

DOE Award No. DE-FC36-03GO13108
NOVEL NON-PRECIOUS METAL CATALYSTS FOR PEMFC:
CATALYST SELECTION THROUGH MOLECULAR MODELING AND
DURABILITY STUDIES

Final Report
(September 2003 – October 2008)

Prepared for

U. S. Department of Energy
Golden Field Office
1617 Cole Blvd
Golden, CO 80401

Prepared by



Principal investigator: Branko N. Popov
Center for Electrochemical Engineering, University of South Carolina
Columbia, SC 29208

Tel: (803) 777-7314; Fax: (803) 777-8265

E-mail: popov@cec.sc.edu; Web Site: <http://www.che.sc.edu>

Team member: Ralph E. White (University of South Carolina)

John W. Van Zee (University of South Carolina)

Collaborators: Alfred B. Anderson (Case Western Reserve University)

Sanjeev Mukerjee (Northeastern University)



UNIVERSITY OF
SOUTH CAROLINA.



CASE
COLLEGE OF ARTS AND SCIENCES



Northeastern
UNIVERSITY

February 2009

DISCLAIMER

This report was prepared as an account of work sponsored by an agency of the United States Government. Neither the United States nor any agency thereof, nor any of their employees, makes any warranty, express or implied, or assumes any legal liability or responsibility for the accuracy, completeness, or usefulness of any information, apparatus, product, or process disclosed, or represents that its use would not infringe privately owned rights. Reference herein to any specific commercial product, process, or service by trade name, trademark, manufacturer, or otherwise does not necessarily constitute or imply its endorsement, recommendation, or favoring by the United States Government or any agency thereof. The views and opinions of authors expressed herein do not necessarily state or reflect those of the United States Government or any agency thereof.

ABSTRACT

The objective of this project is to develop novel non-precious metal electrocatalysts for oxygen reduction reaction (ORR), and demonstrate the potential of the catalysts to perform at least as good as conventional Pt catalysts currently in use in polymer electrolyte membrane fuel cell (PEMFC) with a cost at least 50 % less than a target of 0.2 g (Pt loading)/peak kW and with durability > 2,000 h operation with less than 10 % power degradation. A novel nitrogen-modified carbon-based catalyst was obtained by modifying carbon black with nitrogen-containing organic precursor in the absence of transition metal precursor. The catalyst shows the onset potential of approximately 0.76 V (NHE) for ORR and the amount of H₂O₂ of approximately 3% at 0.5 V (NHE). Furthermore, a carbon composite catalyst was achieved through the high-temperature pyrolysis of the precursors of transition metal (Co and Fe) and nitrogen supported on the nitrogen-modified carbon-based catalyst, followed by chemical post-treatment. This catalyst showed an onset potential for ORR as high as 0.87 V (NHE), and generated less than 1 % of H₂O₂. The PEM fuel cell exhibited a current density of 2.3 A cm⁻² at 0.2 V for a catalyst loading of 6.0 mg cm⁻². No significant performance degradation was observed for 480 h continuous operation. The characterization studies indicated that the metal-nitrogen chelate complexes decompose at the temperatures above 800 °C. During the pyrolysis, the transition metals facilitate the incorporation of pyridinic and graphitic nitrogen groups into the carbon matrix, and the carbon surface modified with nitrogen is active for ORR. In order to elucidate the role of transition metal precursor played in the formation of active sites in the non-precious metal catalysts, a novel ruthenium-based chelate (RuN_x) catalyst was synthesized by using RuCl₃ and propylene diammine as the Ru and N precursors, respectively, followed by high-temperature pyrolysis. This catalyst exhibited comparable catalytic activity and selectivity for ORR as the Pt catalyst.

A theoretical analysis is made of the four-electron reduction reaction of oxygen to water over the mixed anion and cation (202) surface of pentlandite structure Co₉Se₈, one of several selenide phases. Reversible potentials for forming adsorbed reaction intermediates in acid are predicted using adsorption energies calculated with the Vienna *ab initio* simulation program (VASP) and the known bulk solution values together in a linear Gibbs energy relationship.

The effect of hydrophobic and structural properties of a single/dual-layer cathode gas diffusion layer on mass transport in PEM fuel cells was studied using an analytical expression. The simulations indicated that liquid water transport at the cathode is controlled by the fraction of hydrophilic surface and the average pore diameter in the cathode gas diffusion layer. The

optimized hydrophobicity and pore geometry in a dual-layer cathode GDL leads to an effective water management, and enhances the oxygen diffusion kinetics.

TABLE OF CONTENTS

DISCLAIMER	ii
ABSTRACT	iii
TABLE OF CONTENTS	v
LIST OF TABLES	viii
LIST OF FIGURES	x
EXECUTIVE SUMMARY	xv
1. INTRODUCTION	1
2. EXPERIMENTAL	3
2.1. Catalyst synthesis	3
2.1.1. Synthesis of nitrogen-modified carbon-based catalysts in the absence of transition metal precursor (metal-free catalysts)	3
2.1.2. Synthesis of carbon composite catalysts in the presence of iron and cobalt precursors	4
2.1.3. Synthesis of carbon composite catalysts in the presence of ruthenium precursor (RuN _x /C)	4
2.2. Rotating ring disk electrode (RRDE) measurements	4
2.3. Fuel cell testing	5
2.4. Physical and chemical characterizations	6
3. RESULTS AND DISCUSSION	7
3.1. Nitrogen-modified carbon-based catalysts synthesized in the absence of transition metal precursor (metal-free catalysts)	7
3.1.1. Electrochemical, physical and chemical studies	7
3.1.2. Discussion of active sites	13
3.1.3. Summary	16
3.2. Carbon composite catalysts synthesized in the presence of iron and cobalt precursors	17
3.2.1. Electrocatalytic properties of metal-free catalysts	17
3.2.2. Electrocatalytic properties of carbon composite catalysts	19

3.2.3. Characterizations of metal-nitrogen complexes and metallic species in carbon composite catalysts-----	22
3.2.4. Characterizations of nitrogen functional groups on carbon composite catalysts -----	26
3.2.5. Durability study of PEM fuel cell with carbon composite cathode catalyst -----	29
3.2.6. Summary-----	31
3.3. Carbon composite catalysts synthesized in the presence of ruthenium precursor (RuN _x /C catalysts) -----	33
3.3.1. Formation of active reaction sites on RuN _x /C catalysts -----	33
3.3.2. Effect of nitrogen contents on catalytic activity and selectivity of RuN _x /C catalysts -----	36
3.3.3. Surface-modification of RuN _x /C catalysts -----	38
3.3.4. Comparative study of RuN _x -based catalysts synthesized with different methodologies -----	39
3.3.5. Summary-----	40
4. CONCLUSIONS-----	41
5. REFERENCES -----	46
6. PRODUCTS DEVELOPED UNDER THE AWARD-----	46
a1. Special recognition & awards-----	46
a2. Publications-----	47
a3. Presentations -----	50
b. Web site that reflect the results of this project -----	52
c. Collaborations fostered -----	53
d. Inventions/Patent applications -----	54
7. MATHEMATICAL MODELING-----	55
Abstract-----	55
7.1. Experimental and theoretical study of cobalt selenide as a catalyst for O ₂ electroreduction-----	56
7.1.1. Introduction-----	56
7.1.2. Experimental studies-----	57

7.1.3. Theoretical approach-----	59
7.1.4. Theoretical results-----	62
7.1.5. Conclusions-----	65
7.1.6. References-----	68
7.2. Effect of hydrophobicity and pore geometry in cathode GDL on PEM fuel cell performance-----	71
7.1.1. Introduction-----	71
7.1.2. Mathematical model development-----	71
7.1.3. Results and discussion-----	75
7.1.4. Conclusions-----	83
7.1.5. References-----	83

LIST OF TABLES

Table 3-1-1.	The amount of H ₂ O ₂ produced at 0.5 V (NHE) during oxygen reduction on carbon-based catalysts modified with different nitrogen donors and heat-treated at 800 °C. -----	9
Table 3-1-2.	BET surface areas of different samples. -----	10
Table 3-1-3.	Bulk transition metal concentrations in UF-C and SeUF-C determined by ICP-MS. -----	12
Table 3-1-4.	Surface compositions of different samples determined by XPS. -----	14
Table 3-2-1.	H ₂ O ₂ percentages at 0.5 V (NHE) and number of electrons (n) transferred during oxygen reduction on the metal-free catalysts. -----	19
Table 3-2-2.	H ₂ O ₂ percentages determined at different disk potentials for the metal-free catalyst, the as-pyrolized carbon composite catalyst, the as-leached carbon composite catalyst, and the conventional Pt/C catalyst (20 wt% Pt, E-TEK). -----	20
Table 3-2-3.	Concentrations of Co and Fe in the carbon composite catalyst obtained before and after the chemical leaching in 0.5 M H ₂ SO ₄ solution at 90 °C, determined by ICP-MS and XPS. -----	25
Table 3-2-4.	Catalytic activity, selectivity, surface nitrogen concentration, and XPS spectrum at each synthesis step of the carbon composite catalyst. The current density and the amount of H ₂ O ₂ were determined at 0.4 V in a fuel cell (6.0 mg cm ⁻² cathode catalyst loading, 30 psi back pressure) and an RRDE, respectively. -----	27
Table 3-3-1.	Surface compositions of the as-refluxed and as-pyrolized RuN _x /C catalysts determined by XPS. -----	34
Table 3-3-2.	Kinetically limited currents, I _k , at 0.7 V (NHE) determined for the RuN _x /C catalysts prepared using different molar ratios of Ru to N in the precursor solution. -----	37
Table 7-2-1.	Values for various simulation parameters and physical properties. -----	76
Table 7-2-2.	Values for the simulation parameters for the fitting. -----	77

Table 7-2-3. Values for physical properties of the MPS with and without the MPL. --81

LIST OF FIGURES

- Figure 3-1-1. Cyclic voltammograms of the un-oxidized and oxidized carbons. The measurements were performed in N₂ saturated 0.5 M H₂SO₄ solution using a potential scan rate of 5 mV s⁻¹. -----7
- Figure 3-1-2. Polarization curves of oxygen reduction on the un-oxidized and oxidized carbons. The measurements were performed in O₂ saturated 0.5 M H₂SO₄ solution using a potential scan rate of 5 mV s⁻¹ and a rotation speed of 900 rpm. -----8
- Figure 3-1-3. Polarization curves of oxygen reduction and (b) percentages of H₂O₂ formed during oxygen reduction on carbon-based catalysts modified with different nitrogen donors and heat-treated at 800 °C. For comparison, the curve measured on the oxidized carbon was also shown. The measurements were performed in O₂ saturated 0.5 M H₂SO₄ solution using a potential scan rate of 5 mV s⁻¹ and a rotation speed of 900 rpm. -----8
- Figure 3-1-4. Polarization curves of oxygen reduction on SeUF-C heat-treated at different temperatures between 400 and 1000 °C. The measurements were performed in O₂ saturated 0.5 M H₂SO₄ solution using a potential scan rate of 5 mV s⁻¹ and a rotation speed of 900 rpm. -----10
- Figure 3-1-5. XRD patterns of UF-C and SeUF-C (a) before and (b) after heat-treatment at 800 °C. -----11
- Figure 3-1-6. TEM image of SeUF-C heat-treated at 800 °C. -----11
- Figure 3-1-7. Polarization curve of the H₂-O₂ PEM fuel cells prepared with UF-C and 20 wt% Pt/C catalysts, respectively. UF-C loading: 6 mg cm⁻²; Pt/C loading: 0.1 mg cm⁻²; H₂/O₂ back pressures: 30 psi/40 psi; operation temperature: 75 °C. (b) SEM image of the cross-section of the MEA prepared with UF-C catalyst. (c) Current transient (stability test) at 0.4 V of the H₂-O₂ PEM fuel cell prepared with UF-C catalyst. Catalyst loading: 4 mg cm⁻²; H₂/O₂ back pressures: 30 psi/30 psi; operation temperature: 75 °C. -----13
- Figure 3-1-8. XPS spectra of N 1s region obtained for SeUF-C heat-treated at 600–1000 °C. -----15

- Figure 3-2-1. Polarization curves on the rotating disk electrodes for the carbon (Ketjen) blacks treated by various methods: (a) as-received carbon, (b) HNO₃-treated carbon, (c) NH₃-treated carbon, (d) urea-formaldehyde-modified carbon, and (e) selenourea-formaldehyde-modified carbon. The measurements were performed in 0.5 M H₂SO₄ solution saturated with O₂ using a potential scan rate of 5 mV s⁻¹ and a rotation speed of 900 rpm. -----17
- Figure 3-2-2. Polarization curves on the rotating disk electrodes for the as-received carbon, the metal-free catalyst and the carbon composite catalyst (as-leached). The measurements were performed in 0.5 M H₂SO₄ solution saturated with O₂ using a potential scan rate of 5 mV s⁻¹ and a rotation speed of 900 rpm. -----19
- Figure 3-2-3. Polarization curves of PEM fuel cells prepared with the different cathode catalysts: the metal-free catalyst, the as-pyrolized carbon composite catalyst, and the as-leached carbon composite catalyst. The cathode catalyst loadings were maintained at 6.0 mg cm⁻². The experiments were performed using 30 psi back pressure on both anode (H₂) and cathode (O₂) compartments. -----21
- Figure 3-2-4. (a) Polarization curves of PEM fuel cells prepared with the carbon composite catalysts. The catalysts were prepared using the metal-nitrogen complexes with different compositions. All the catalysts were subjected to the chemical leaching. The cathode catalyst loading was 6.0 mg cm⁻². (b) PEM fuel cell performances for different loadings of the optimized carbon composite catalyst. The experiments were performed using 30 psi back pressure on both anode (H₂) and cathode (O₂) compartments. -----22
- Figure 3-2-5. k₁-weighted EXAFS data for the carbon composite catalysts pyrolized at various temperatures. The catalyst was prepared by the CoN_x deposition onto the metal-free carbon support, followed by the pyrolysis. No chemical leaching was conducted on the pyrolized catalysts. -----23
- Figure 3-2-6. TEM images of (a) the metal-free carbon support and (b) the carbon composite catalyst. The carbon composite catalyst was subjected to the chemical leaching. -----24
- Figure 3-2-7. Powder XRD patterns of the metal-free carbon support and the carbon composite catalyst. The carbon composite catalyst was subjected to the chemical leaching. -----24

Figure 3-2-8.	XPS spectra of N 1s region obtained for the catalysts pyrolyzed in the absence and presence of transition metals (Co and Fe). The carbon composite catalysts were subjected to the chemical leaching. -----	28
Figure 3-2-9.	Typical stability test data for the carbon composite catalyst. -----	29
Figure 3-2-10.	Galvanostatic potential transient measured on the carbon composite catalyst for stability test. The cathode catalyst loading was 2.0 mg cm ⁻² . The tests were run at 200 mA cm ⁻² using H ₂ and O ₂ without applying the back pressure. -----	30
Figure 3-2-11.	XPS spectra of N 1s region for the catalysts taken from the fresh MEA and the MEA tested for 480 h. -----	31
Figure 3-2-12.	SEM image of the cross-section of the MEA prepared using the carbon composite cathode catalyst. -----	31
Figure 3-3-1.	Polarization curves on the rotating disk electrodes for the RuN _x /C catalysts pyrolyzed at 600 to 900 °C. The measurements were performed in 0.5 M H ₂ SO ₄ solution saturated with oxygen at the potential scan rate of 5 mV s ⁻¹ and the rotation speed of 900 rpm. -----	33
Figure 3-3-2.	XPS spectra of N 1s region for the RuN _x /C catalysts: (a) as-refluxed and (b) as-pyrolyzed. -----	35
Figure 3-3-3.	XRD patterns of the RuN _x /C catalysts subjected to pyrolysis at 600 to 800 °C. For comparison, the XRD pattern for the as-refluxed catalyst is given in the figure. -----	35
Figure 3-3-4.	Polarization curves on the rotating disk electrodes for the RuN _x /C catalysts prepared using different molar ratios of Ru to N in the precursor solution. -----	36
Figure 3-3-5.	Koutecky-Levich plots at different potentials measured on the RuN _x /C catalysts prepared with the Ru:N ratio of 1:20. -----	37
Figure 3-3-6.	(a) Ring currents and (b) H ₂ O ₂ percentages determined as a function of the disk potential for the RuN _x /C catalysts with different molar Ru:N ratios. -----	38
Figure 3-3-7.	(a) Polarization curves on the rotating disk electrodes and (b) H ₂ O ₂ percentages measured for the RuN _x /C catalysts prepared using urea as additive. -----	39

Figure 3-3-8.	(a) Polarization curves on the rotating disk electrodes and (b) H ₂ O ₂ percentages measured for various Ru-based catalysts: urea-modified RuN _x /C, RuO _x /C, amorphous Mo _x Ru _y Se _z /C and Ru-NH ₃ /C. The RRDE data obtained from the commercial Pt/C is also presented in the figure. -- -----40
Figure 7-1-1.	Effect of heat-treatment on oxygen reduction for unsupported cobalt selenide. Pt/C results are included for comparison. The RDE measurements were performed in 0.5 M H ₂ SO ₄ solution saturated with oxygen by using a potential scan rate of 5 mV s ⁻¹ and rotation speed of 900 rpm. -----58
Figure 7-1-2.	Co ₉ Se ₈ unit cell in pentlandite structure (4Co ₉ Se ₈ , 68 atoms; Cobalt atoms are blue). The (202) surface is shown as the highlighted crystal plane. Optimized cell lattice constant a = 10.374 Å (experimental a = 10.431 Å). -----60
Figure 7-1-3.	Slab (202) surface model used in the adsorption calculations showing the top two layers relaxed. -----61
Figure 7-1-4.	Predicted H ₂ O oxidation reactions over a four-atom Co site forming the 2-fold hydroxylated (202) surface. -----63
Figure 7-1-5.	O ₂ dissociation on the (202) Co ₉ Se ₈ hydroxylated surface model. ----64
Figure 7-1-6.	First electron transfer step during O ₂ reduction on (202) Co ₉ Se ₈ : structure S4 has the highest. -----66
Figure 7-1-7.	Two predicted pathways for the second, third, and fourth electron transfer steps for O ₂ reduction on (202) Co ₉ Se ₈ . Path 1 has the favored higher potential. For the fourth electron transfer step 0.37 V is the reversible potential for producing the surface state chosen as the standard one for the beginning of the calculations. -----67
Figure 7-2-1.	Bulk porosity with respect to average pore diameter for MPS with different PTFE contents. -----75
Figure 7-2-2.	Comparison of model and experimental polarization curves. Parameters are given in Table 7-2-2 and the data are from [3]. -----77
Figure 7-2-3.	(a) Saturation profile across the MPS with average pore diameter. (b) Polarization curves with average pore diameter in the MPS. -----78

Figure 7-2-4. (a) Saturation profile across the MPS with fraction of hydrophilic surface. (b) Polarization curves with fraction of hydrophilic surface in the MPS. ---
-----79

Figure 7-2-5. (a) Gradients of fraction of hydrophilic surface with respect to average pore diameter in a diffusion layer. (b) Average saturation in the MPS with gradient of fraction of hydrophilic surface with respect to average pore diameter. -----80

Figure 7-2-6. (a) Saturation profile across the MPS at various pairs of the average pore diameter and fraction of hydrophilic surface. (b) Polarization curves using the MPS at various pairs of the average pore diameter and fraction of hydrophilic surface. -----81

Figure 7-2-7. (a) Saturation profile across the GDL with average pore diameter in the MPL. (b) Polarization curves with average pore diameter in the MPL. -82

Figure 7-2-8. (a) Saturation profile across the GDL at various pairs of the average pore diameter and fraction of hydrophilic pore in the MPL. (b) Polarization curves using the MPL at various pairs of the average pore diameter and fraction of hydrophilic pore. -----83

EXECUTIVE SUMMARY

The goal of this project is to demonstrate the potential of the carbon-based composite electrocatalysts to perform as well as conventional Pt catalysts currently in use in MEAs with a cost at least 50 % less than a target of 0.2 g (Pt loading)/peak kW. The optimization of the catalyst composition is based on durability > 2000 h of continuous operation with less than 10 % power degradation.

The specific objectives are (i) to develop highly active and stable carbon-based electrocatalysts with strong Lewis basicity (π electron delocalization) for ORR, (ii) To optimize the active reaction sites for ORR, (iii) to perform electrochemical polarization and stability tests under various conditions and to demonstrate the potential of carbon-based catalysts to substitute conventional Pt catalysts currently used in MEA.

Metal free, carbon-based catalysts were synthesized by modifying the surface functional groups on the porous carbon black with low-cost organic precursors. Metal free catalysts for oxygen reduction reaction are obtained by the modification of carbon using nitric acid to introduce oxygen surface groups particularly quinone and hydroquinone groups. Following this nitrogen surface groups were anchored onto the modified/oxidized carbon using various nitrogen containing precursors like melamine thiourea/urea/selenourea by a simple addition-condensation polymerization reaction. Subsequently, the synthesized powders were subjected to a high temperature treatment between 800 – 1000 °C in a flow reactor in Ar atmosphere. The active reaction sites for ORR were optimized as a function of: (i) carbon support, (ii) surface oxygen groups, (iii) nitrogen content, (iv) pyrolysis temperature, (v) porosity, (vi) pore size distribution and (vii) the concentration of the non-metallic additive. In this work, we have demonstrated that carbon upon chemical modification with nitric acid and treatment with nitrogen rich precursors like urea, selenourea and melamine is active for ORR and exhibits excellent selectivity towards the four electron reduction of oxygen to water.

Carbon based catalyst was synthesized with activation overvoltage of 0.9 V which is similar to Pt activation overvoltage. For comparison, the activation overvoltage of carbon blacks is only 0.1V. The amount of peroxide produced during oxygen reduction was zero compared with platinum which produces up to 2% of peroxide.

The accomplishments are as follows:

- (i) Carbon based catalyst was synthesized with activation overvoltage of 0.9 V vs NHE. For comparison, the activation overvoltage of carbon blacks is 0.1V.

- (ii) It is generally known that a carbonaceous material catalyzes oxygen reduction to H_2O_2 via two electron pathway; however, the optimized metal-free catalyst in our laboratories catalyzes oxygen reduction to water via four-electron pathway with producing no H_2O_2 at 0.5 V vs. HER. Pt catalyst generates 1 to 2 % H_2O_2 . To our knowledge, such a high selectivity of carbonaceous material has not been reported in the literature.
- (iii) Using XPS the catalytic sites of the metal free catalyst were identified as pyridinic and graphitic nitrogen groups which contribute to high activity and stability of this novel catalyst. Identifying the catalytic sites creates new opportunities to further optimize the performance of the catalyst.
- (iv) After polymerization and heat treatment a further reduction in the active surface area can be observed. The catalyst exhibits more mesoporous area and hence more active surface area is accessible for oxygen transport.
- (v) Stability testing of 4 mg/cm^2 of metal free catalyst was performed in the fuel cell at 75°C at 0.4 V. The results showed a current density of 0.12 Acm^2 and steady state current profile without showing performance degradation for up to 300 hours. The absence of any metal impurity has been confirmed by XRD

A highly active carbon composite catalyst was developed using a metal-free catalyst as a support through the following steps: (i) catalyzed pyrolysis in presence of transition metals and (ii) chemical post-treatments. The catalyzed pyrolysis was carried out using a procedure developed in our laboratories. Catalytic activity of the composite catalyst is as high as 1.0 A cm^{-2} at 0.4 V and 2.0 A cm^{-2} at 0.2 V for 4 mg cm^{-2} catalyst loading (no IR compensated). The optimized pyrolysis parameters increase the onset potential of the carbon composite catalyst for ORR to 0.9 V vs. NHE. The amount of H_2O_2 produced decreased to a level lower than 1 %. No irreversible loss was observed of catalytic activity during 300 hours of continuous operation.

Patent Application Number: 11939322; Confirmation Number 9723 has been filed for all three catalysts developed in our Laboratories, namely: (i) the metal free, (ii) carbon composite and (iii) Pt-Co catalyst for oxygen reduction in PEMFC.

The accomplishments are as follows:

- (i) Catalytic activity as high as (i) 1.0 A cm^{-2} at 0.4 V and 2.0 A cm^{-2} at 0.2 V for 4 mg cm^{-2} catalyst loading (no IR compensated).
- (ii) The optimized pyrolysis parameters increase the onset potential of the carbon composite catalyst for ORR to 0.9 V vs. NHE.

- (iii) The amount of H₂O₂ produced decreased to a level lower than 1 %.
- (iv) No irreversible loss of catalytic activity during 300 hours of continuous operation.
- (v) XPS results indicate that high temperature pyrolysis combined with chemical post-treatment increases the concentration of pyridine-the nitrogen resulting in the increased Lewis basicity, and incorporates the nitrogen into graphitic structures that increases the stability.

A novel process was developed to synthesize ruthenium-based chelate (RuN_x) electrocatalysts for the oxygen reduction reaction, using RuCl₃ and propylene diamine as the Ru-and N-precursors, respectively. High-temperature pyrolysis has a critical role in the formation of the catalytic Ru-N sites for oxygen reduction.

The following goals were accomplished:

- (i) Novel catalyst based on RuN was synthesized using low cost ruthenium compounds.
- (ii) The onset potential of RuN catalyst for ORR to 0.9 V vs. NHE.
- (iii) The RuN_x catalyst modified in the presence of nitrogen-containing organic exhibited comparable catalytic activity and selectivity for oxygen reduction to the carbon-supported Pt catalyst in acidic media.
- (iv) From the TEM analysis, the particle size of the RuN₄ catalysts was estimated to be 2-4 nm which explains the observed high catalytic activity.
- (v) The catalyst generates less than 2 % hydrogen peroxide during oxygen reduction indicating high catalytic activity toward four electron reduction.
- (vi) From the results of rotating ring disc electrode (RRDE) experiments and XPS measurements, it is was that the high-temperature pyrolysis leads to the formation of Ru clusters coordinated with pyridinic N, and such Ru-N chelate sites are catalytically active for oxygen reduction.

Ruthenium-based bimetallic electrocatalysts with non-noble metals such as Ti, Cr, Fe, Co and Pb were synthesized on a porous carbon support using a chelation process.

The accomplishments are summarized as follows:

- (i) The catalytic activity for ORR increased in the order of RuCrN_x/C, RuTiN_x/C, RuPbN_x/C, RuCoN_x/C and RuFeN_x/C, indicating that the non-noble metal in the bimetallic catalyst has a crucial role in the catalytic activity.

- (ii) The RuFeN_x/C catalyst showed the onset potential for ORR as high as 0.9 V(NHE) which is comparable to that of the Pt/C catalyst.
- (iii) The TEM analysis indicated that the RuFeN_x/C catalyst consists of uniformly dispersed particles as large as 5 – 6 nm.
- (iv) The MEA prepared with the RuFeN_x/C cathode catalyst exhibited the maximum power density of ca. 0.18 W cm⁻² and no performance degradation for 150 h of continuous operation.

Two theoretical models were developed entitled “Experimental and theoretical study of cobalt selenide as a catalyst for oxygen electro-reduction” and “Effect of PTFE content in microporous layer on water management in PEM fuel cells”.

Cobalt sulfides have been known for more than 30 years to be active toward oxygen reduction and cobalt selenides have shown less activity. In this paper a theoretical analysis is made of the four-electron reduction reaction of oxygen to water over the mixed anion and cation (202) surface of pentlandite structure Co₉Se₈, one of several selenide phases. Reversible potentials for forming adsorbed reaction intermediates in acid are predicted using adsorption energies calculated with the Vienna *ab initio* simulation program (VASP) and the known bulk solution values together in a linear Gibbs energy relationship. Comparison with an earlier theoretical analysis of pentlandite structure Co₉S₈ shows the overpotential is predicted to be larger for the selenide by around 0.46 V. Cobalt selenide electrodes of unspecified stoichiometry were prepared chemically on glassy carbon discs and polarization curves were measured using rotating discs. When heat treated at 900 °C the onset potential for O₂ reduction was found to be 0.5 V (NHE) whereas electrodes not subject to heat treatment was inactive. For Co₃S₄, onset potentials in the literature are ~0.8 V (NHE), consistent with a ~0.3 V higher measured overpotential for the selenide. The theoretical predictions for the pentlandite sulfide and selenide surfaces are in qualitative agreement.

The effect of hydrophobic and structural properties of a single/dual-layer cathode gas diffusion layer on mass transport in PEM fuel cells was studied using an analytical expression. The simulations indicated that liquid water transport at the cathode is controlled by the fraction of hydrophilic surface and the average pore diameter in the cathode gas diffusion layer. The optimized hydrophobicity and pore geometry in a dual-layer cathode GDL leads to an effective water management, and enhances the oxygen diffusion kinetics.

1. INTRODUCTION

Platinum is considered the best electrocatalyst for the four-electron reduction of oxygen to water in acidic environments as it has the lowest overpotential and the highest stability [1-5]. However, even on pure Pt, potentials in excess of 300 mV are lost from the thermodynamic potential for oxygen reduction reaction (ORR) due to the competing water activation and sluggish kinetics. Furthermore, oxygen undergoes a non-dissociative adsorption on Pt metals accompanied by some dissociative adsorption, which results in Pt oxidation. Most importantly, Pt remains an expensive metal with low abundance.

Since Jasinski's discovery of the catalytic properties of cobalt phthalocyanines [6], there has been a considerable research on non-precious metal catalysts such as: (i) porphyrin-based macrocyclic compounds of transition metals (e.g., cobalt phthalocyanines and iron tetramethoxyphenyl porphyrin (Fe-TMPP)) [7-23], (ii) vacuum-deposited cobalt and iron compounds (e.g., Co-C-N and Fe-C-N) [24, 25], and (iii) metal carbides, nitrides and oxides (e.g., FeC_x , TaO_xN_y , MnO_x/C) [26, 27]. Pyrolysis at higher temperatures than 800 °C in an inert or NH_3 atmosphere led to the improvement in catalytic activity of the catalysts to some extent, but none of the above catalysts are active enough to be used as oxygen reduction catalysts for PEM fuel cells. Due to low selectivity (H_2O_2 amount > 5%) and poor stability, the transition metal-based catalysts reported in the literature so far do not qualify as catalyst for ORR.

There is disagreement in the literature regarding the catalytic reaction site for oxygen reduction and the relevant mechanism on non-precious metal catalysts. The most commonly accepted hypothesis is that the metal- N_4 center bound to the carbon support is catalytically active, and the central metal ion in the macrocycle plays a crucial role in the ORR [7-23, 28]. Beck et al. [28] have proposed that oxygen reduction on N_4 -chelates of transition metal occurs via a modified "redox catalysis" mechanism. That is, an oxygen molecule is adsorbed on the catalyst metal center to form an oxygen-catalyst adduct, followed by electron transfer from the metal center and the regeneration of the reduced N_4 -chelates. From the analysis of Fe-based catalysts by Time-of-Flight Secondary Ion Mass Spectrometry, Dodelet and his coworkers [14] have found that two different catalytic sites, i.e., FeN_4/C and FeN_2/C , coexist in the catalysts, irrespective of the Fe precursors used. Here, FeN_4/C represents a Fe ion coordinated to four nitrogen atoms of the pyrrolic type, and FeN_2/C stands for a Fe ion coordinated to two nitrogen atoms of the pyridinic type.

On the other hand, Yeager [29] found that after the heat-treatment of Co-TMPP and Fe-TMPP at 800 °C, neither Co nor Fe was detected in the Mössbauer spectra in a form corresponding to coordination with nitrogen. Yeager and Wiesener [30] have suggested that the transition metals do not act as an active reaction site for oxygen reduction, but rather serve primarily to facilitate the stable incorporation of nitrogen into the graphitic carbon during high-temperature pyrolysis of metal-nitrogen complexes. This means that high-temperature pyrolysis in the presence of transition metals yields a carbonaceous layer with a large amount of nitrogen groups that are catalytically active for oxygen reduction.

Nitrogen-containing carbons have been typically prepared using implantation through NH_3 or HCN treatment of carbon at high temperatures. The experimental measurements of nitrated Ketjen black indicated an onset potential for oxygen reduction of approximately 0.5 V (NHE) compared to that of 0.2 V (NHE) for un-treated carbon [31, 32]. Another way to prepare carbons with controlled nitrogen content is to synthesize carbon powder using nitrogen-containing polymer precursors, followed by a physical or chemical activation process [33-38]. Matter et al. [39-41] prepared an active non-metal catalyst for oxygen reduction through decomposition of acetonitrile vapor over an alumina support containing 2 wt% Fe or Ni. The results obtained by using a rotating ring disk electrode (RRDE) technique indicated only 100 mV greater overpotential than Pt catalyst, but the measured current were in the micro Ampere range. The catalyst activity was attributed to pyridinic nitrogen incorporated into edge planes as determined by X-ray photoelectron spectroscopy (XPS). However, a measurable cathode current was observed in the RRDE experiments only at the potential range for H_2O_2 formation (i.e., below approximately 0.6 V (NHE)).

The objective of this project is to develop the novel non-precious metal catalysts with comparable selectivity, activity, and stability to Pt for ORR in polymer electrolyte membrane (PEM) fuel cell in order to decrease the cost of fuel cell catalysts.

The objective of this project is to develop novel non-precious metal electrocatalysts for oxygen reduction reaction (ORR), and demonstrate the potential of the catalysts to perform at least as good as conventional Pt catalysts currently in use in polymer electrolyte membrane fuel cell (PEMFC) with a cost at least 50 % less than a target of 0.2 g (Pt loading)/peak kW and with durability > 2,000 h operation with less than 10 % power degradation. In addition, we intend to elucidate the active sites of non-precious metal catalysts by using a variety of physical and chemical characterization techniques and molecular modeling. Furthermore, the effect of hydrophobic and structural properties of a single/dual-layer cathode gas diffusion layer on mass transport in PEM fuel cells was studied.

2. EXPERIMENTAL

2.1. CATALYST SYNTHESIS

2.1.1. Synthesis of Nitrogen-Modified Carbon-Based Catalysts in the Absence of Transition Metal Precursor (Metal-Free Catalysts)

Nitrogen-modified carbon-based catalysts (metal-free catalysts) were prepared with a four-step process that includes (i) removal of metal impurities, (ii) chemical oxidation of carbon support, (iii) synthesis of nitrogen-rich polymeric resins on the oxidized carbon, and (iv) pyrolysis of the resulting powder at elevated temperatures in an inert atmosphere.

Initially, commercially available Ketjen Black EC 300J was pre-washed with 6 M HCl to remove any of metal impurities on the carbon. The carbon was washed several times with deionized water to remove any of chloride and metal impurities. The pre-washed carbon was subject to oxidation in 70% HNO₃ for 7 h under refluxing conditions and then washed in distilled water followed by drying in an oven at 75 °C.

Various nitrogen-based resins such as melamine formaldehyde (MF), urea formaldehyde (UF), thiourea formaldehyde (TUF), and selenourea formaldehyde (SeUF) were synthesized by a simple addition-condensation reaction on the oxidized carbon [42]. In the first step, by the addition of formaldehyde, melamine or urea is hydroxymethylolated to the amino groups. In the case of UF, this reaction leads to the formation of mono-, di- and tri-methylureas. The second step consists of condensation of the methylolureas to low molecular weight polymers. The condensation reaction occurs only at acidic environment and results in the formation of methylene bridges between amido nitrogens and methylene ether linkages by the reaction of two methylol groups.

For every 10 g of the oxidized carbon black, melamine, urea, thiourea or selenourea was mixed with formaldehyde in 100 ml of distilled water. The molar ratio of melamine to formaldehyde in the precursor solution was maintained at 1:3, and the urea (or thiourea, selenourea) to formaldehyde was 1:2. After the solution temperature reaches 50 °C, NaOH solution was added to bring the pH of the solution to around 10.0. This initiates the addition reaction. Then, the polymerization reaction was initiated by increasing the temperature of the solution to 75 °C and by acidifying the solution with H₂SO₄ solution to pH = 2.5. The solution was stirred for 4 h. The resulting gel was dried overnight in a vacuum oven at 90 °C. The

resulting powder was placed in a quartz boat and inserted into a 10 cm diameter quartz tube. The pyrolysis was carried out at high temperatures in the range of 400 to 1000 °C for 90 min. N₂ gas was purged into the reactor continuously throughout the pyrolysis step.

2.1.2. Synthesis of Carbon Composite Catalysts in the Presence of Iron and Cobalt Precursors

The carbon composite catalyst was synthesized using the nitrogen-modified carbon-based catalysts (metal-free catalysts) described in 2.1.1. Section as a support through the three consecutive steps: (i) the deposition of Co-N or Co-Fe-N chelate complex on the support, and (ii) the high-temperature pyrolysis, and (iii) the chemical post-treatment (acid leaching). Co(NO₃)₂, FeSO₄, and ethylene diamine (H₂NCH₂CH₂NH₂) were used as Co-, Fe- and N-precursors, respectively. Desired amounts of Co(NO₃)₂ and/or FeSO₄ were dissolved in ethanol. A mixture of ethylene diamine and ethanol was added drop-wise into the reaction mixture, followed by vigorous stirring for 1 h. In the reaction mixture, the atomic ratio of metal : nitrogen varied between 1 : 4 and 1 : 24. The metal-free carbon support was added into the reaction mixture and refluxed at 85 °C for 4 h. The solvents were removed in a rotary evaporator at 80 °C under vacuum, and the resulting power specimen was heat-treated (pyrolyzed) in an argon atmosphere at different temperatures of 600 – 900 °C for 1 h. In order to remove excess metal elements deposited on the support, the pyrolyzed sample was treated with 0.5 M H₂SO₄ solution at 90 °C for 4 h, and washed thoroughly with deionized water.

2.1.3. Synthesis of Carbon Composite Catalysts in the Presence of Ruthenium Precursor (RuN_x/C)

The desired amount of RuCl₃ was dissolved in isopropyl alcohol (100 mL). The solution was refluxed at 80 – 90 °C under stirring conditions. Next, propylene diamine was added into the solution to form Ru-N complexes, followed by the addition of carbon black powders (0.4 g, Ketjen Black). The mixture was refluxed for several hours and then dried under vacuum at 80 °C. The resulting powder specimens were heat-treated in an argon atmosphere at various temperatures ranging from 600 to 900 °C.

2.2. RRDE MEASUREMENTS

Electrochemical characterization of the synthesized catalysts was performed in a RRDE setup that employs a standard three-compartment electrochemical cell. The RRDE has a

platinum ring (5.52 mm inner diameter and 7.16 mm outer diameter) and a glassy carbon disk (5.0 mm diameter) as the working electrode; a saturated mercury-mercury sulfate electrode is the reference electrode and a platinum foil acts as the counter electrode. All potentials in this work were referred to a normal hydrogen electrode (NHE).

The catalyst ink was prepared by ultrasonically blending 8 mg of catalyst with 1 mL of isopropyl alcohol. 15 μL of the ink was then deposited onto the glassy carbon surface. 5 μL of 0.25 wt % Nafion solution (a mixture of 5 wt % Nafion solution and isopropyl alcohol with the volume ratio of 1:19) was applied onto catalyst layer to ensure better adhesion of catalyst onto glassy carbon. 0.5 M H_2SO_4 was the electrolyte. The system was purged with N_2 to clean the surface of catalyst by scanning the potential between 1.04 and 0.04 V (NHE) at a sweep rate of 50 mV s^{-1} . The electrode was scanned in N_2 saturated electrolyte at a sweep rate of 5 mV s^{-1} to evaluate the background capacitance current. The electrocatalytic activity of catalyst was then measured by saturating the electrolyte with O_2 . Linear sweep voltammograms were measured at 900 rpm. The ring potential was maintained at 1.2 V (NHE) throughout the experiment in order to oxidize H_2O_2 produced during oxygen reduction on disk electrode. The percentage of H_2O_2 was calculated using the following equation:

$$\% \text{H}_2\text{O}_2 = \frac{200(I_r/N)}{I_d + (I_r/N)}$$

where I_d , I_r and N are the disk current, ring current and collection efficiency, respectively. The value of N was taken as 0.39 for our experiments.

2.3. FUEL CELL TESTING

To construct the membrane-electrode assemblies (MEAs), the cathode catalyst ink was prepared by ultrasonically blending catalyst with Nafion solution and isopropyl alcohol for 4 h. The catalyst ink was then sprayed onto a gas diffusion layer (GDL) (ELAT LT 1400W, E-TEK) until a desired catalyst loading has been achieved. A commercially catalyzed GDL (0.5 mg cm^{-2} Pt, E-TEK) was used as the anode. A thin layer of Nafion was coated on both the cathode and anode surfaces. The Nafion-coated anode and cathode were hot-pressed to a Nafion 112 membrane at 140 $^\circ\text{C}$ and 534 kPa for 3 min. The geometric area of the electrode was 5 cm^2 .

The MEA testing was carried out in a single cell with serpentine flow channels. Pure H_2 gas humidified at 77 $^\circ\text{C}$ and pure O_2 gas humidified at 75 $^\circ\text{C}$ were supplied to the anode and cathode

compartments, respectively. The measurements were conducted using a fully automated test station (Fuel Cell Technologies Inc.) at 75 °C. In order to evaluate the durability of the catalyst, potentiostatic current transient technique was used by applying a constant potential or current density.

2.4. PHYSICAL AND CHEMICAL CHARACTERIZATIONS

Extended X-ray absorption fine structure (EXAFS) spectra were recorded at room temperature at beam line X9B of the National Synchrotron Light Source at Brookhaven National Laboratory. The data were collected in the transmission mode. The background removal and edge-step normalization were performed using the FEFFIT 3.42 program, and the experimental EXAFS data were analyzed by the FEFF 7.0 program.

Surface analysis of the catalyst was performed using X-ray photoelectron spectroscopy (XPS) with a KRATOS AXIS 165 high performance electron spectrometer. Inductively coupled plasma-mass spectroscopy (ICP-MS) was conducted with an SCIEX ELAN DRc ICP-MS system (Perkin-Elmer) to analyze the bulk transition metals in the catalysts. X-ray diffraction (XRD) pattern was recorded on an automated Rigaku diffractometer equipped with a Cu K α radiation and a graphite monochromatic operation at 45 kV and 40 mA. Transmission electron microscopy (TEM, Hitachi H-8000) was used to determine the distribution of carbon and to confirm the absence of metal particles in the catalyst. The BET surface area of the catalyst was evaluated in a Quantachrome NOVA BET 2000 analyzer using N₂ gas sorption.

3. RESULTS AND DISCUSSION

3.1. NITROGEN-MODIFIED CARBON-BASED CATALYSTS SYNTHESIZED IN THE ABSENCE OF TRANSITION METAL PRECURSOR (METAL-FREE CATALYSTS)

3.1.1. Electrochemical, Physical and Chemical Studies

Figure 3-1-1 shows the cyclic voltammograms of the un-oxidized and oxidized carbons. The measurements were performed in N_2 saturated 0.5 M H_2SO_4 solution at a potential scan rate of 5 mV s^{-1} . In comparison with the un-oxidized carbon, the oxidized carbon exhibits well-defined redox peaks at about 0.55 V (NHE). These characteristic peaks are associated with the quinone-hydroquinone redox couple [43].

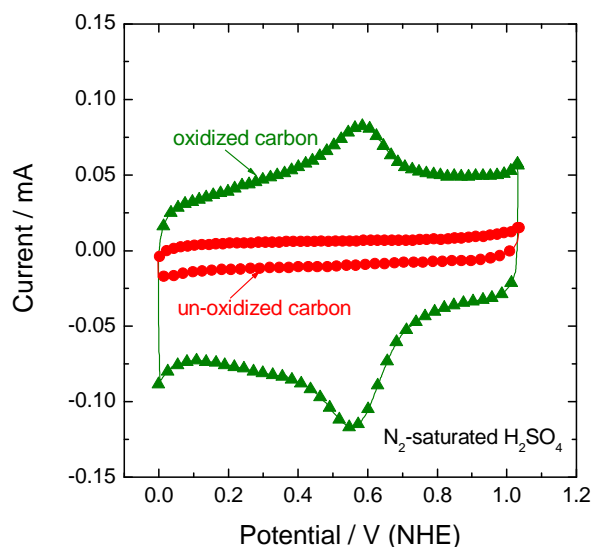


Figure 3-1-1. Cyclic voltammograms of the un-oxidized and oxidized carbons. The measurements were performed in N_2 saturated 0.5 M H_2SO_4 solution using a potential scan rate of 5 mV s^{-1} .

Figure 3-1-2 shows the polarization curves of oxygen reduction on the un-oxidized and oxidized carbons. The RRDE measurements were performed in O_2 saturated 0.5 M H_2SO_4 solution at a potential scan rate of 5 mV s^{-1} and a rotation speed of 900 rpm. The un-oxidized carbon exhibited very low activity for oxygen reduction. With the introduction of oxygen-containing groups on carbon surface by HNO_3 treatment, the activity of carbon black for oxygen reduction increases. This is attributed to the presence of quinone type groups [43-45].

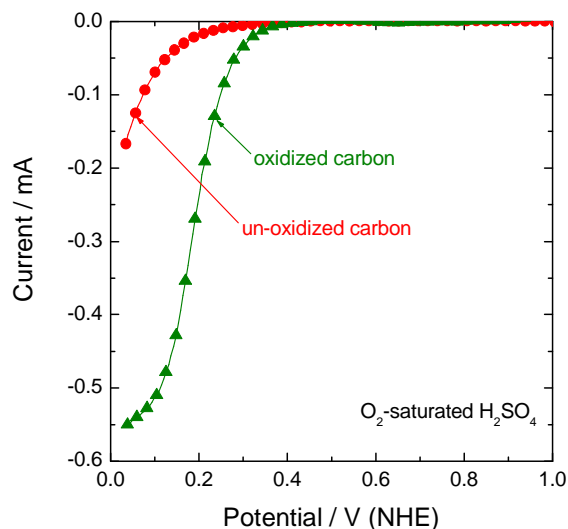


Figure 3-1-2. Polarization curves of oxygen reduction on the un-oxidized and oxidized carbons. The measurements were performed in O_2 saturated 0.5 M H_2SO_4 solution using a potential scan rate of 5 mV s^{-1} and a rotation speed of 900 rpm.

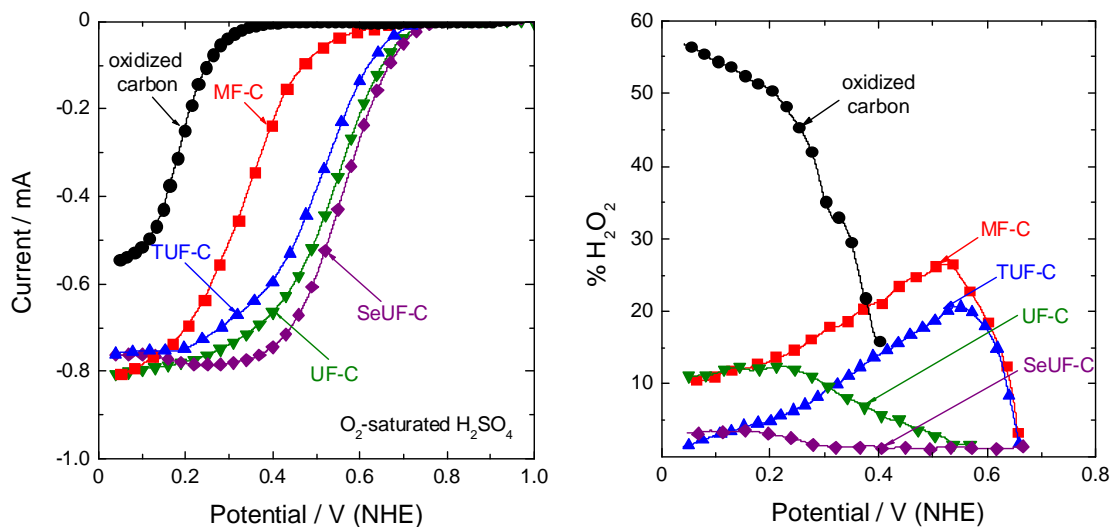


Figure 3-1-3. (a) Polarization curves of oxygen reduction and (b) percentages of H_2O_2 formed during oxygen reduction on carbon-based catalysts modified with different nitrogen donors and heat-treated at $800 \text{ }^\circ\text{C}$. For comparison, the curve measured on the oxidized carbon was also shown. The measurements were performed in O_2 saturated 0.5 M H_2SO_4 solution using a potential scan rate of 5 mV s^{-1} and a rotation speed of 900 rpm.

Figure 3-1-3a shows the polarization curves of oxygen reduction on carbon-based catalysts modified with different nitrogen donors and heat-treated at 800 °C. It was observed that the onset potential of oxygen reduction on melamine formaldehyde modified carbon (MF-C) shifts positively by about 0.3 V (NHE) compared to the oxidized carbon, which does not contain nitrogen. The activity of catalysts for oxygen reduction further increases when the carbon was modified with thiourea formaldehyde (TUF), urea formaldehyde (UF), and selenourea formaldehyde (SeUF) resins, respectively. The onset potentials of oxygen reduction on these catalysts are approximately 0.7 to 0.8 V (NHE).

Figure 3-1-3b shows the amount of H₂O₂ generated during oxygen reduction on carbon based catalysts modified with different nitrogen donors and heat-treated at 800 °C. It is evident that the nitrogen modification significantly decrease the percentage of H₂O₂ produced during oxygen reduction in comparison with oxidized carbon.

Table 3-1-1. The amount of H₂O₂ produced at 0.5 V (NHE) during oxygen reduction on carbon-based catalysts modified with different nitrogen donors and heat-treated at 800 °C.

Nitrogen-modified carbon-based catalyst	% H ₂ O ₂
MF-C	28
TUF-C	17
UF-C	3
SeUF-C	1

Table 3-1-1 summarizes the amount of H₂O₂ produced at 0.5 V (NHE) during ORR on the carbon-based catalysts modified with different nitrogen donors. The amounts of H₂O₂ generated on MF-C and TUF-C at 0.5 V (NHE) are about 28% and 17%, respectively due to the presence of nitrogen groups. In the case of UF-C and SeUF-C, it further decreases to approximately 1-3% under our experiment conditions. These results indicated that the modification of nitrogen groups onto the oxidized carbon can greatly improves the activity and selectivity of carbon substrate towards oxygen reduction. Since UF-C and SeUF-C exhibited the optimum catalytic performances, the following study will be focused on these two samples.

Table 3-1-2 summarizes the BET surface areas of different samples: un-oxidized carbon, oxidized carbon, UF-C, and SeUF-C. The un-oxidized carbon has a surface area of 915 m² g⁻¹.

After HNO₃ treatment, the surface area decreases to 694 m² g⁻¹ due to the destruction of micro- and meso-pores. After modification with nitrogen-containing polymer and subsequent heat-treatment, a further reduction in the surface area was observed for UF-C and SeUF-C. Moreover, the higher BET surface area of SeUF-C than that of UF-C may at least partially explain the slightly higher catalytic performance of SeUF-C compared to UF-C (see Fig. 3-1-3).

Table 3-1-2. BET surface areas of different samples.

Sample	BET surface area (m ² g ⁻¹)
Un-oxidized carbon	915
Oxidized carbon	694
UF-C (heat-treated)	321
SeUF-C (heat-treated)	496

Figure 3-1-4 shows the polarization curves of oxygen reduction on SeUF-C heat-treated at different temperatures. It can be seen that the activity of SeUF-C is strongly dependent on the heat-treatment temperature and the optimum temperature is 800 °C. The same tendency was also observed for UF-C.

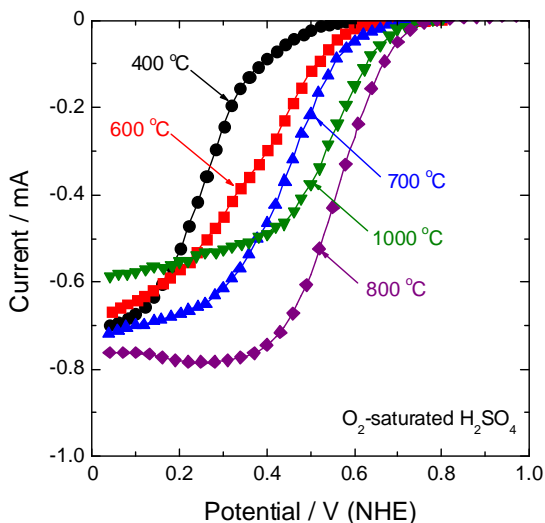


Figure 3-1-4. Polarization curves of oxygen reduction on SeUF-C heat-treated at different temperatures between 400 and 1000 °C. The measurements were performed in O₂ saturated 0.5 M H₂SO₄ solution using a potential scan rate of 5 mV s⁻¹ and a rotation speed of 900 rpm.

Figs. 3-1-5a and 5b show the XRD patterns of UF-C and SeUF-C before and after heat-treatment at 800 °C, respectively. The XRD patterns recorded before heat-treatment exhibit characteristic peaks corresponding to Se and/or UF in addition to a broad diffraction peak from carbon black. Upon heat-treatment, the diffraction peaks for carbon black become sharper indicating an increased graphitization. Moreover, only diffraction peaks from carbon were observed for heat-treated carbon-based catalysts. No any metal species was detected. TEM image shown in Fig. 3-1-6 further confirmed the absence of any metal in the catalytic structure. The ICP-MS analysis was carried out to analyze the bulk transition metals in UF-C and SeUF-C (see Table 3-1-3). A trace of transition metals was detected by University of Illinois at Urbana-Champaign.

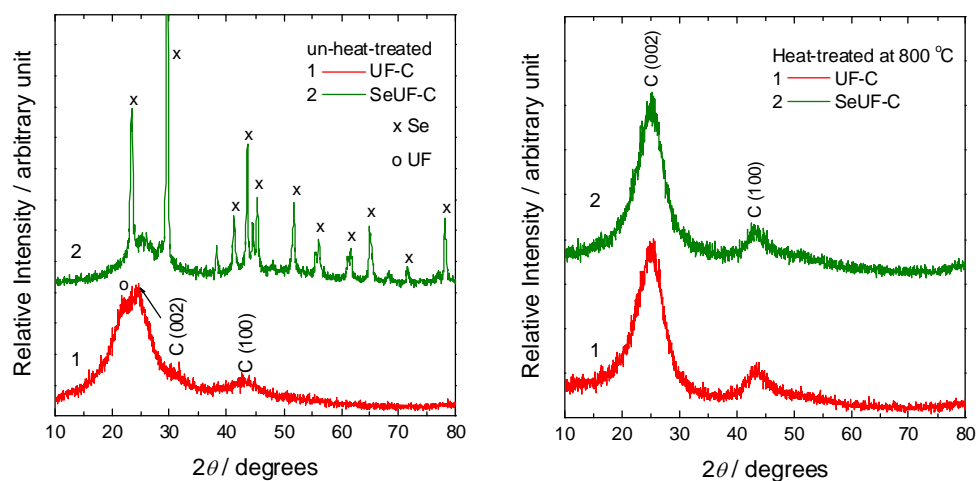


Figure 3-1-5. XRD patterns of UF-C and SeUF-C: (a) before and (b) after heat-treatment.

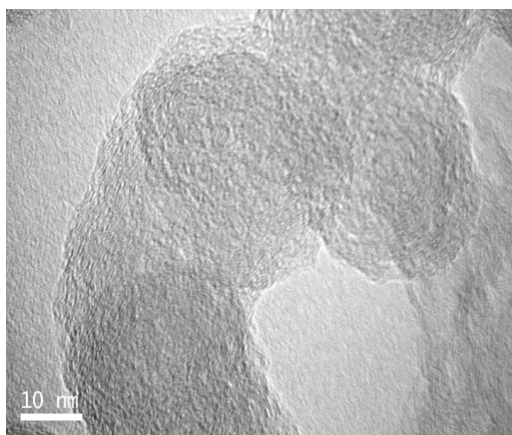


Figure 3-1-6. TEM image of SeUF-C heat-treated at 800 °C.

No metal impurities were observed for the same catalysts by Yonsei University. These results indicated that only nitrogen-modified carbon-based structures are responsible for the observed catalytic activity of UF-C and SeUF-C for oxygen reduction.

Table 3-1-3. Bulk transition metal concentrations in UF-C and SeUF-C determined by ICP-MS.

Catalysts	Fe (wt %)	Co (wt %)
UF-C	0.00004 ^a	0.00003 ^a
	0 ^b	0 ^b
SeUF-C	0.00002 ^a	0.000006 ^a
	0 ^b	0 ^b

^a Measured by University of Illinois at Urbana-Champaign;

^b Measured by Yonsei University, Korea

Fig. 3-1-7a shows the polarization curve of the H₂-O₂ PEM fuel cell prepared with the UF-C cathode catalyst (UF-C loading: 6.0 mg cm⁻²). The testing was run at 75 °C with the H₂/O₂ back pressures of 30 and 40 psi, respectively. For comparison, the fuel cell performance prepared with 20 wt % Pt/C catalyst (Pt/C loading: 0.1 mg cm⁻²) was also presented. The UF/C shows current density of 1.06 A cm⁻² at 0.2 V; however, its performance is much lower than Pt/C counterpart. It is due to the lower intrinsic activity of UF-C for ORR in comparison with Pt/C. Another reason is that the large thickness of UF-C based catalyst layer causes high electrical resistance and mass transfer resistance.

As shown in Fig. 3-1-7b, the thickness of UF-C based catalyst layer with catalyst loading of 6 mg cm⁻² is approximately 90 μm, while it is generally 3-5 μm for Pt/C based catalyst layer with catalyst loading of 0.1 mg cm⁻². Fig. 3-1-7c shows the stability testing of UF-C catalyst at 0.4 V. The cathode catalyst loading is 4.0 mg cm⁻², and the H₂/O₂ back pressures are 30 and 30 psi, respectively. It can be seen that the UF-C based fuel cell shows a stable current profile with current density of approximately 0.12 A cm⁻² up to 200 h.

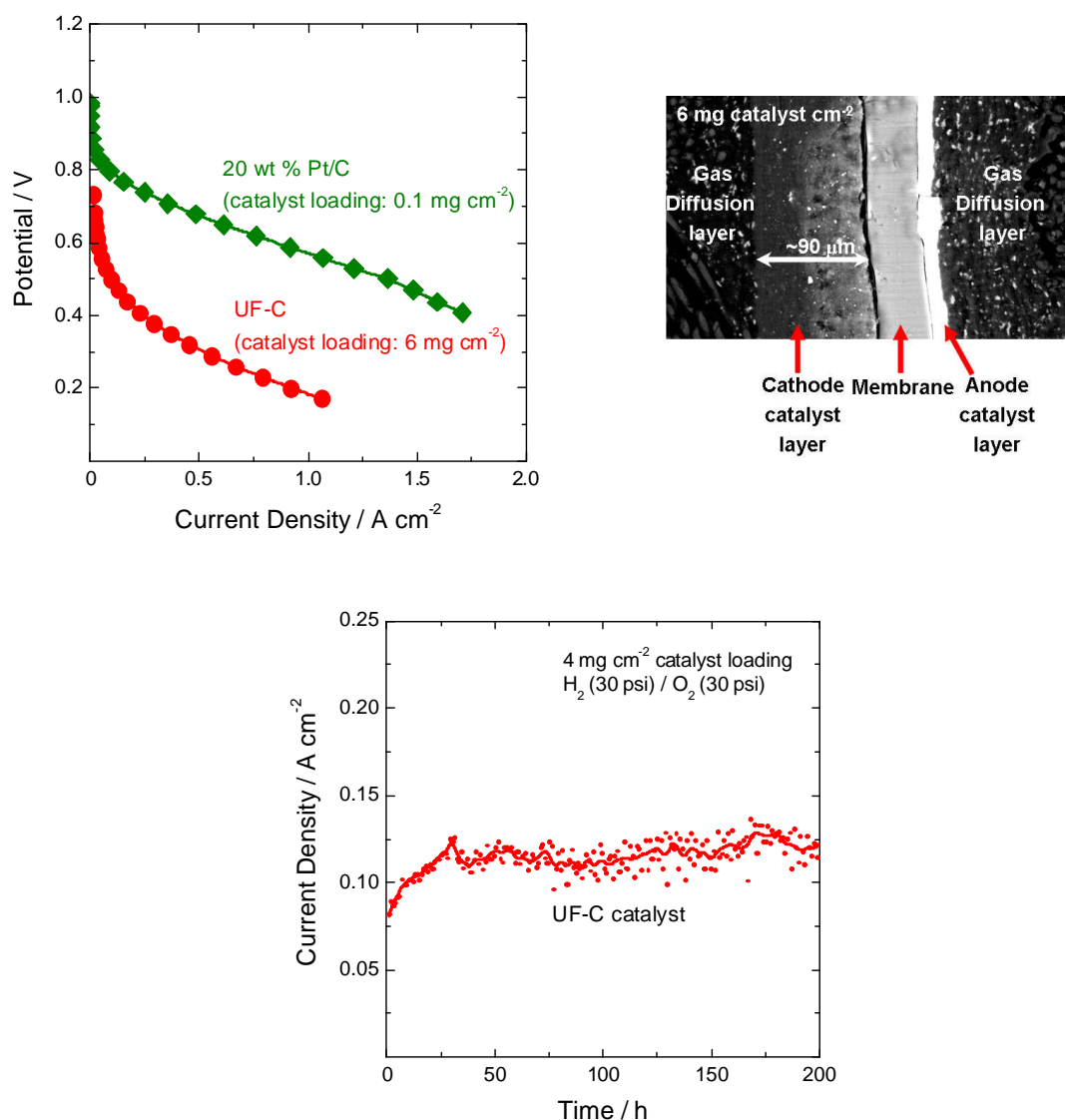


Figure 3-1-7. Polarization curve of the H₂-O₂ PEM fuel cells prepared with UF-C and 20 wt% Pt/C catalysts, respectively. UF-C loading: 6 mg cm⁻²; Pt/C loading: 0.1 mg cm⁻²; H₂/O₂ back pressures: 30 psi/40 psi; operation temperature: 75 °C. (b) SEM image of the cross-section of the MEA prepared with UF-C catalyst. (c) Current transient (stability test) at 0.4 V of the H₂-O₂ PEM fuel cell prepared with UF-C catalyst. Catalyst loading: 4 mg cm⁻²; H₂/O₂ back pressures: 30 psi/30 psi; operation temperature: 75 °C.

3.1.2. Discussion of Active Sites

Table 3-1-4 provides the summary of surface composition of different samples determined by XPS. It was observed that the oxidized carbon has high oxygen concentration on the surface

which was introduced by HNO₃ oxidation. After the polymerization on the oxidized carbon, the nitrogen concentration on the surface of carbon substrates increases. However, heat treatment at 800 °C can decrease the nitrogen concentration since the nitrogen can be partially removed in the form of small nitrogen-containing molecules at elevated temperature.

Table 3-1-4. Surface compositions of different samples determined by XPS.

Sample	Surface concentration (wt %)			
	C	N	O	Se
Oxidized carbon	95.0	-	5.0	-
UF-C (un-heat-treated)	88.2	8.4	3.4	-
UF-C (heat-treated)	92.4	2.2	5.4	-
SeUF-C (un-heat-treated)	89.6	5.8	3.5	1.1
SeUF-C (heat-treated)	92.3	2.4	5.1	0.2

XPS analysis was used to study the nature of nitrogen surface groups on the carbon support. The three common nitrogen groups observed in nitrogen containing carbonaceous materials are the pyridinic (ca. 398.6 eV), pyrrolic (ca. 400.3 eV) and graphitic nitrogen groups (ca. 401.1 – 403.6 eV) [46-48]. Pyridinic nitrogen refers to the nitrogen atom bonded to two carbon atoms on the edge of graphite planes that is capable of adsorbing molecular oxygen and its intermediates in oxygen reduction reaction. It has one lone pair of electrons in addition to the one electron donated to the conjugated π bond system, imparting Lewis basicity to the carbon. Graphitic nitrogen, which is sometimes termed “quaternary” nitrogen, represents the nitrogen atom bonded to three carbon atoms within a graphite (basal) plane. Pyrrolic groups refer to nitrogen atoms that contribute to the π system with two p-electrons.

Fig. 3-1-8 shows the XPS spectra of N1s region obtained for SeUF-C heat-treated at 600–1000 °C. The XPS spectrum for the catalyst heat-treated at 600 °C exhibits the three nitrogen groups, i.e., pyridinic, pyrrolic, and graphitic nitrogens. When the catalyst was heat-treated at 800 °C, the peak for the pyrrolic nitrogen is no longer observed from the XPS data. Increasing the heat-treatment temperature from 800 to 1000 °C transforms more of the pyridinic nitrogen to graphitic nitrogen. It should be noted that the sample heat-treated at 800 °C has larger fraction of the pyridinic nitrogen group compared to the pyrrolic and graphitic groups and it shows the

highest activity. This indicated that the pyridinic nitrogen group is active for oxygen reduction and the catalyst heat-treated at 800 °C has more active sites (pyridinic nitrogen) to facilitate oxygen adsorption.

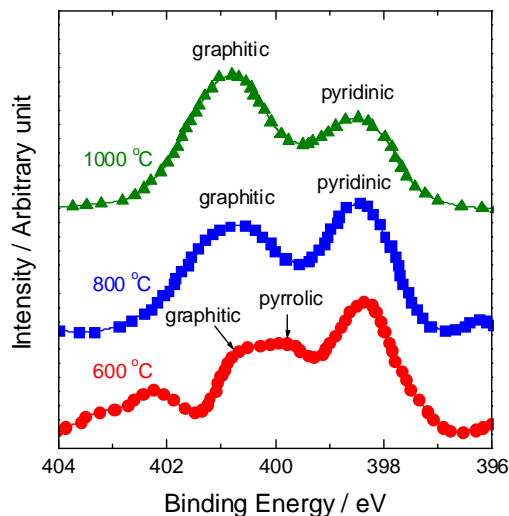


Figure 3-1-8. XPS spectra of N 1s region obtained for SeUF-C heat-treated at 600–1000 °C

It is conceivable that the nitrogen atoms are attached onto the surface of the oxygen-rich (oxidized) carbon in the form of pyridinic and pyrrolic structures. During the subsequent heat-treatment step, carbon surface becomes richer in pyridinic nitrogen that enhances the activity of the catalyst for oxygen reduction. In the past, the general conception is that pyridinic nitrogen groups coordinated with a metal atom is responsible for the activity of non-precious metal catalysts. However, we observed that pyridinic N-rich carbon without metal is active for oxygen reduction since transition metal is not present on the surface of our catalysts.

According to Ref. [29, 30], after heat-treatment at 800 °C in argon for Co-TMPP and Fe-TMPP, no Co or Fe was detected in the Mössbauer spectra in a form corresponding to coordination with nitrogen, thus indicating loss of the metal-N₄ centers. The macrocycle structure is rather completely destroyed after heat-treatment at temperatures of 800-900 °C [49-51]. It was suggested that the transition metal does not act as an active site for oxygen reduction, but rather it serves primarily to facilitate the stable incorporation of nitrogen into the graphitic structure during high-temperature pyrolysis of metal-nitrogen complexes [29, 30].

Using a semi-empirical quantum chemical method, Strelko et al. [52] have shown that availability of 4–6% oxygen heteroatoms of furan and pyrone-type and/or also 2–3% N of pyrrolic-type in a carbon matrix provide the greatest electron-donor ability to carbons. Two mechanisms

of chemisorptions of oxygen on evacuated carbons were suggested namely: homolytic (free radical) at small degrees of filling of a surface by oxygen, and heterolytic (at large degrees of filling) causing the fixation of oxygen on a surface in the form of a superoxide ion $O_2^{\cdot-}$.

According to Maldonado and Stevenson [53], on nitrogen doped carbon nanofiber electrodes, the oxygen reduction reaction can be treated as a catalytic regenerative process where the intermediate hydroperoxide (HO_2^-) is chemically decomposed to regenerate oxygen. They have supported the proposed mechanism by electrochemical simulation and by measured difference in hydroperoxide decomposition rate constants. The results indicated that remarkable 100-fold enhancement for hydroperoxide decomposition for N-doped carbon nanofibers. The authors have concluded that exposed edge plane defects and nitrogen doping are important factors for influencing adsorption of reactive intermediates and for enhancing electrocatalysis for the oxygen reduction at nanostructured carbon electrodes. Our experimental studies indicate that a strong Lewis basicity of carbons doped with pyridinic and graphitic nitrogens facilitates the reductive adsorption reaction of O_2 without the irreversible formation of oxygen functionalities, due to an increased electron-donor property of carbon.

3.1.3. Summary

This work showed that carbon-based catalysts for oxygen reduction can be synthesized by introducing oxygen and nitrogen groups from various nitrogen precursors. The nature of nitrogen surface groups and the effect of pyrolysis temperature on the activity of the catalyst have been evaluated. XPS indicated that high concentration of pyridinic type nitrogen groups doped on graphitic carbon increase the activity of catalysts. The carbon-based catalysts showed an onset potential at around 0.78 V (NHE) and the amount of H_2O_2 generated during oxygen reduction was approximately 1-3 % at 0.5 V (NHE). On the carbon surface, pyridinic (quaternary) and graphitic nitrogens act as catalytic sites for oxygen reduction: particularly, pyridinic nitrogen, which possesses one lone pair of electrons in addition to the one electron donated to the conjugated μ bond, facilitates the reductive oxygen adsorption and eliminates H_2O_2 formation.

3.2. CARBON COMPOSITE CATALYSTS SYNTHESIZED IN THE PRESENCE OF IRON AND COBALT PRECURSORS

3.2.1. Electrocatalytic Properties of Metal-Free Catalysts

Carbon-based metal-free catalysts were synthesized by modifying the porous carbon black with the surface functional groups such as oxygen and nitrogen. Nitrogen groups were incorporated into the graphitic structure using polymerization of low-cost organic precursors (e.g., melamine-formaldehyde, urea-formaldehyde, and selenourea-formaldehyde) and thermal/chemical activation processes. The activity and selectivity for four-electron oxygen reduction were studied as a function of: (i) carbon support, (ii) surface oxygen groups, (iii) nitrogen content, (iv) pyrolysis temperature, (v) porosity, and (vi) pore size distribution.

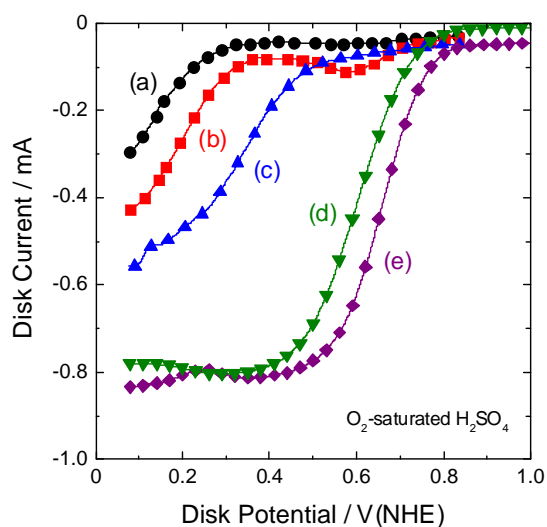


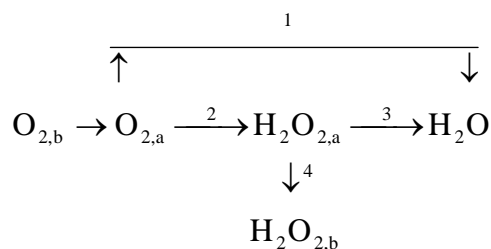
Figure 3-2-1. Polarization curves on the rotating disk electrodes for the carbon (Ketjen) blacks treated by various methods: (a) as-received carbon, (b) HNO_3 -treated carbon, (c) NH_3 -treated carbon, (d) urea-formaldehyde-modified carbon, and (e) selenourea-formaldehyde-modified carbon. The measurements were performed in 0.5 M H_2SO_4 solution saturated with O_2 using a potential scan rate of 5 mV s^{-1} and a rotation speed of 900 rpm.

Figure 3-2-1 presents polarization curves observed on the rotating disk electrodes for the carbon blacks treated by various methods. The RRDE measurements were performed in 0.5 M H_2SO_4 solution saturated with O_2 using a potential scan rate of 5 mV s^{-1} and a rotation speed of 900 rpm. For comparison, the curve measured on the as-received Ketjen black is also shown in Fig. 3-2-1. The as-received carbon (curve “a”) does not show any catalytic activity towards

oxygen reduction. The carbon oxidized with HNO₃ (curve “b”) exhibits higher catalytic activity compared with the as-received carbon. The increased activity is attributed to the oxygen functional groups of quinone/hydroquinone generated on the carbon surface during HNO₃ treatment [32, 34].

Remarkable increase in the catalytic activity towards oxygen reduction has been achieved with the introduction of nitrogen groups. The metal-free catalysts synthesized by novel methodologies with organic N-precursors (curves “d” and “e”) show improved performance when compared with the conventional NH₃-treated carbon (curve “c”). For example, the metal-free catalyst prepared using selenourea-formaldehyde (curve “e”) exhibits an onset potential for oxygen reduction as high as 0.76 V(NHE) and also a well-defined diffusion limiting current which is only observed in Pt-based catalyst.

The oxygen reduction reaction proceeds by two pathways as follows:



where subscripts a and b denote the species adsorbed on the electrode surface and that in the bulk, respectively. O₂ may be directly reduced to H₂O through four-electron transfer (reaction 1). In parallel, O₂ may be reduced to H₂O₂ via two-electron transfer (reaction 2), followed by either reduction of H₂O₂ to H₂O (reaction 3) or transport of the adsorbed H₂O₂ to the bulk solution (reaction 4). H₂O₂ is believed to be responsible for the deterioration of MEA performance, since the polymer electrolyte membrane and the catalyst degrade over time due to attack by peroxide radicals [12].

Table 3-2-1 summarizes % H₂O₂ determined at 0.5 V (NHE) for the different metal-free catalysts. It is known that oxygen reduction to H₂O₂ is predominant on most of carbaceous materials, since the O-O bond breakage is not feasible. However, the metal-free catalysts, which had been used as a support in this study, generated 1 - 3 % H₂O₂ at 0.5 V (NHE) depending on the precursors used. In this study, the metal-free carbon modified with urea-formaldehyde was used as a support for preparation of the carbon composite catalyst.

Table 3-2-1. H₂O₂ percentages at 0.5 V (NHE) and number of electrons (n) transferred during oxygen reduction on the metal-free catalysts.

Organic precursor used for metal-free catalyst preparation	% H ₂ O ₂	n
Melamine-formaldehyde	28	3.2
Urea-formaldehyde	3	3.6
Selenourea-formaldehyde	1	4.0

3.2.2. Electrocatalytic Properties of Carbon Composite Catalyst

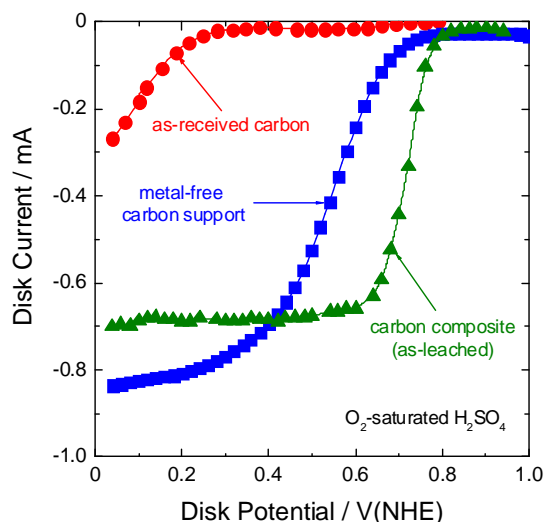


Figure 3-2-2. Polarization curves on the rotating disk electrodes for the as-received carbon, the metal-free catalyst and the carbon composite catalyst (as-leached). The measurements were performed in 0.5 M H₂SO₄ solution saturated with O₂ using a potential scan rate of 5 mV s⁻¹ and a rotation speed of 900 rpm.

The carbon composite catalyst was prepared as follows: (i) the Co₁Fe₁N_x deposition on the metal-free carbon support, (ii) the pyrolysis at 900 °C, and (iii) the chemical leaching in 0.5 M H₂SO₄ solution at 90 °C. Figure 3-2-2 shows typical polarization curves on the rotating disk electrodes for the metal-free carbon catalyst and the as-leached carbon composite catalyst. The RRDE measurements were performed in 0.5 M H₂SO₄ using a rotation speed of 900 rpm. For

comparison, the curve measured on the as-received carbon is also presented in Figure 3-2-2. The as-received carbon did not show any catalytic activity toward oxygen reduction. The metal-free carbon catalyst exhibited much higher activity when compared with the as-received carbon. The increased activity is attributed to the oxygen and nitrogen functional groups introduced on the carbon surface. A further improvement in the activity was achieved with the pyrolysis in the presence of $\text{Co}_1\text{Fe}_1\text{N}_x$ complex, followed by the chemical leaching treatment. The carbon composite catalyst showed an onset potential for oxygen reduction as high as 0.87 V (NHE) and also a well-defined diffusion limiting current.

Table 3-2-2. H_2O_2 percentages determined at different disk potentials for the metal-free catalyst, the as-pyrolized carbon composite catalyst, the as-leached carbon composite catalyst, and the conventional Pt/C catalyst (20 wt% Pt, E-TEK).

Disk potential, V (NHE)	% H_2O_2			
	Metal-free carbon support	As-pyrolized carbon composite	As-leached carbon composite	Pt/C
0.6	0	9.3	1.1	0.4
0.5	1.2	7.1	0.9	0.4
0.4	4.0	6.1	0.7	0.7

Table 3-2-2 summarizes % H_2O_2 as a function of disk potential determined for the different catalysts: (i) the metal-free carbon support, (ii) the as-pyrolized carbon composite catalyst, (iii) the as-leached carbon composite catalyst, and (iii) the conventional Pt/C catalyst (20 wt% Pt, E-TEK). The as-pyrolized carbon composite catalyst produced a relatively large amount of H_2O_2 , due probably to excess transition metals on the carbon support as discussed in the following section. Upon the subsequent removal of excess metal elements, the H_2O_2 amount decreased to a level less than 2 %. Notice that the Pt catalyst generated 1 to 2 % H_2O_2 . To our knowledge, such a high selectivity has not been reported for any of transition metal-based or carbon-based catalysts.

Figure 3-2-3 presents the polarization curves of PEM fuel cells prepared with the different cathode catalysts: (i) the metal-free carbon support, (ii) the as-pyrolized carbon composite catalyst, and (iii) the as-leached carbon composite catalyst. The cathode catalyst loadings were maintained at 6.0 mg cm^{-2} . The experiments were performed using 30 psi (2.0 atm) back pressure on both anode and cathode compartments. Ohmic potential drop was not compensated for in the measurement. As expected from the RRDE results (Fig. 3-2-2), the fuel cell performance increased gradually after the pyrolysis and the chemical leaching. Particularly, it should be noted that the subsequent dissolution of Co and Fe metals from the as-pyrolized catalyst does not cause any activity loss, but rather increases the activity. The PEM fuel cell with the as-leached carbon composite catalyst showed the current density of 2.3 A cm^{-2} at 0.2 V .

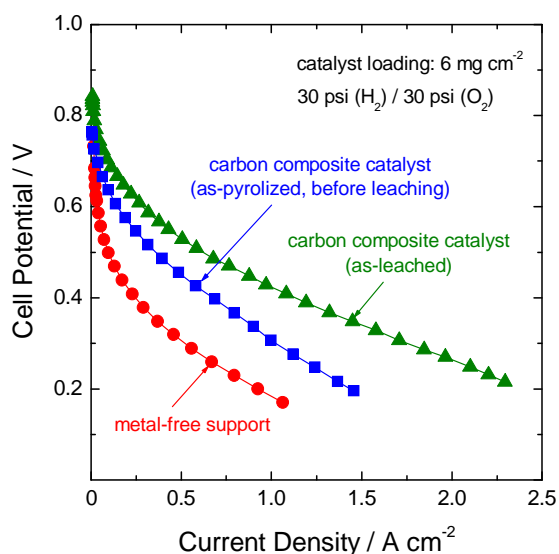


Figure 3-2-3. Polarization curves of PEM fuel cells prepared with the different cathode catalysts: the metal-free catalyst, the as-pyrolized carbon composite catalyst, and the as-leached carbon composite catalyst. The cathode catalyst loadings were maintained at 6.0 mg cm^{-2} . The experiments were performed using 30 psi back pressure on both anode (H_2) and cathode (O_2) compartments.

The carbon composite catalysts were synthesized by the deposition of the metal-nitrogen complexes with different compositions (i.e., FeN_x , CoN_x , $\text{Co}_1\text{Fe}_3\text{N}_x$, $\text{Co}_3\text{Fe}_1\text{N}_x$, and $\text{Co}_1\text{Fe}_1\text{N}_x$), followed by the pyrolysis and the chemical leaching. The fuel cell test results are summarized in Figure 3-2-4(a). As shown in Fig. 3-2-4(a), the use of Co-Fe-N complex resulted in an improved activity when compared with Co-N and Fe-N complexes, and the maximum performance was

achieved for $\text{Co}_1\text{Fe}_1\text{N}_x$. The fuel cell performances of the optimized carbon composite catalyst were presented in Fig. 3-2-4(b) for various cathode loadings of 2.0 – 6.0 mg cm^{-2} .

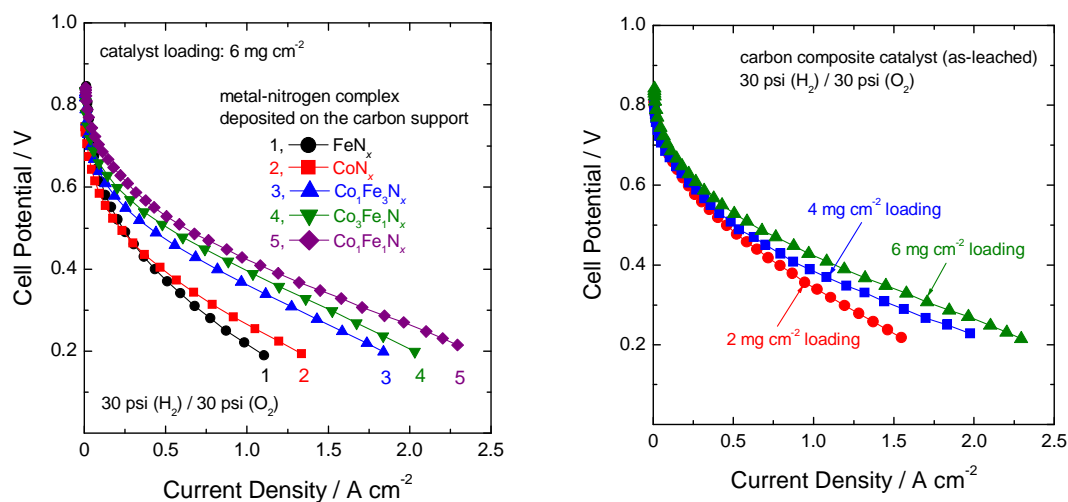


Figure 3-2-4. (a) Polarization curves of PEM fuel cells prepared with the carbon composite catalysts. The catalysts were prepared using the metal-nitrogen complexes with different compositions. All the catalysts were subjected to the chemical leaching. The cathode catalyst loading was 6.0 mg cm^{-2} . (b) PEM fuel cell performances for different loadings of the optimized carbon composite catalyst. The experiments were performed using 30 psi back pressure on both anode (H_2) and cathode (O_2) compartments.

The electrochemical characterization studies show that the new method involving the $\text{Co}_1\text{Fe}_1\text{N}_x$ deposition followed by the pyrolysis and the chemical leaching produces the carbon composite catalyst with superior catalytic activity and selectivity to any of non-precious metal catalysts reported in the literature [7-27].

3.2.3. Characterizations of Metal-Nitrogen Complexes and Metallic Species in Carbon Composite Catalysts

Figure 3-2-5 demonstrates the k^1 -weighted EXAFS spectra in R space for the carbon composite catalysts pyrolyzed at various temperatures. The catalyst was prepared by the CoN_x deposition onto the metal-free carbon support, followed by the pyrolysis. No chemical leaching was conducted on the pyrolyzed catalysts. For comparison, a reference spectrum for a pure cobalt foil is given in Fig. 3-2-5. As indicated in Fig. 3-2-5, the major two peaks centered at R values of ca. 1.2 and 2.1 \AA correspond to the Co-N and Co-Co interactions, respectively.

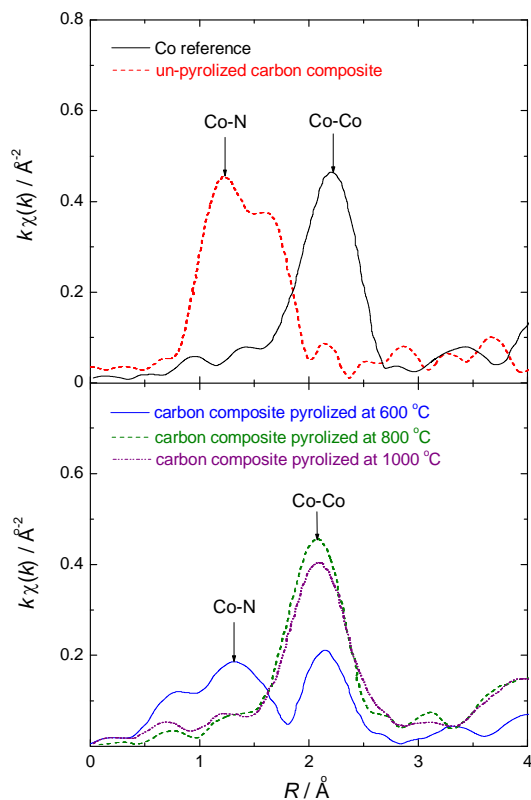


Figure 3-2-5. k_1 -weighted EXAFS data for the carbon composite catalysts pyrolyzed at various temperatures. The catalyst was prepared by the CoN_x deposition onto the metal-free carbon support, followed by the pyrolysis. No chemical leaching was conducted on the pyrolyzed catalysts.

The EXAFS spectrum for the un-pyrolized catalyst shows only a dominant Co-N peak, which confirms the presence of the Co species coordinated with nitrogen groups on the carbon surface. The Co-Co peak becomes strong with increasing the pyrolysis temperature, and only a Co-Co peak is observed when the catalyst was pyrolyzed at 800 and 1000 °C. This means that the CoN_x chelate complexes decompose at high pyrolysis temperatures above 800 °C, resulting in the formation of the metallic Co species. The EXAFS analysis supports the experimental finding of Yeager et al. [29] that after the heat-treatment of Co-TMPP and Fe-TMPP at 800 °C, neither Co nor Fe was detected in the Mössbauer spectra in a form corresponding to coordination with nitrogen. Therefore, it is clear that the metal-nitrogen complexes are not responsible for the observed activity for oxygen reduction in Figs. 3-2-2, 3, 4. As a matter of fact, the dissolution of metallic species from the as-pyrolyzed catalyst increases the activity as presented in Fig. 3-2-3.

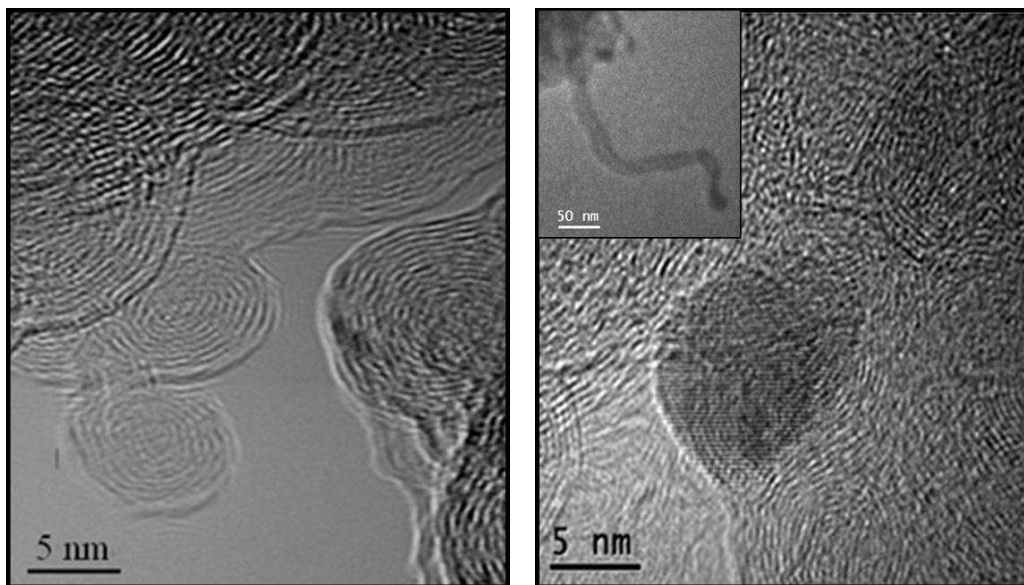


Figure 3-2-6. TEM images of (a) the metal-free carbon support and (b) the carbon composite catalyst. The carbon composite catalyst was subjected to the chemical leaching.

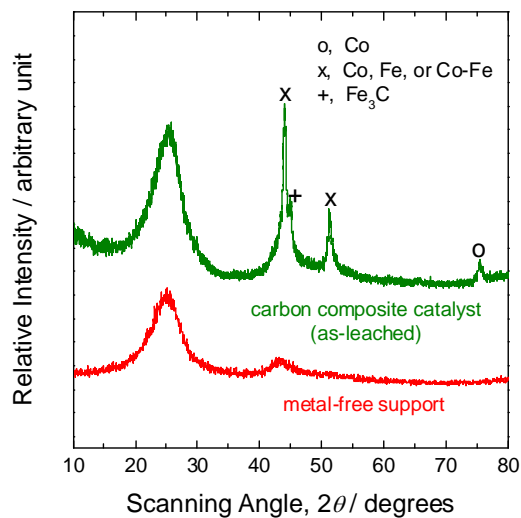


Figure 3-2-7. Powder XRD patterns of the metal-free catalyst and carbon composite catalyst. The carbon composite catalyst was subjected to the chemical leaching.

Figures 3-2-6(a) and (b) present the TEM images of the metal-free catalyst and the carbon composite catalyst, respectively. The carbon composite catalyst was prepared as follows: (i) the $\text{Co}_1\text{Fe}_1\text{N}_x$ deposition on the metal-free carbon support, (ii) the pyrolysis at 900 °C, and (iii) the chemical leaching in 0.5 M H_2SO_4 solution at 90 °C. Comparing the two TEM images, it is seen that a metal particle was covered with graphitic layers of the carbon composite catalyst, and a nanostructured tube or fiber of graphitic carbon was formed as a result of the pyrolysis in the presence of Co and Fe metals [40]. Figure 3-2-7 compares the powder XRD patterns for the metal-free catalyst and the carbon composite catalyst. The XRD pattern for the carbon composite catalyst shows the characteristic diffraction peaks that can be assigned to a mixture of the metallic phases (i.e., Co, Fe and Co_xFe_y) and to the cementite phase (Fe_3C).

Table 3-2-3. Concentrations of Co and Fe in the carbon composite catalyst obtained before and after the chemical leaching in 0.5 M H_2SO_4 solution at 90 °C, determined by ICP-MS and XPS.

Analytical technique		Concentration (wt %)	
		Co	Fe
ICP-MS	(before leaching)	10.4	9.6
	(after leaching)	4.6	1.4
XPS	(after leaching)	0	0

Table 3-2-3 summarizes the concentrations of Co and Fe in the carbon composite catalyst obtained after the chemical leaching in H_2SO_4 solution. The concentrations were determined by ICP-MS and XPS techniques. ICP-MS analysis shows that the concentrations of Co and Fe decreased from 10.4 to 4.6 wt% and from 9.6 to 1.4 wt%, respectively, upon the chemical leaching. XPS detected no metal traces from the leached carbon composite catalyst. Since the escape depth of photoelectrons is a few nanometers, XPS analysis provides only the surface composition of the carbon composite catalyst. Therefore, the composition analysis by two techniques indicates that Co and Fe particles on the pyrolyzed catalyst surface were removed by the subsequent chemical treatment in H_2SO_4 solution, whereas metal particles encased in the carbon structure survived the leaching treatment as indicated in Figs. 3-2-6(b) and 7.

In summary, the materials characterization studies indicate that (i) the metal-nitrogen chelate complexes are not stable at high temperatures above 800 °C, (ii) no metallic species is present on

the catalyst surface after chemical post-treatment, and (iii) the carbon surface is responsible for the observed activity for oxygen reduction.

3.2.4. Characterizations of Nitrogen Functional Groups on Carbon Composite Catalysts

The nature of nitrogen functional groups was identified using XPS at each synthesis step: (a) after the deposition of $\text{Co}_1\text{Fe}_1\text{N}_x$ complex onto the support, (b) after the pyrolysis at 900 °C, and (c) after the chemical leaching in 0.5 M H_2SO_4 solution at 90 °C. The results are summarized in Table 3-2-4 along with the nitrogen content and the fuel cell performance of each sample. The current density and the amount of H_2O_2 were determined at 0.4 V in a fuel cell (Fig. 3-2-3) and an RRDE (Table 3-2-2), respectively. The activity was determined to be almost zero for the non-pyrolyzed catalyst, but the activity and selectivity gradually increased after the pyrolysis and the chemical post-treatment.

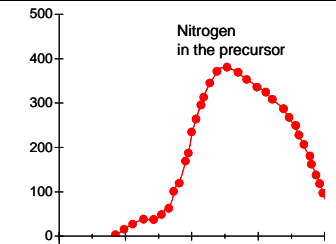
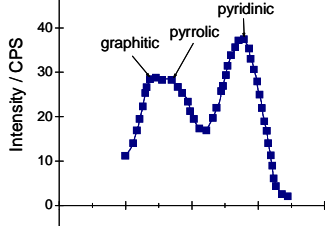
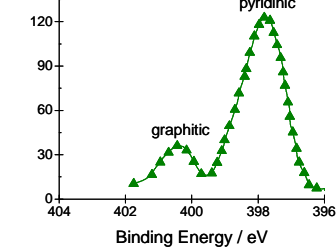
The XPS spectrum obtained after the $\text{Co}_1\text{Fe}_1\text{N}_x$ deposition exhibits a broad peak around 398.9 eV that corresponds to the nitrogen groups of the ternary amine-type. The data indicate that the high-temperature pyrolysis induces a significant loss of nitrogen from 9.9 to 2.6 wt%. Upon pyrolysis, the peak splits into three broad peaks at ca. 398.5, 400.5 and 401.1 eV that can be assigned to “pyridinic” nitrogen, “pyrrolic” nitrogen, and “graphitic” nitrogen, respectively. Finally, the XPS spectrum obtained after the chemical leaching shows no dominant peak for pyrrolic nitrogen.

Pyridinic nitrogen refers to the nitrogen atom bonded to two carbon atoms on the edge of graphite planes that is capable of adsorbing molecular oxygen and its intermediates in the oxygen reduction reaction. It has one lone pair of electrons in addition to the one electron donated to the conjugated π bond system, imparting Lewis basicity to the carbon [53]. Graphitic nitrogen, which is sometimes termed “quaternary” nitrogen, represents the nitrogen atom bonded to three carbon atoms within a graphite (basal) plane.

Recently, Sidik et al. [31] performed the quantum mechanical calculations for oxygen reduction on cluster models of graphite sheets containing substitutional nitrogen (i.e., graphitic nitrogen), and they showed that in acidic media, oxygen reduction is activated to some extent by radical carbon sites formed adjacent to graphitic nitrogen atoms in the basal plane. Using a semi-empirical quantum chemical simulation, Strelko et al. [54] have shown that the highly occupied molecular orbital level (E_{HOMO}) of carbon has a maximum for a nitrogen doping level of ca. 3 % providing the high electron-donor ability to carbons. Also, two mechanisms of oxygen

chemisorptions on evacuated carbons were suggested: namely, hemolytic (free radical) of a small degree of filling of the surface by oxygen, and heterolytic (large degree of filling) causing the fixation of oxygen on a surface in the form of a superoxide ion O_2^{*-} .

Table 3-2-4. Catalytic activity, selectivity, surface nitrogen concentration, and XPS spectrum at each synthesis step of the carbon composite catalyst. The current density and the amount of H_2O_2 were determined at 0.4 V in a fuel cell (6.0 mg cm^{-2} cathode catalyst loading, 30 psi back pressure) and an RRDE, respectively.

Step	Current Density ($A\ cm^{-2}$)	% H_2O_2	N content (wt%)	XPS
After metal-nitrogen complex deposition	~ 0	-	9.9	
After pyrolysis	0.7	6.1	2.6	
After chemical post-treatment	1.2	0.7	3.9	

According to Maldonado and Stevenson [53], on nitrogen doped carbon nanofiber electrodes, the oxygen reduction reaction can be treated as a catalytic regenerative process where the intermediate hydroperoxide (HO_2^-) is chemically decomposed to regenerate oxygen. They have supported the proposed mechanism by electrochemical simulation and by measured difference in

hydroperoxide decomposition rate constants. The results indicated a remarkable 100-fold enhancement for hydroperoxide decomposition for nitrogen-doped carbon nanofibers. The authors have concluded that pyridinic nitrogen doping into edge plane defects is an important factor for influencing adsorption of reactive intermediates and for enhancing electrocatalysis for oxygen reduction at nanostructured carbon electrodes.

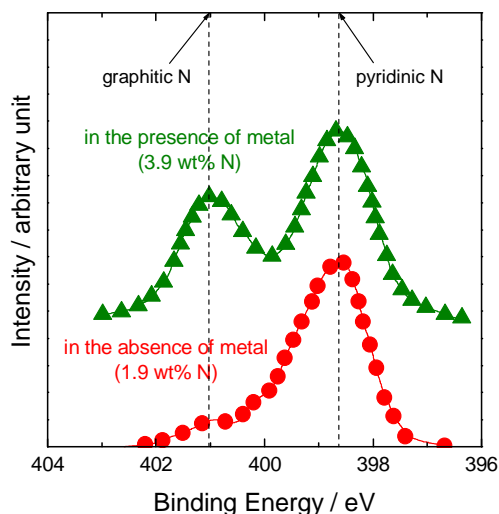


Figure 3-2-8. XPS spectra of N 1s region obtained for the catalysts pyrolyzed in the absence and presence of transition metals (Co and Fe). The carbon composite catalysts were subjected to the chemical leaching.

Consequently, the previous simulation analyses and our experimental studies indicate that a strong Lewis basicity of carbons doped with pyridinic and graphitic nitrogens facilitates the reductive adsorption reaction of O_2 without the irreversible formation of oxygen functionalities, due to an increased electron-donor property of carbon.

In order to further study the role of transition metals in facilitating the incorporation of nitrogen functional groups during the pyrolysis, the catalyst was prepared without using any transition metals as follows: ethylene diamine was adsorbed on the metal-free carbon support, followed by the pyrolysis at 900 °C and the chemical leaching in 0.5 M H_2SO_4 solution at 90 °C. The XPS data are presented in Fig. 3-2-8. It was found (data not shown) that the catalyst prepared without metal-nitrogen complexes showed no improvement in the activity in comparison to the metal-free carbon support. As indicated in Fig. 3-2-8, the surface nitrogen

concentration increased from 1.9 to 3.9 wt%, when the pyrolysis was performed in the presence of transition metals.

Yeager [29] and Wiesener [30] have suggested that the transition metals do not act as an active reaction site for oxygen reduction, but rather serve primarily to facilitate the stable incorporation of nitrogen into the graphitic carbon during high-temperature pyrolysis of metal-nitrogen complexes. This means that high-temperature pyrolysis in the presence of transition metals yields a carbonaceous layer with substantial nitrogen groups that are catalytically active for oxygen reduction. Our electrochemical and XPS results also indicate that the high-temperature pyrolysis combined with the chemical leaching facilitates the joint incorporation of pyridinic and graphitic nitrogen groups with a strong Lewis basicity, thus resulting in a high activity and selectivity of carbon composite catalyst.

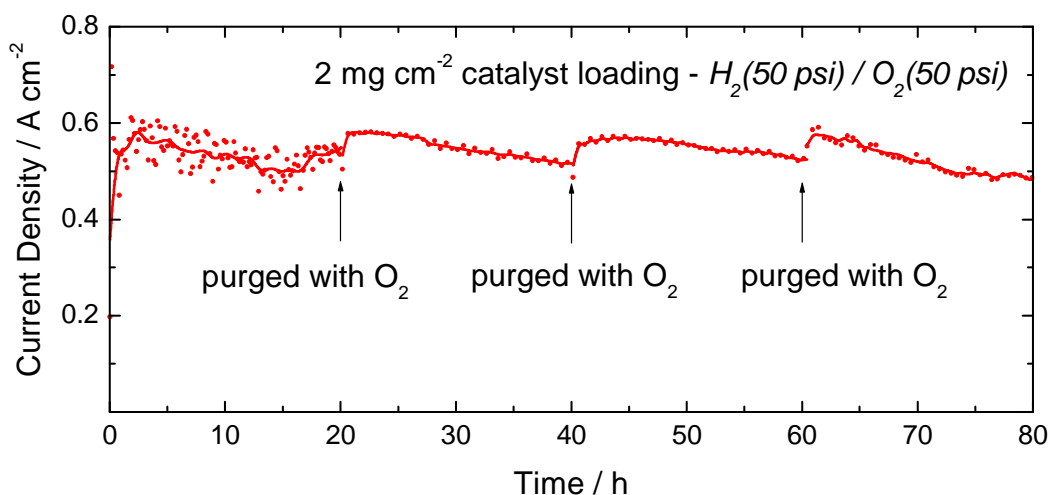


Figure 3-2-9. Typical stability test data for the carbon composite catalyst.

3.2.5. Durability Study of PEM Fuel Cell with Carbon Composite Cathode Catalyst

Figure 3-2-9 shows the current transient (stability test performance) measured on the carbon composite catalyst as a function of time. The cathode catalyst loading was 2 mg cm^{-2} , and the tests were run using H_2 (50 psi) and O_2 (50 psi). As indicated in the figure, the cathode compartment was periodically purged with O_2 gas during test, in order to remove liquid water accumulated inside the MEA. The result shows an initial increase of current density to ca. 0.6 A cm^{-2} , followed by a slight decay with time. The fuel cell performance was fully recovered upon O_2 purging, which indicates that an ineffective water management is responsible for a slight

performance loss of PEMFC, and no irreversible loss of catalytic activity occurs for 80 h operation.

Figure 3-2-10 demonstrates the potential transient measured on the carbon composite catalyst for stability test. The tests were run at 200 mA cm^{-2} using H_2 and O_2 without applying the back pressure. The cathode catalyst loading was 2.0 mg cm^{-2} . The test result showed an initial increase of potential to ca. 0.35 V , followed by a very slight decay with time (the decay rate $\approx 80 \mu\text{V h}^{-1}$). Note that only ca. 10 % performance decrease was observed for 480 h of continuous operation. Figure 3-2-11 compares the XPS spectra of N 1s region for the catalysts taken from the fresh MEA and the MEA tested for 480 h. Two dominant peaks are observed at 398.5 and 401.0 eV that can be assigned to pyridinic nitrogen and graphitic nitrogen, respectively, for both samples. This result confirms that catalytically active nitrogen functional groups remain stable on the carbon matrix during long-term fuel cell operation.

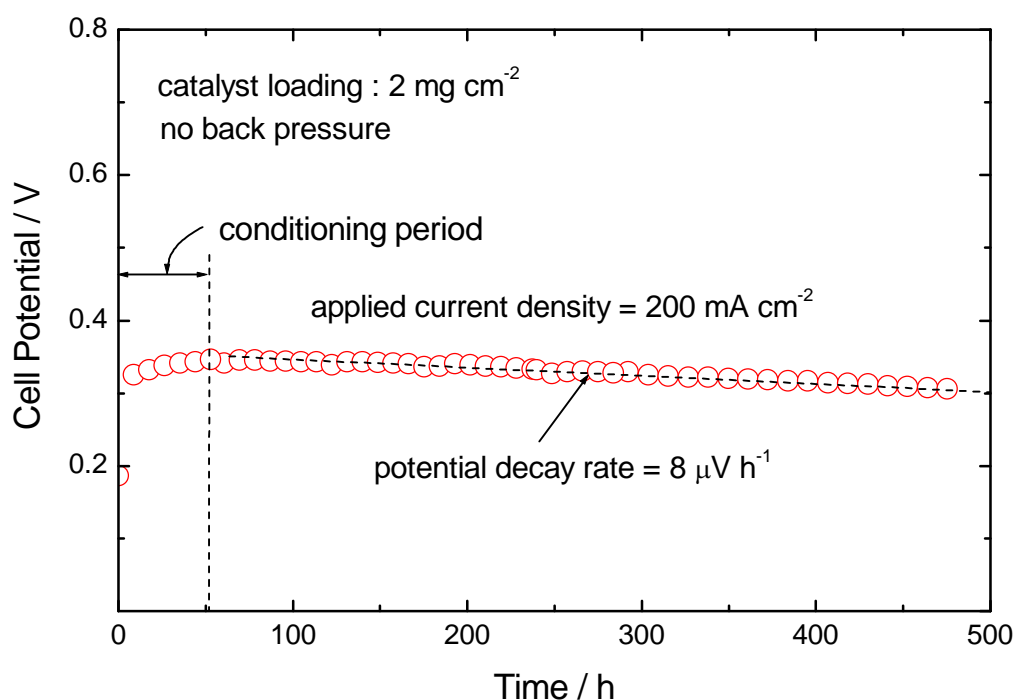


Figure 3-2-10. Galvanostatic potential transient measured on the carbon composite catalyst for stability test. The cathode catalyst loading was 2.0 mg cm^{-2} . The tests were run at 200 mA cm^{-2} using H_2 and O_2 without applying the back pressure.

Figure 3-2-12 presents a typical SEM image of the MEA prepared with the carbon composite cathode catalyst. The cathode catalyst loading was 6.0 mg cm^{-2} . The image shows the five

distinctive layers: (i) anode GDL, (ii) anode Pt/C catalyst layer, (iii) electrolyte membrane, (iv) cathode carbon composite catalyst layer, and (v) cathode GDL. The thickness of the cathode catalyst layer was ca. 35 μm which is thicker than the conventional Pt/C catalyst layer. We found (data not shown) that the fuel cell performance was fully recovered after purging the MEA with O_2 , which indicates that an ineffective water management due to a thicker cathode catalyst layer is mainly responsible for a slight performance loss observed in Fig. 3-2-10.

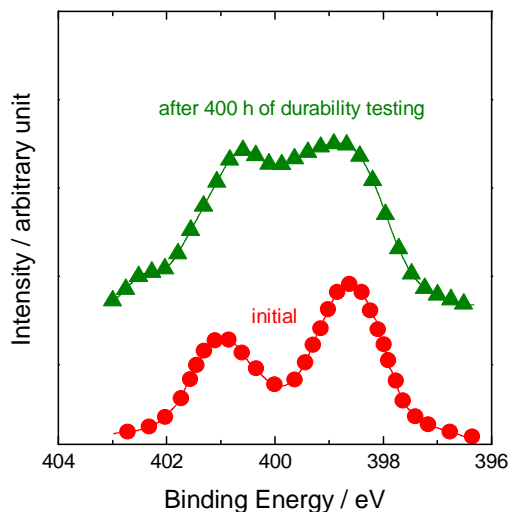


Figure 3-2-11. XPS spectra of N 1s region for the catalysts taken from the fresh MEA and the MEA tested for 480 h.

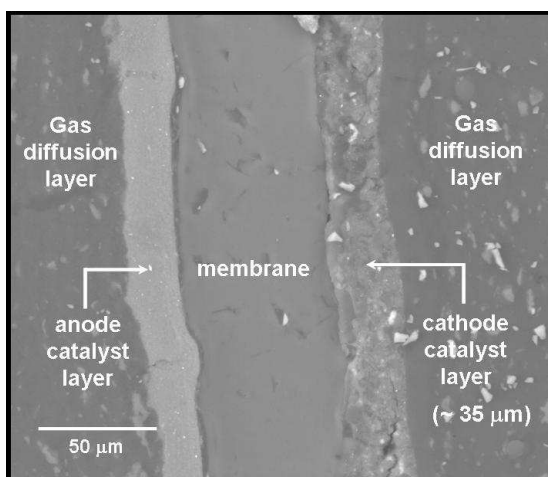


Figure 3-2-12. SEM image of the cross-section of the MEA prepared using the carbon composite cathode catalyst.

3.2.6. Summary

The new method was developed to synthesize highly active and stable carbon composite catalysts through the high-temperature pyrolysis of Co-Fe-N chelate complex on the support, followed by the chemical leaching. The carbon-based metal-free catalyst developed by us was used as the support. The carbon composite catalyst showed an onset potential for oxygen reduction as high as 0.87 V (NHE) in H₂SO₄ solution, and generated less than 1 % H₂O₂. The PEM fuel cell exhibited a current density as high as 2.3 A cm⁻² at 0.2 V for a catalyst loading of 6.0 mg cm⁻². No significant performance decrease was observed for 480 h of continuous fuel cell operation. The EXAFS study showed that the metal-nitrogen chelate decompose at high pyrolysis temperatures above 800 °C, resulting in the formation of the metallic species. All metal particles on the surface were removed by the chemical treatment in H₂SO₄ solution. The XPS results indicated that during the pyrolysis, the transition metals facilitate the joint incorporation of pyridinic and graphitic nitrogen groups into the carbon matrix, and the carbon surface with nitrogen groups is catalytically active for oxygen reduction.

3.3. CARBON COMPOSITE CATALYSTS SYNTHESIZED IN THE PRESENCE OF RUTHENIUM PRECURSOR (RuN_x/C)

3.3.1. Formation of Active Reaction Sites on RuN_x/C Catalysts

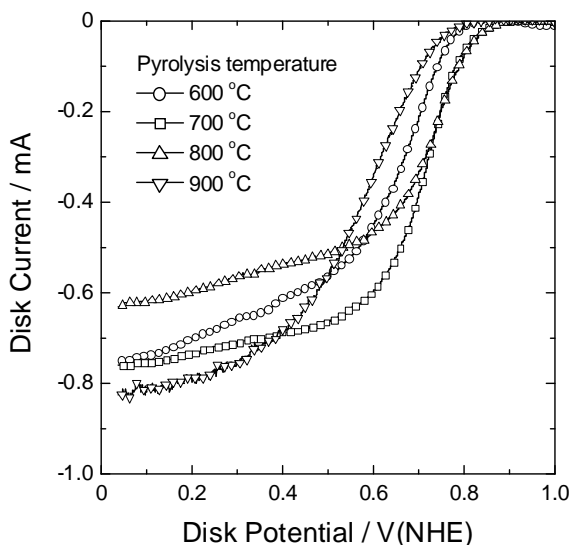


Figure 3-3-1. Polarization curves on the rotating disk electrodes for the RuN_x/C catalysts pyrolyzed at 600 to 900 °C. The measurements were performed in 0.5 M H_2SO_4 solution saturated with oxygen at the potential scan rate of 5 mV s^{-1} and the rotation speed of 900 rpm.

Figure 3-3-1 shows polarization curves on the rotating disk electrodes for the carbon-supported RuN_x catalysts pyrolyzed at various temperatures. The temperatures were varied between 600 and 900 °C. The measurements were performed in 0.5 M H_2SO_4 solution saturated with oxygen by using a potential scan rate of 5 mV s^{-1} and rotation speed of 900 rpm. In this work, the as-refluxed catalyst was found to hardly catalyze oxygen reduction, indicating no formation of the active reaction sites. The RRDE data in Fig. 3-3-1 show that the as-pyrolyzed catalysts exhibit the onset potentials for oxygen reduction as high as 0.85 V (NHE) and the well-defined limiting currents below 0.6 V (NHE). The pyrolysis at 700 °C leads to the best performance of the catalyst in terms of the activation overpotential and the reaction kinetics for oxygen reduction.

Table 3-3-1 summarizes the compositions of the as-refluxed and as-pyrolyzed RuN_x/C catalysts determined by XPS. For the as-refluxed catalyst, the Ru concentration evaluated by XPS is much lower than the concentration (20 wt%) in the precursor solution. Keeping in mind that the escape depth of photoelectrons is only a few nanometers, the result suggests that the Ru

clusters formed on the carbon support during refluxing may be mostly covered with a graphitic layer. The XPS data also indicate that the high-temperature pyrolysis induces a significant loss of Ru and N, while the O concentration remains almost constant.

Table 3-3-1. Surface compositions of the as-refluxed and as-pyrolized RuN_x/C catalysts determined by XPS.

Element	Concentration (wt%)	
	As-refluxed (before heat-treatment)	As-pyrolized (after heat-treatment)
Ru	4.4	1.8
C	70.3	89.9
N	18.1	1.8
O	7.2	7.5

Figure 3-3-2a and b present the XPS spectra of N 1s region for the as-refluxed and as-pyrolized RuN_x/C catalysts, respectively. The XPS spectrum of the as-refluxed catalyst exhibits a broad peak around 399.8 eV which corresponds to the nitrogen of the ternary amine-type [55]. Upon pyrolysis the peak splits into two broad peaks at about 398.4 and 400.4 eV which can be assigned to two different types of nitrogen on the carbon matrix, namely: the “pyridinic N” and the “pyrrolic N”, respectively. It is known that the “pyridinic N” possesses one lone pair of electrons in addition to the one electron donated to the conjugated π bond system, so it provides an orbital in the plane of the graphene layer that is capable for coordinating the metal ions [56]. From the results of RRDE and XPS measurements, it is clear that the high-temperature pyrolysis leads to the formation of Ru clusters coordinated with pyridinic N, and such Ru-N chelate sites are catalytically active for oxygen reduction.

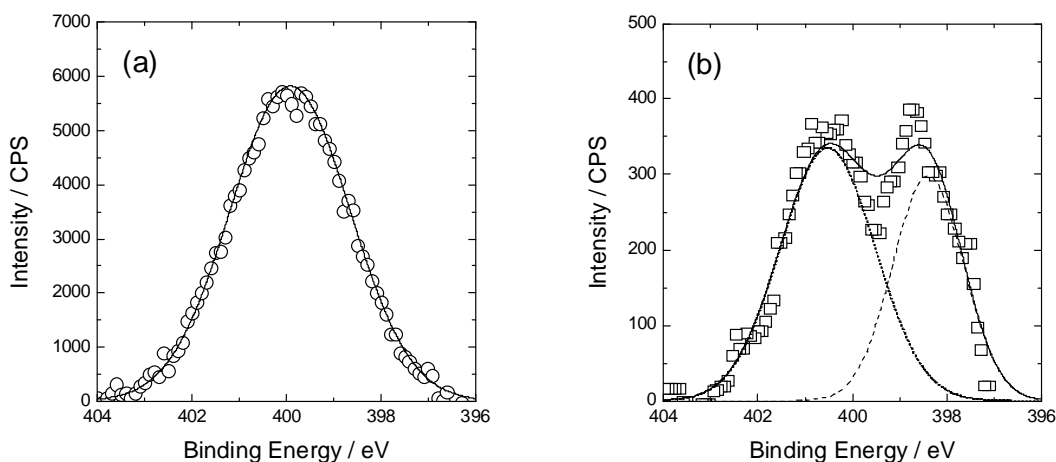


Figure 3-3-2. XPS spectra of N 1s region for the RuN_x/C catalysts: (a) as-refluxed and (b) as-pyrolized.

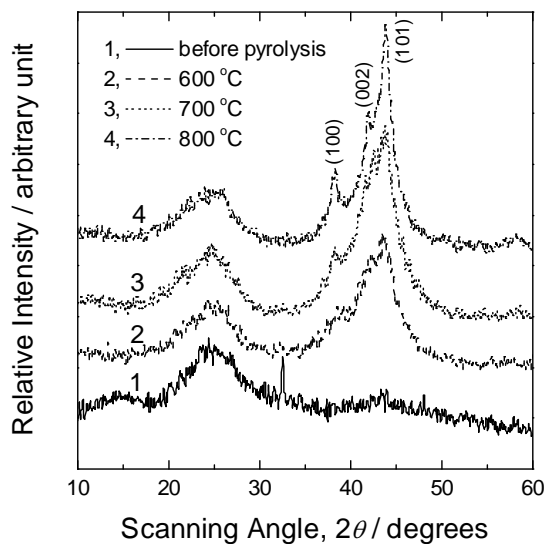


Figure 3-3-3. XRD patterns of the RuN_x/C catalysts subjected to pyrolysis at 600 to 800 oC. For comparison, the XRD pattern for the as-refluxed catalyst is given in the figure.

Figure 3-3-3 presents the powder XRD patterns of the carbon-supported RuN_x catalysts which were subjected to pyrolysis at various temperatures. For comparison, the XRD pattern for the as-refluxed catalyst is also shown in Fig. 3-3-3, and only a broad diffraction peak resulting from carbon support is observed around 24.5° . The absence of the diffraction peaks from Ru indicates that Ru crystal particles are too small to be detected by the instrument. However, all of

the XRD patterns for the as-pyrolized catalysts clearly exhibit the characteristic peaks which correspond to crystalline Ru. As indicated in Fig. 3-3-3, the diffraction peaks at 38.2, 42.0 and 43.8° are assigned to (100), (002) and (101) planes, respectively.

It is of importance to note that as the pyrolysis temperature increases from 600 to 800 °C, the diffraction peaks of Ru become sharper. That is, the Ru crystallite size gradually increases with increasing the pyrolysis temperature, which suggests that lower activity of the as-pyrolized catalyst at 800 °C results from the agglomeration of Ru crystallite particles. The results also indicated that the pyrolysis temperature plays a critical role in the formation of the active reaction sites. However, higher temperatures than 700°C cause Ru crystallite particles to agglomerate, resulting in a loss of the catalytic activity.

3.3.2. Effect of Nitrogen Contents on Catalytic Activity and Selectivity of RuN_x/C Catalysts

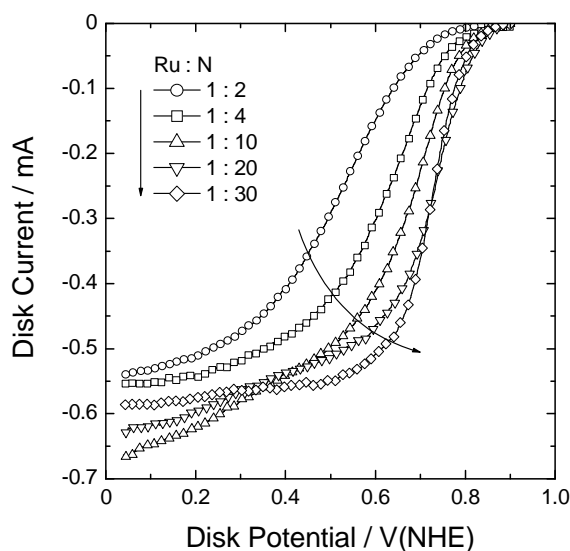


Figure 3-3-4. Polarization curves on the rotating disk electrodes for the RuN_x/C catalysts prepared using different molar ratios of Ru to N in the precursor solution.

Figure 3-3-4 shows typical polarization curves on the rotating disk electrodes for the carbon-supported RuN_x catalysts prepared using different molar ratios of Ru to N in the precursor solution. It is clearly seen that the nitrogen incorporation enhances the catalytic activity toward the oxygen reduction reaction. This fact further confirms that the N-coordinated Ru clusters are catalytically active for oxygen reduction. The catalyst prepared with the Ru:N ratio of 1:20 shows the lowest activation overpotential for oxygen reduction, while the best reduction kinetics

is observed on the catalyst with the 1:30 ratio.

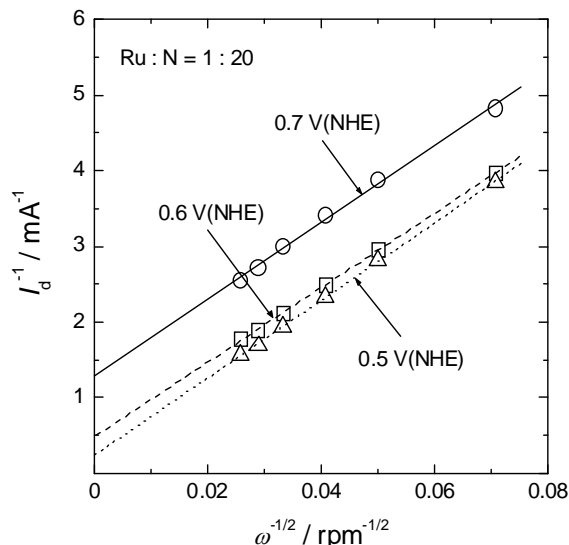


Figure 3-3-5. Koutecky-Levich plots at different potentials measured on the RuN_x/C catalysts prepared with the Ru:N ratio of 1:20.

Table 3-3-2. Kinetically limited currents, I_k , at 0.7 V (NHE) determined for the RuN_x/C catalysts prepared using different molar ratios of Ru to N in the precursor solution.

Ru : N	I_k at 0.7 V(NHE) (mA)
1 : 2	0.051
1 : 4	0.165
1 : 10	0.331
1 : 20	0.751
1 : 30	0.864

The Koutecky–Levich plots obtained at the potential range between 0.5 and 0.7 V (NHE) are presented in Figure 3-3-5 for the catalyst with the Ru:N ratio of 1:20. A linear relationship between I_d^{-1} and $\omega^{-1/2}$ is clearly observed and the slope remains nearly constant, regardless of the potential, which indicates that the electrochemical reaction follows first-order kinetics [57]. The

values of I_k at 0.7 V (NHE) for different Ru:N ratios are listed in Table 3-3-2. The I_k value increases with increasing the nitrogen content, which confirms that nitrogen incorporation improves the catalytic activity of RuN_x/C .

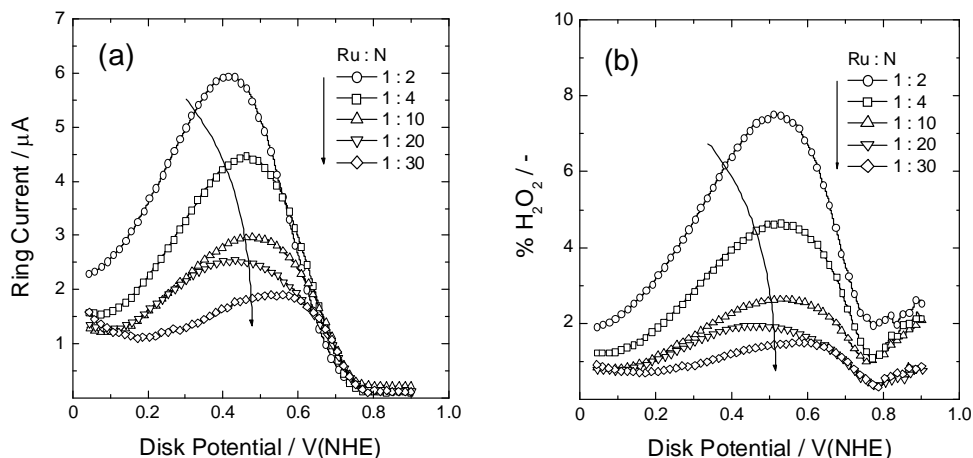


Figure 3-3-6. (a) Ring currents and (b) H_2O_2 percentages determined as a function of the disk potential for the RuN_x/C catalysts with different molar Ru:N ratios.

Figure 3-3-6a presents the ring currents measured for the carbon-supported RuN_x catalysts with different molar Ru:N ratios as a function of the disk potential. The ring current increases with decreasing the disk potential, then reaches a maximum value between 0.6 and 0.4 V(NHE), and finally decreases with further decreasing the disk potential. The value of ring current decreases with increasing the N content over the whole potential range, which indicates that the nitrogen incorporation improves the selectivity of the catalyst to four electron reduction of O_2 to H_2O .

The percentage of H_2O_2 generated on the cathode decreases with increasing the N content. The RuN_x/C catalysts with the Ru to N ratios of 1:20 and 1:30 generate less than 2 % H_2O_2 , over the whole potential range, which is much lower than that value reported in the literature [58].

3.3.3. Surface-Modification of RuN_x/C

Organic additive, which contains N and O, was incorporated into the precursor solution during refluxing, in an attempt to increase the catalytic activity and selectivity. Figure 3-3-7a and b demonstrate polarization curves on the rotating disk electrodes and the percentage of H_2O_2 , respectively, measured for the RuN_x/C catalyst prepared using urea ($(\text{NH}_2)_2\text{CO}$).

It is found that urea has a positive effect on the activation overpotential and the reduction

kinetics. The urea-modified RuN_x/C catalyst exhibits an onset potential as high as 0.9 V(NHE). Urea chemically modifies the RuN_x catalyst surfaces by providing functional groups of nitrogen and oxygen which contribute to the formation of active reaction sites. Also as presented in Fig. 3-3-7b, urea decreases the amount of H_2O_2 generated on the cathode.

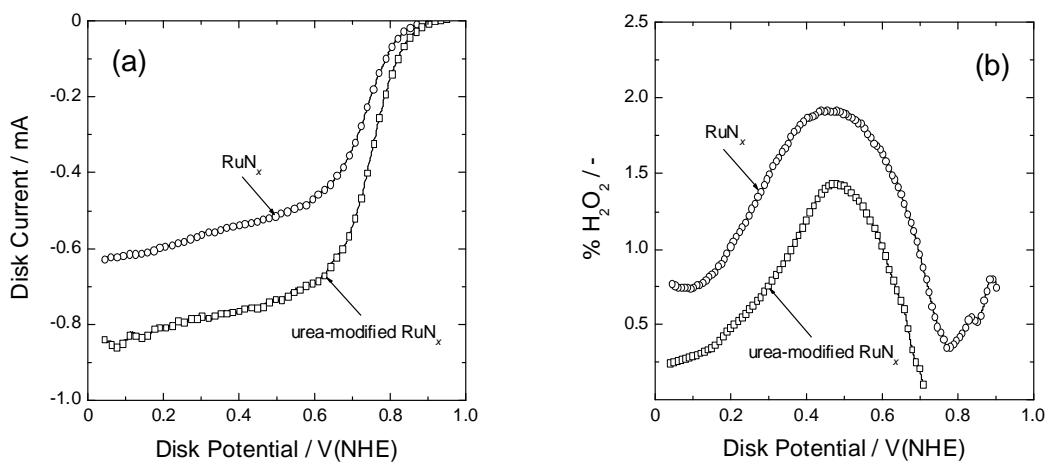


Figure 3-3-7. (a) Polarization curves on the rotating disk electrodes and (b) H_2O_2 percentages measured for the RuN_x/C catalysts prepared using urea as additive

3.3.4. Comparative Study of Ru-Based Catalysts Synthesized with Different Methodologies

Different types of Ru-based catalysts were synthesized and compared with the RuN_x/C catalyst: (i) RuO_x/C , (ii) amorphous $\text{Mo}_x\text{Ru}_y\text{Se}_z/\text{C}$ and (iii) $\text{Ru-NH}_3/\text{C}$. The RuO_x/C catalyst was synthesized by a colloidal method developed in our laboratory [59]. The Ru complex colloidal solution was prepared with a slow addition of NaHCO_3 into an aqueous $\text{RuCl}_3 \cdot x\text{H}_2\text{O}$ solution, and then the colloidal particles were adsorbed onto the carbon black under stirring conditions.

The amorphous $\text{Mo}_x\text{Ru}_y\text{Se}_z/\text{C}$ catalyst was synthesized by reacting metal carbonyls with Se in xylene at 140 °C under stirring and refluxing conditions for 20 h, as described by Solorza-Feria and coworkers [60]. Finally, the $\text{Ru-NH}_3/\text{C}$ catalyst was synthesized by heat-treating Ru^{3+} -impregnated carbon under an NH_3 atmosphere at 800 °C for 1 h. Here an NH_3 gas was used as the N-precursor instead of propylene diammine.

Figure 3-3-8a and b summarizes the polarization curves obtained on the rotating disk electrodes and the percentage of H_2O_2 , respectively, measured for various Ru-based catalysts. The RRDE data obtained from the commercially available 20 wt% Pt/C catalyst are also given in

Fig. 3-3-8 for comparison. The urea-modified RuN_x/C catalyst shows higher catalytic activity toward the oxygen reduction reaction. As shown in Fig. 3-3-8a, the activation overvoltage decreases more than 150 mV when compared with all other Ru-based catalysts under study. It produces smaller amount of H_2O_2 during oxygen reduction, indicating the enhanced catalytic selectivity toward four-electron reduction. The results indicated that RuN_x/C catalyst modified with urea in this work exhibits comparable catalytic activity and selectivity to the commercial Pt/C catalyst in the RRDE tests. From the TEM analysis, the particle sizes of the RuN_x catalysts were estimated to be ca. 2 – 4 nm, regardless of the presence and absence of urea, which are about two times smaller than the particle sizes of $\text{Mo}_x\text{Ru}_y\text{Se}_z/\text{C}$ and $\text{Ru-NH}_3/\text{C}$ (ca. 4 – 8 nm).

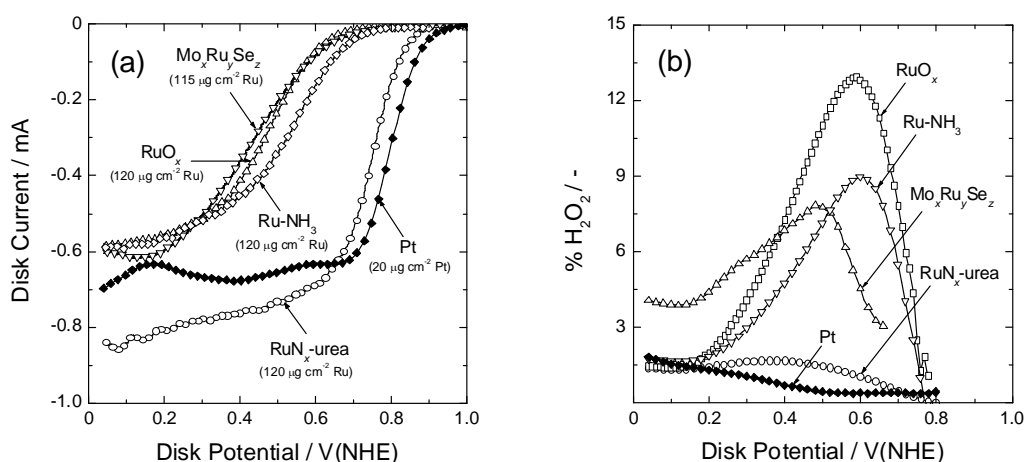


Figure 3-3-8. (a) Polarization curves on the rotating disk electrodes and (b) H_2O_2 percentages measured for various Ru-based catalysts: urea-modified RuN_x/C , RuO_x/C , amorphous $\text{Mo}_x\text{Ru}_y\text{Se}_z/\text{C}$ and $\text{Ru-NH}_3/\text{C}$. The RRDE data obtained from the commercial Pt/C is also presented in the figure.

3.3.5. Summary

Nano-sized Ru-N chelate catalysts were synthesized by using RuCl_3 and propylene diammine, followed by heat-treatment at 600 to 900 °C. The influence of pyrolysis temperature, nitrogen content and surface-modifier on the catalytic properties has been investigated. XPS and XRD studies showed that the high-temperature pyrolysis plays a critical role in the formation of the active Ru-N sites, but it causes the agglomeration of Ru crystalline particles above 800 °C. The RRDE experiments indicated that the nitrogen incorporation improves the catalytic activity and selectivity toward four electron reduction of molecular oxygen to water. The urea-modified RuN_x/C catalyst with the particle sizes of 2 – 4 nm exhibited comparable catalytic activity to the carbon-supported Pt catalyst, and generated less than 2 % H_2O_2 during oxygen reduction.

4. CONCLUSIONS

A novel nitrogen-modified carbon-based catalyst for oxygen reduction is achieved by introducing oxygen and nitrogen groups from various nitrogen precursors. The nature of nitrogen surface groups and the effect of pyrolysis temperature on the activity of the catalyst have been evaluated. XPS indicated that high concentration of pyridinic type nitrogen groups doped on graphitic carbon increase the activity of catalysts. The carbon-based catalysts showed an onset potential at around 0.78 V (NHE) and the amount of H₂O₂ generated during oxygen reduction was approximately 1-3 % at 0.5 V (NHE).

A highly active and stable carbon composite catalyst was developed through the high-temperature pyrolysis of the precursor of nitrogen supported on the metal free catalysts in the presence of iron and cobalt precursors, followed by the chemical leaching. The carbon composite catalyst showed an onset potential for oxygen reduction as high as 0.87 V (NHE) in H₂SO₄ solution, and generated less than 1 % H₂O₂. The PEM fuel cell exhibited a current density as high as 2.3 A cm⁻² at 0.2 V for a catalyst loading of 6.0 mg cm⁻². No significant performance decrease was observed for 480 h of continuous fuel cell operation. The EXAFS study showed that the metal-nitrogen chelate decompose at high pyrolysis temperatures above 800 °C, resulting in the formation of the metallic species. All metal particles on the surface were removed by the chemical treatment in H₂SO₄ solution. The XPS results indicated that during the pyrolysis, the transition metals facilitate the joint incorporation of pyridinic and graphitic nitrogen groups into the carbon matrix, and the carbon surface with nitrogen groups is catalytically active for oxygen reduction.

For comparison, nano-sized Ru-N chelate catalysts were synthesized by using RuCl₃ and propylene diammine, followed by heat-treatment at 600 to 900 °C. The influence of pyrolysis temperature, nitrogen content and surface-modifier on the catalytic properties has been investigated. XPS and XRD studies showed that the high-temperature pyrolysis plays a critical role in the formation of the active Ru-N sites, but it causes the agglomeration of Ru crystalline particles above 800 °C. The RRDE experiments indicated that the nitrogen incorporation improves the catalytic activity and selectivity toward four electron reduction of molecular oxygen to water. The urea-modified RuN_x/C catalyst with the particle sizes of 2 – 4 nm exhibited comparable catalytic activity to the carbon-supported Pt catalyst, and generated less than 2 % H₂O₂ during oxygen reduction.

5. REFERENCES

- [1]. M.L. Rao, B.A. Damjanovic, J. O'M Bockris, *J. Chem. Phys.* 67 (1963) 2508.
- [2]. R.R. Adzic, in: J. Lipkowski, P. Ross (Eds.), *Electrocatalysis*, VCH Publishers, New York, 1998, pp. 197–242.
- [3]. N.M. Markovic, P.N. Ross, *Electrochim. Acta* 45 (2000) 4101.
- [4]. N.M. Markovic, P.N. Ross, *Surf. Sci. Rep.* 286 (2002) 1.
- [5]. H.A. Gasteiger, S.S. Kocha, B. Sompalli, F.T. Wagner, *Appl. Catal. B* 56 (2005) 9.
- [6]. R. Jasinski, *Nature* 201 (1964) 1212.
- [7]. A. Widelov, R. Larsson, *Electrochim. Acta* 37 (1992) 187.
- [8]. G. Lalander, R. Cote, D. Guay, J.P. Dodelet, L.T. Weng, P. Bertrand, *Electrochim. Acta* 42 (1997) 1379.
- [9]. R. Cote, G. Lalande, D. Guay, J.P. Dodelet, *J. Electrochem. Soc.* 145 (1998) 2411.
- [10]. P. Guerec, M. Savy, J. Riga, *Electrochim. Acta* 43 (1998) 743.
- [11]. P. Guerec, M. Savy, *Electrochim. Acta* 44 (1999) 2653.
- [12]. S.Lj. Gojkovic, S. Gupta, R.F. Savinell, *Electrochim. Acta* 45 (1999) 889.
- [13]. S.Lj. Gojkovic, S. Gupta, R.F. Savinell, *J. Electroanal. Chem.* 462 (1999) 63.
- [14]. M. Lefevre, J.P. Dodelet, P. Bertrand, *J. Phys. Chem. B* 104 (2000) 11238.
- [15]. H. Schulenburg, S. Stankov, V. Schunemann, J. Radnik, I. Dorbandt, S. Fiechter, P. Bogdanoff, H. Tributsch, *J. Phys. Chem. B* 107 (2003) 9034.
- [16]. S. Marcotte, D. Villers, N. Guillet, L. Roue, J.P. Dodelet, *Electrochim. Acta* 50 (2004) 179.

- [17]. K. Sawai, N. Suzuki, J. Electrochem. Soc. 151 (2004) A682/
- [18]. D. Villers, X. Jacques-Bedard, J.P. Dodelet, J. Electrochem. Soc. 151 (2004) A1507.
- [19]. K. Sawai, N. Suzuki, J. Electrochem. Soc. 151 (2004) A2132.
- [20]. S.-I. Yamazaki, Y. Yamada, T. Ioroi, N. Fujiwara, Z. Siroma, K. Yasuda, Y. Miyazaki, J. Electroanal. Chem. 576 (2005) 253.
- [21]. M. Yuasa, A. Yamaguchi, H. Itsuki, K. Tanaka, M. Yamamoto, K. Oyaizu, Chem. Mater. 17 (2005) 4278.
- [22]. F. Jaouen, F. Charreteur, J.P. Dodelet, J. Electrochem. Soc. 153 (2006) A689.
- [23]. R. Bashyam, P. Zelenay, Nature 443 (2006) 63.
- [24]. R. Yang, A. Bonakdarpour, E.B. Easton, J.R. Dahn, ECS Trans. 3 (2006) 221.
- [25]. E.B. Easton, A. Bonakdarpour, R. Yang, D.A. Stevens, D.G. O'Neill, G. Vernstrom, D.P. O'Brien, A.K. Schmoeckel, T.E. Wood, R.T. Atanasoski, J.R. Dahn, ECS Trans. 3 (2006) 241.
- [26]. J.-H. Kim, A. Ishihara, S. Mitsushima, N. Kamiya, K.-I. Ota, ECS Trans. 3 (2006) 255.
- [27]. T. Otsubo, S. Takase, Y. Shimizu, ECS Trans. 3 (2006) 263.
- [28]. F. Beck, J. Appl. Electrochem. 7 (1977) 239.
- [29]. E. Yeager, Electrochim. Acta 29 (1984) 1527.
- [30]. K. Wiesener, Electrochim. Acta 31 (1986) 1073.
- [31]. R.A. Sidik, A.B. Anderson, N.P. Subramanian, S.P. Kumaraguru, B.N. Popov, J. Phys. Chem. B 110 (2005) 1787.
- [32]. N.P. Subramanian, S.P. Kumaraguru, H.R. Colon-Mercado, H. Kim, B.N. Popov, T.

- Black, D.A. Chen, J. Power Sources 157 (2006) 56.
- [33]. Y.-P. Lin, H.-P. Lin, D.-W. Chen, H.-Y. Liu, H. Teng, C.-Y. Tang, Mater. Chem. Phys. 90 (2005) 339.
- [34]. H.-Y. Liu, K.-P. Wang, H. Teng, Carbon 43 (2005) 559.
- [35]. P. Kim, H. Kim, J.B. Joo, W. Kim, I.K. Song, J. Yi, J. Power Sources 145 (2005) 139.
- [36]. P. Kim, J.B. Joo, W. Kim, S.K. Kang, I.K. Song, J. Yi, Carbon 44 (2006) 381.
- [37]. J.B. Joo, P. Kim, W. Kim, J. Kim, J. Yi, Catal. Today 111 (2006) 171.
- [38]. V. Raghuvver, A. Manthiram, Electrochem. Solid-State Lett. 7 (2004) A336.
- [39]. P.H. Matter, U.S. Ozkan, Catal. Lett. 109 (2006) 115.
- [40]. P.H. Matter, L. Zhang, U.S. Ozkan, J. Catal. 239 (2006) 83.
- [41]. P.H. Matter, E. Wang, J.-M.M. Millet, U.S. Ozkan, J. Phys. Chem. C 111 (2007) 1444.
- [42]. Pizzi, Wood Adhesives: Chemistry and Technology, A. Pizzi, Ed.; Marcel Dekker, New York, 1983.
- [43]. K. Kinoshita, J.A.S. Bett, Carbon 11 (1973) 403.
- [44]. H.P. Boehm, Carbon 32 (1994) 759.
- [45]. J.P. Chen, S. Wu, Langmuir 20 (2004) 2233.
- [46]. K. Stanczyk, R. Dziembaj, Z. Piwowarska, S. Witkowski, Carbon 33 (1995) 1383.
- [47]. R.J.J. Jansen, H. van Bekkum, Carbon 33 (1995) 1021.
- [48]. J. Casanovas, J.M. Ricart, J. Rubio, F. Illas, J.M. Jimenez-Mateos, J. Am. Chem. Soc., 118 (1996) 8071.
- [49]. V. S. Bagotzky, M. Tarasevich, K. Radysishkina, O. Levina, S. Andriyova, J. Power Sources 2 (1977) 233.

- [50]. K. Wiesener, A. Fuhrmann, Z. Phys. Chem. 261 (1980) 411.
- [51]. A. Karsheva, S. Gamburtzev, I. Iliev, Elektrokimiya 18 (1982) 127.
- [52]. V.V. Strelko, N.T. Kartel, I.N. Dukhno, V.S. Kuts, R.B. Clarkson and B.M. Odintsov, Surf. Sci. 548 (2004) 281.
- [53]. S. Maldonado and K.J. Stevenson, J. Phys. Chem. B 109 (2005) 4707.
- [54]. V.V. Strelko, N.T. Kartel, I.N. Dukhno, V.S. Kuts, R.B. Clarkson and B.M. Odintsov, Surf. Sci. 548 (2004) 281.
- [55]. L. J. Gerenser, J. M. Grace, G. Apai and P. M. Thompson, Surf. Interface Anal. 29 (2000) 12.
- [56]. Y. F. Jia, B. Xiao and K. M. Thomas, Langmuir 18 (2002) 470.
- [57]. O. Solorza-Feria, S. Ramírez-Raya, R. Rivera-Noriega, E. Ordoñez-Regil and S. M. Fernández-Valverde, Thin Solid Films 311 (1997) 164.
- [58]. H. Schulenburg, M. Hilgendorff, I. Dorbandt, J. Radnik, P. Bogdanoff, S. Fiechter, M. Bron and H. Tributsch, J. Power Sources 155 (2006) 47.
- [59]. H. Kim and B. N. Popov, J. Power Sources 104 (2002) 52.
- [60]. O. Solorza-Feria, K. Ellmer, M. Giersig and N. Alonso-Vante, Electrochim. Acta 39 (1994) 1647.

6. PRODUCTS DEVELOPED UNDER THE AWARD

a1. SPECIAL RECOGNITIONS & AWARDS

Crystal Flame Innovation Award in Research from FuelCell South was presented to Dr. Popov's research group for research work in the fields of the non-precious metal catalyst development, the preparation of thin film assemblies with nano-structured catalysts, and the development of the pulse deposition technique for preparation of membrane electrode assemblies.

a2. PUBLICATIONS

1. H. Kim and B.N. Popov, "Development of Novel Method for Preparation of PEM Fuel Cell Electrodes", *Electrochemical and Solid State Letters*, 7 (2004) A71.
2. H. Kim, N. Subramanian and B.N. Popov, "Preparation of PEM Fuel Cell Electrodes Using Pulse Electrodeposition", *J. of Power Sources*, 138 (2004) 14.
3. H. R. Colón-Mercado, H. Kim, B. N. Popov, "Durability study of Pt₃Ni₁ catalysts as cathode in PEM fuel cells", *Electrochem. Commun.* 6 (2004) 795.
4. B.N. Popov, "Electrodeposition of Alloys and Composites with Superior Corrosion and Electrocatalytic Properties", AESF Scientific Achievement Award Plenary Lecture Paper, *Plating & Surface Finishing*. p. 40- 48, October 2004.
5. H. R. Colón-Mercado, B. N. Popov, "Stability of platinum based Alloy cathode catalysts in PEM fuel cells," *J. Power Sources* 155 (2006) 253.
6. N.P. Subramanian, S.P. Kumaraguru, H.R. Colón-Mercado, B.N. Popov, "Studies on Co based electrocatalysts on modified carbon substrates for PEMFC applications," *J. Power Sources* 157 (2006) 56.
7. L. Liu, J.-W. Lee, B. N. Popov, "Development of ruthenium-based bimetallic electrocatalysts for oxygen reduction reaction," *J. Power Sources* 162 (2006) 1099.
8. R. Sidik, A. Anderson, "Co₉S₈ as a catalyst for electroreduction of O₂: quantum chemistry predictions", *J. Phys. Chem. B* 110 (2006) 936.
9. R. Sidik, A. Anderson, N. P. Subramanian, S. P. Kumaraguru, B. N. Popov, "O₂ reduction on graphite and nitrogen-doped graphite: experiment and theory", *J. Phys. Chem. B* 110 (2006) 1787.
10. S. Park, J. W. Lee, B. N. Popov, "Effect of carbon loading in microporous layer on PEM fuel cell performance", *J. Power Sources* 163 (2006) 357.

11. S. P. Kumaraguru, N. P. Subramanian, H. Colon and B. N. Popov, "Non-noble metal catalysts for oxygen reduction reaction in acidic media," *ECS Trans. 1* (2006) 27.
12. H.R. Colon-Mercado, H. Kim and B.N. Popov, "Durability study of Pt₃Ni₁ catalysts as cathode in PEM fuel cells", *Electrochemistry Communications*, 6 (2004) 795.
13. L. Liu, B.N. Popov, "Highly Active Ruthenium Based Catalysts for Oxygen Reduction Reaction", *ECS Trans.*, 1 (2006) 41.
14. L. Liu, H. Kim, J.-W. Lee and B.N. Popov, "Development of Ruthenium-Based Catalysts for Oxygen Reduction Reaction", *J. Electrochem. Soc.*, 154 (2007) A123-A128.
15. X. Li, H. R. Colón-Mercado, G. Wu, J.-W. Lee, B. N. Popov, "Development of method for synthesis of PtCo cathode catalysts for PEM fuel cells", *Electrochem. Solid-State Lett.* 10 (2007) B201.
16. X. Li, H. Colon, G. Wu, J. W. Lee, B. N. Popov, "Development of stable Pt-Co cathode catalysts for PEM fuel cells" *ECS Transactions* 11 (2007) 1259.
17. J. W. Lee, B. N. Popov, "Ruthenium-based electrocatalysts for oxygen reduction reaction-a review", *J Solid State Electrochem.* 11 (2007) 1355.
18. E. Vayner, R. A. Sidik, A. B. Anderson, B. N. Popov, "Experimental and theoretical study of cobalt selenide as a catalyst for O₂ electroreduction", *J. Phys. Chem. C* 111 (2007) 10508.
19. V. Nallathambi, G. Wu, N. P. Subramanian, S. P. Kumaraguru, J. W. Lee, B. N. Popov, "Highly active carbon composite electrocatalysts for PEM fuel cells", *ECS Transactions* 11 (2007) 241.
20. S. Ayyadurai, Y.-S. Choi, P. Ganesan, S.P. Kumaraguru, B.N. Popov, "Novel PEM Fuel Cell Cathodes Prepared by Pulse Deposition," *J. Electrochem. Soc.*, 154 (2007) B1063-B1073.
21. V. S. Park, J.-W. Lee and B.N. Popov, "Effect of PTFE Content in Microporous Layer on Water Management," *ECS Trans.*, 11 (2007) 623-628.

22. S. Park and B.N. Popov, "Effect of hydrophobicity and pore geometry in cathode GDL on PEM fuel cell Performance", *Electrochim. Acta* (accepted).
23. V. Nallathambi, J. W. Lee, S. P. Kumaraguru, G. Wu, B. N. Popov, "Development of high performance carbon composite catalyst for oxygen reduction reaction in proton exchange membrane fuel cells", *J. Power Sources* 183 (2008) 34.
24. X. Li, L. Liu, J.W. Lee, B. N. Popov, Development of tellurium-modified carbon catalysts for oxygen reduction reaction in PEM fuel cells. *J Power Sources* 182 (2008) 18.
25. S. Park and B.N. Popov, "Effect of hydrophobic and structural properties of GDL on PEM fuel cell performance", *ECS transactions* 16 (2008) 1627.
26. H.-Y. Jung, S. Park, P. Ganesan, and B. N. Popov, "Electrochemical studies of unsupported PtIr electrocatalyst as bifunctional oxygen electrode in unitized regenerative fuel Cell (URFC)", *ECS transactions* 16 (2008) 1117.
27. N. P. Subramanian, X. Li, V. Nallathambi, S. P. Kumaraguru, H. Colon-Mercado, G. Wu, J.-W. Lee, B. N. Popov, "Nitrogen-modified carbon-based catalysts for oxygen reduction reaction in PEM fuel cells", *J. Power Sources* 188 (2009) 38.
28. S. Park and B. N. Popov, "Effect of GDL characteristics on mass transport in PEM fuel cells", *Fuel* (under review).
29. G. Liu, X. Li, and B. N. Popov, "Development of N-doped mesoporous carbon based non-precious oxygen reduction catalysts for PEM fuel cells" (in preparation).
30. G. Liu, X. Li, S. Park, and B. N. Popov, "Non-precious oxygen reduction catalysts based on simple heat treatment of high N-content carbon with iron acetate" (in preparation).

a3. PRESENTATIONS

1. S. P. Kumaraguru, N. Subramanian, H. R. Colón-Mercado, H. Kim, B. N. Popov, “Novel Non Precious Metal Catalysts for PEMFC Applications”, *206th meeting of the Electrochemical Society*, Honolulu, HI, October 2004.
2. N. P. Subramanian, S. P. Kumaraguru, B. N. Popov, “Analysis of Carbon Substrates used in Non-Precious Metal Catalysts for Fuel Cell Applications”, *206th meeting of the Electrochemical Society*, Honolulu, HI, October 2004.
3. S. P. Kumaraguru, B. N. Popov, “New Electrocatalysts for PEM Fuel Cells”, *SERMACS*, Durham, NC, November 2004. (Invited).
4. B. N. Popov, “Overview of Fuel Cell Research at CEE”, *Fuel Cell South Annual Conference*, Columbia, SC, May 2005. (Invited).
5. L. Liu, B. N. Popov, “Highly Active Ru-Chelate Catalysts for Oxygen Reduction Reaction”, *the 1st Symposium on Manufacturing of MEAs for Hydrogen Applications*, Dayton, OH, August 2005.
6. “Novel Non-Precious Metals for PEMFC,” *2nd MEA Manufacturing Symposium*, Dayton, OH, August 2006.
7. S. P. Kumaraguru, M. Curran, B. N. Popov, “Non Noble Metal Catalysts for Oxygen Reduction Reaction”, *208th meeting of the Electrochemical Society*, Los Angeles, CA, October 2005.
8. L. Liu, B. N. Popov, “Novel Ru Chelate Catalysts for Oxygen Reduction Reaction”, *208th meeting of the Electrochemical Society*, Los Angeles, CA, October 2005.
9. “Development of Nano-structured Electrocatalysts for PEM Fuel Cells”, *5th International Conference of the Chemical Societies of the South-East European Countries*, Ohrid, Macedonia, September 2006. (Invited).

10. "Highly Active Carbon-Based Catalysts for PEM Fuel Cells", *210th Meeting of the Electrochem Soc.*, Cancun, Mexico, October 2006.
11. "Highly Active Carbon-Based Catalysts for PEM Fuel Cells", *2006 Annual AIChE Meeting*, San Francisco, CA, November 2006.
12. X. Li, V. Nallathambi, H. R. Colon-Mercado, J.-W. Lee, B. N. Popov, "Development of Stable Pt-Co Cathode Catalysts for PEM Fuel Cells," *212th Meeting of the Electrochem. Soc.*, Washington DC, October 2007.
13. V. Nallathambi, G. Wu, N.P. Subramanian, S. P. Kumaraguru, J.-W. Lee, B. N. Popov, "Highly Active Carbon-Based Electrocatalysts for PEM Fuel Cells," *212th Meeting of the Electrochem. Soc.*, Washington DC, October 2007.
14. B. N. Popov, "Development of Advanced Catalysts and Supports for PEM Fuel Cell", Yonsei University, Seoul, South Korea, Jun 2008.
15. B. N. Popov, "Development of Metal Free Catalyst", Samsung, South Korea, June 2008.
16. B. N. Popov, "Catalyst Development Research at University of South Carolina", Kyongju, South Korea, June 2008.
17. B. N. Popov, "Development of Advanced Catalysts and Supports for PEM Fuel Cell Application", *214th Meeting of the Electrochem. Soc.*, Honolulu, HI, October 2008.
18. S. Park and B.N. Popov, "Effect of Hydrophobic and Structural Properties of GDL on PEM Fuel Cell Performance", *214th Meeting of the Electrochem. Soc.*, Honolulu, HI, October 2008.

b. WEB SITE THAT REFLECT THE RESULTS OF THIS PROJECT

Research group

<http://www.che.sc.edu/faculty/popov/drbnp/WebSite/index.html>

Center for Electrochemical Engineering

<http://www.che.sc.edu/centers/CEE/>

c. COLLABORATIONS FOSTERED

- Case Western Reserve University, US
- North Eastern University, US
- Yonsei University, South Korea

d. INVENTIONS/PATENT APPLICATIONS

1. B. N. Popov, J.-W. Lee, N. P. Subramanian, S. P. Kumaraguru, H. R. Colón-Mercado, V. Nallathambi, X. Li, G. Wu, “Carbon-based composite electrocatalysts for low temperature fuel cells”, US Patent 11/939,322 (2007) pending.
2. B. N. Popov, H. Kim, “Development of a novel method for preparation of PEMFC electrodes”, US Patent Publication No. 2006040157 (2006) pending.
3. “Pulse Electrodeposition of Platinum for PEMFC Electrodes Using Wetting Agents”, US Patent, Provisional Patent, Invention Disclosure USCRF No. 602.

7. MATHEMATICAL MODELING

ABSTRACT

Cobalt sulfides have been known for more than 30 years to be active toward oxygen reduction and cobalt selenides have shown less activity. In this paper a theoretical analysis is made of the four-electron reduction reaction of oxygen to water over the mixed anion and cation (202) surface of pentlandite structure Co_9Se_8 , one of several selenide phases. Reversible potentials for forming adsorbed reaction intermediates in acid are predicted using adsorption energies calculated with the Vienna *ab initio* simulation program (VASP) and the known bulk solution values together in a linear Gibbs energy relationship. Comparison with an earlier theoretical analysis of pentlandite structure Co_9S_8 shows the overpotential is predicted to be larger for the selenide by around 0.46 V. Cobalt selenide electrodes of unspecified stoichiometry were prepared chemically on glassy carbon discs and polarization curves were measured using rotating discs. When heat treated at 900 °C the onset potential for O_2 reduction was found to be 0.5 V (NHE) whereas electrodes not subject to heat treatment were inactive. For Co_3S_4 , onset potentials in the literature are ~0.8 V (NHE), consistent with a ~0.3 V higher measured overpotential for the selenide. The theoretical predictions for the pentlandite sulfide and selenide surfaces are in qualitative agreement.

The effect of hydrophobic and structural properties of a single/dual-layer cathode gas diffusion layer on mass transport in PEM fuel cells was studied using an analytical expression. The simulations indicated that liquid water transport at the cathode is controlled by the fraction of hydrophilic surface and the average pore diameter in the cathode gas diffusion layer. Deposition of a hydrophobic microporous layer reduces the average pore diameter in the macroporous substrate. It also increases the hydrophobic surface, which improves the mass transport of the reactant. The optimized hydrophobicity and pore geometry in a dual-layer cathode GDL leads to an effective water management, and enhances the oxygen diffusion kinetics.

7.1. EXPERIMENTAL AND THEORETICAL STUDY OF COBALT SELENIDE AS A CATALYST FOR O₂ ELECTROREDUCTION

7.1.1. Introduction

Cobalt sulfides were noted over thirty years ago to be active toward the four-electron electroreduction of O₂ to H₂O in acid electrolyte [1,2]. Cobalt selenides were observed to be less active and the cobalt tellurides were less active still. A recent theoretical study [3] explored the activities of three crystallographic surface planes of pentlandite structure Co₉S₈ toward this reaction and produced a mechanism consistent with the activity. The Co terminated (008) surface was predicted to be inactive due to passivation by OH(ads), as were the isolated Co sites on the 1:4 Co:S (002) surface. However, the partially OH(ads)-passivated 5:4 Co:S (202) surface presented properties allowing each of the four one-electron reduction steps to proceed at acceptable reversible potentials, accounting for good observed activity. In the predicted mechanism for this surface, O₂ dissociated exothermally over a 4-fold Co site, placing one O(ads) near its center and the other on an adjacent S. These O(ads) were subsequently reduced to OH(ads) and H₂O and the last OH(ads) reduction step was predicted to have the lowest reversible potential, 0.74 V, indicating it may be responsible for the O₂ reduction overpotential (the standard reversible potential for the reduction to water is 1.23 V).

It is of interest to explain the lower activity of the cobalt selenides. This is addressed by using the same theoretical approach as for the pentlandite sulfide to study the steps in O₂ reduction over an isostructural (202) surface to see if, according to the predicted reversible potential of the electron transfer steps, it should indeed be less active than the sulfide. This study also presents new experimental results for cobalt selenide.

Developing new electrocatalysts to replace platinum for O₂ reduction remains a significant technological goal. In addition to the cobalt chalcogenides mentioned above, many other transition metal compounds have been explored [4-15]. Alonso-Vante *et al.* have led the study of transition-metal chalcogenides as oxygen reduction catalysts. They advanced the synthesis of Ru-based catalysts and contributed to the characterization of them using electrochemical and spectroscopic techniques. They associated the four-electron reduction of molecular oxygen to water with O₂ adsorption on adjacent cation sites, which, they believe, are required for O-O bond cleavage [15].

Pentlandite structure Co₉S₈ and (Fe,Ni)₉S₈ have also been the subject of fairly recent electronic structure, lattice parameter and stability calculations [16]. Lately, cobalt sulfide compounds, such as linnaeite (Co₃S₄) and pentlandite (Co₉S₈), have been characterized as

potential materials for the synthesis of nanocrystals [17,18]. The activities of nanocrystals of these compounds as oxygen reduction electrocatalysts have not been studied.

The surface structures and compositions of the chalcogenide electrocatalysts are not yet experimentally characterized. This is why idealized model structures are assumed for theoretical studies. In the case of well-studied platinum and platinum alloy oxygen reduction electrocatalysts, surface structures are believed to be known, and theoretical studies have been carried out for some of them. Platinum monolayer skins on platinum alloys are more active for O₂ reduction, and a series of theoretical studies has been conducted to determine properties of Pt₃Co [18,19] and Pt₃Cr [20-22] (111) surface Pt skins. The ~50 mV reduction in overpotential on the skins relative to pure platinum has been explained as due to a positive shift in the OH(ads) reduction potential [18,21,22] and a positive shift in the OOH(ads) formation potential during the first electron transfer step [20]. The VASP slab-band density functional theory was used [23-26]. The same approach was used in a study of pentlandite structure Co₉S₈ as a catalyst for electroreduction of molecular oxygen³ and will be used in the present study of the cobalt selenide (202) surface.

7.1.2. Experimental Studies

Se powder (99.999%) was dissolved in anhydrous xylene at 140 °C under stirring conditions. The xylene solvent was deaerated by bubbling Ar through it. Dicobalt octacarbonyl (Co₂(CO)₈), was added to the Se-dissolved xylene solution, and then the reaction mixture was refluxed in an Ar atmosphere at 140 °C for 30 h. The resulting powder specimens were filtered and washed with diethylether, then dried in air. The Co-Se catalysts were further heat-treated in an NH₃ atmosphere at 900 °C for 90 min. The bulk and surface structures of the catalyst particles were not determined.

The rotating disk electrode (RDE) measurements were performed in a three-electrode electrochemical cell using a bi-potentiostat (Pine Instruments) at room temperature. A glassy carbon disk (5.0 mm diameter) was employed as the working electrode, and it was polished with Al₂O₃ powder. The catalyst ink was prepared by blending the Co-Se catalyst powder with isopropyl alcohol in an ultrasonic bath. The catalyst ink was deposited on the glassy carbon disk until a total catalyst loading of 610 g cm⁻² was achieved. After drying, 10 μL of a mixture of Nafion solution (5 wt%, Aldrich) and isopropyl alcohol was coated onto the catalyst layer to ensure better adhesion of the catalyst on the glassy carbon substrate. Aqueous 0.5 M H₂SO₄ was used for the electrolyte. Platinum mesh and Hg/HgSO₄ electrodes were used as the counter and reference electrodes. All potentials in this work were referred to the normal hydrogen electrode

(NHE) scale. In order to estimate the double-layer capacitance, the electrolyte was deaerated by bubbling N_2 through it, and a cyclic voltammogram was recorded by scanning the disk potential between 0.04 and 1.04 V(NHE) at a 5 mV s^{-1} rate. Then, the electrocatalytic activity for oxygen reduction was evaluated in the oxygen-saturated electrolyte. The oxygen reduction currents were taken as the differences between currents measured for the deaerated and oxygen-saturated electrolytes.

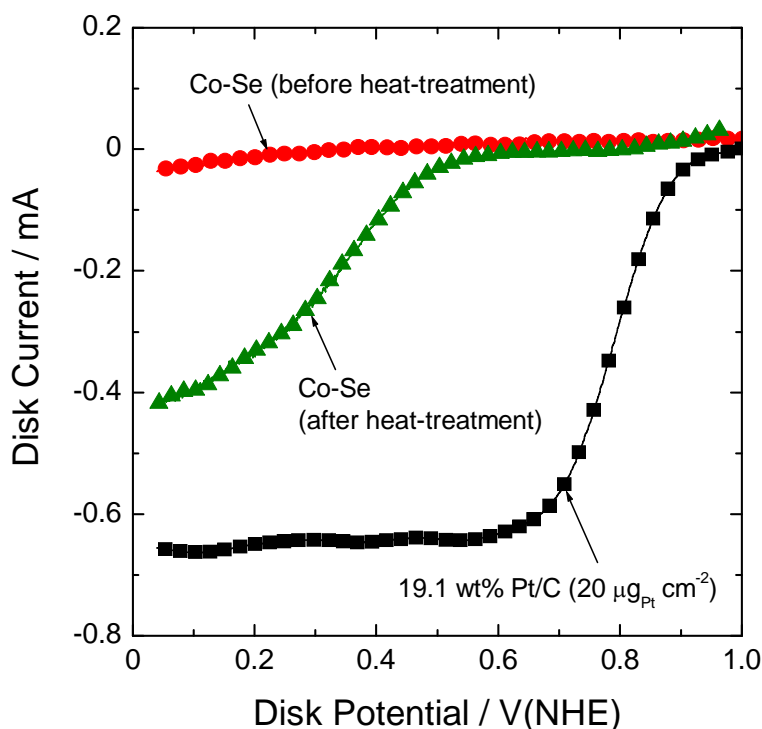


Fig. 7-1-1. Effect of heat-treatment on oxygen reduction for unsupported cobalt selenide. Pt/C results are included for comparison. The RDE measurements were performed in 0.5 M H_2SO_4 solution saturated with oxygen by using a potential scan rate of 5 mV s^{-1} and rotation speed of 900 rpm.

Fig. 7-1-1 shows typical polarization curves on the rotating disk electrodes for the as-refluxed and as-heat-treated Co-Se catalysts. The RDE measurements were performed in 0.5 M H_2SO_4 solution saturated with oxygen; the rotation speed was 900 rpm. The as-refluxed Co-Se catalyst, which was not subjected to heat-treatment, does not show any activity towards the oxygen reduction reaction. A remarkable increase in catalytic activity is evident for the catalyst that was heat-treated at $900 \text{ }^\circ\text{C}$. The as-heat-treated Co-Se catalyst exhibits an onset potential for oxygen reduction as high as 0.5 V (NHE). The XRD pattern for commercially available CoSe sample (purity > 99%, Alfa Aesar) showed characteristic diffraction peaks of hexagonal structure at $2\theta = 33.3^\circ$, 44.3° , and 50.1° . The XRD pattern of as-prepared Co-Se catalyst (before heat-

treatment) exhibited very broad diffraction lines at the same values of 2θ (except for $2\theta \approx 33.3^\circ$), indicating that an amorphous phase coexists with crystalline phases which have very small sizes. Upon heat-treatment at 900°C , the diffraction peaks became sharper. The peak intensity increased significantly, which indicates a crystallization of the catalyst particles and a crystal growth

The XRD patterns determined for commercial CoSe sample and those of Co-Se catalyst synthesized in this study showed a mismatch at approximately 33.3° . The peak shift observed for the Co-Se catalyst prepared in this work toward a higher 2θ value indicates a non-stoichiometric nature of the nano-particles (i.e. Co_{1-x}Se), as inferred from the phase diagram of the Co-Se system. The preliminary surface characterization studies using XRD, Energy Dispersive Spectroscopy and Transmission Electron Microscopy indicated that the catalyst may consist of nano-crystals of Co_{1-x}Se surrounded by extra Se elements. Since physisorbed or elemental selenium would evaporate from the catalyst at the heat-treatment temperature used in this study, some of Se elements must have been strongly (chemically) bonded to the Co particles. The observed enhanced activity of the as-heat-treated catalyst over the as-prepared catalyst is attributed to a higher degree of crystallization of the non-stoichiometric Co_{1-x}Se particles due to the heat-treatment process.

7.1.3. Theoretical Approach

All calculations were performed using the Vienna *ab initio* simulation program (VASP) [24-28] with a plane-wave basis and non-local Vanderbilt-type ultrasoft pseudo-potentials (US-PP) to describe the electron-ion interaction [28]. Exchange and correlation energies were expressed by the functional proposed by Perdew and Wang [29]. Self-consistent solutions of Kohn-Sham equations corresponding to the electronic ground states were solved via an iterative unconstrained band-by-band matrix-diagonalization scheme based on a residual minimization method [27,30]. Brillouin zone integrations were executed with Monkhorst-Pack grids [31] and a generalized Gaussian smearing [32] of $\sigma = 0.2\text{ eV}$ for integration in reciprocal space. A plane-wave energy cutoff of 400 eV and a $5 \times 5 \times 1$ k -point mesh was used because those parameters proved to be satisfactory for similar calculations [3,19-23]. Optimization of the lattice constant for Co_9Se_8 yielded the value $a = 10.374\text{ \AA}$, only slightly underestimating the experimental value $a = 10.431\text{ \AA}$ [33]. As in pentlandite structure Co_9S_8 , the (202) surface, defined in the cubic unit cell in Fig. 7-1-2, represented by a slab composed of four layers of continuing cations and anions separated by 10 \AA of vacuum. Since the purely Co terminated (008) surface of the sulfide was found in [3] to be poisoned by adsorbed OH and the isolated Co sites of the (002) surface of the

sulfide, surrounded by S, were also poisoned by OH, these two surfaces were not examined in this study of the selenide.

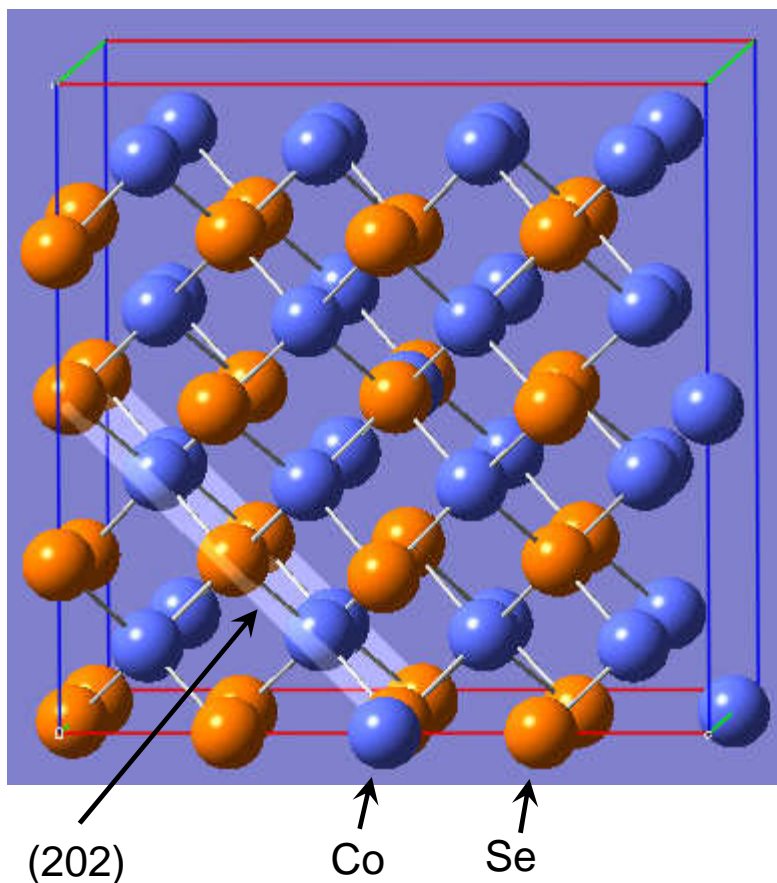


Fig. 7-1-2. Co_9Se_8 unit cell in pentlandite structure ($4\text{Co}_9\text{Se}_8$, 68 atoms; Cobalt atoms are blue). The (202) surface is shown as the highlighted crystal plane. Optimized cell lattice constant $a = 10.374 \text{ \AA}$ (experimental $a = 10.431 \text{ \AA}$) [33].

For the (202) slab unit cell, shown in Fig. 7-1-3, atom positions of two topmost layers and the adsorbates were relaxed and the two bottom layers were frozen at the optimized unit cell geometry, just as was done for the sulfide in [3].

Adsorption bond strength, or bond dissociation energy, D_e is the negative of difference between the energy of the slab unit cell plus adsorbate system and the sum of the energy of the separated slab unit cell and adsorbate:

$$D_e = - [E(\text{adsorbate on slab unit cell}) - E(\text{slab unit cell}) - E(\text{adsorbate})] \quad (7-1-1)$$

This dissociation energy does not include zero-point vibrational energies, but they would approximately cancel out in reversible potential determinations because bond orders are roughly

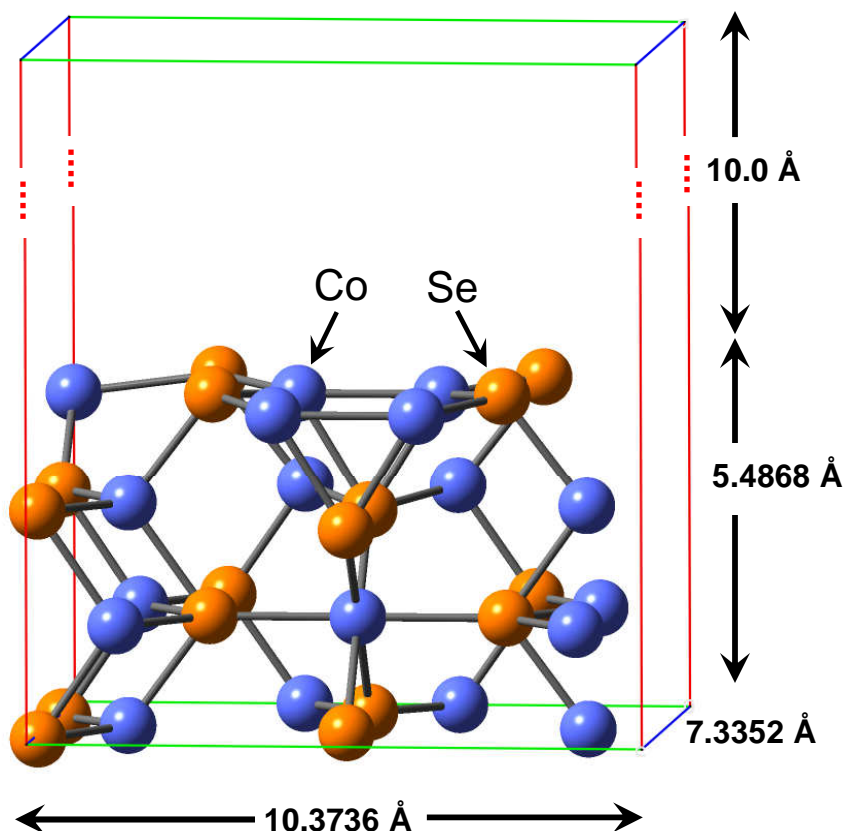


Fig. 7-1-3. Slab (202) surface model used in the adsorption calculations showing the top two layers relaxed.

conserved. Reversible potentials were predicted using the calculated adsorption bond strengths in a linear Gibbs free energy relation. It was shown in past studies that reversible potentials for reaction steps taking place on the catalyst surface, $U^{\text{rev}}(\text{surface})$, can be determined to reasonable accuracy by introducing the catalyst as a perturbation to the solution phase reaction [23-24]:

$$\Delta G^{\text{rev}}(\text{surface}) = \Delta G^{\circ} - \Delta E(\text{adsorption}) \quad (7-1-2)$$

$$U^{\text{rev}}(\text{surface}) = U^{\circ} + \Delta E(\text{adsorption})/nF \quad (7-1-3)$$

where ΔG° is the standard Gibbs energy change for a reduction reaction, $\Delta E(\text{adsorption})$ is defined to be the total adsorption bond strength of the products minus the total adsorption bond strength of the reactants, n is the number of electrons transferred, F is the Faraday constant, and U° is the standard electrode potential. Based on comparisons of predictions using this model with experimental measurements, predictions using the model have been found to have up to ~0.2 V uncertainty.

For a sample prediction with the above linear Gibbs energy relationship, consider OH(ads) reduction to H₂O(ads) on a platinum surface. Using experimentally estimated bond strengths of 2.50 eV [35] and 0.42 eV [36] respectively, and 2.81 V as the reversible potential for OH reduction to water [37], the reversible potential predicted for the surface is $U_{\text{surface}} = (2.81 + 0.42 - 2.50) \text{ V} = 0.73 \text{ V}$. This result is close to the ~0.6 V onset potential observed for platinum electrode in 0.1 N acid [38-43]. Only one other standard reversible potential is needed in this paper, 2.047 V for O(aq) reduction to OH(aq) [37].

7.1.4. Theoretical Results

H₂O and O₂ Adsorption

It has been proposed that OH(ads) blocks surface sites on platinum electrodes, and, by preventing O₂ adsorption at high potentials, it contributes to the O₂ reduction overpotential [19-23,38-43]. However, recent theoretical work for platinum electrodes suggests the potential for reducing O₂(ads) to OOH(ads) may be close to the OH(ads) reduction potential [21], and therefore the OOH(ads) formation step may play a role in determining the cathode overpotential. Furthermore, measured effective activation energies for the four-electron process on platinum at several electrode potentials are matched well by theoretical prediction for the activation energies for O₂(ads) reduction to OOH(ads) [44]. These findings suggest that both OH(ads) reduction and O₂(ads) reduction to OOH(ads) may contribute to the overpotential.

In the case of the (202) surface of Co₉S₈, it was predicted that a partial coverage of OH on the Co sites with very low reversible potential could form, but further increase in OH(ads) required high potential. Thus, the partially-covered Co site presented opportunities for O₂ adsorption and reduction.

Our results for OH(ads) formation on the (202) surface of Co₉Se₈ are in Fig. 7-1-4. The predicted potential for the first water oxidation is -0.67 V, which is very similar to -0.69 V predicted for the (202) Co₉S₈ surface [3]. The second water molecule is oxidized at -0.29 V, which is close to $U^{\circ} = -0.42 \text{ V}$ predicted in [3] for sulfide (but mistakenly reported as 0.64 V). The selenide value is lower because of weaker H₂O adsorption compared to the sulfide. Potentials for oxidizing the third water molecule are both high, due predominantly to weakened OH adsorption; 1.19 V for the selenide and 1.64 V [3] for the sulfide.

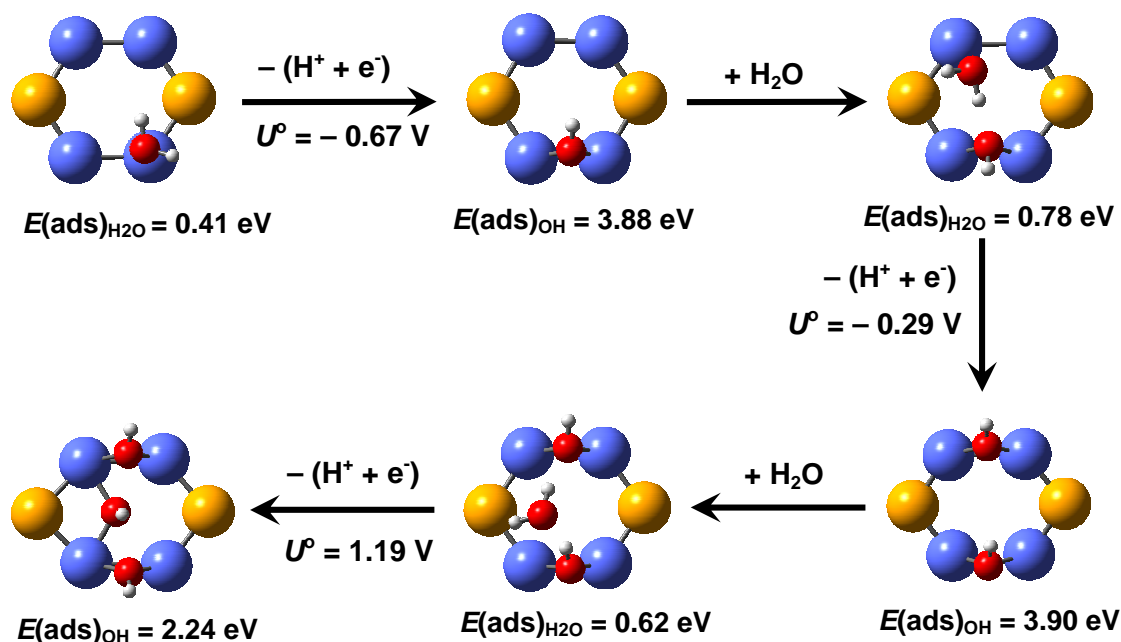


Fig. 7-1-4. Predicted H₂O oxidation reactions over a four-atom Co site forming the 2-fold hydroxylated (202) surface.

O₂ Reduction

From the preceding it is evident that, as for the sulfide, over the electrode potential range of interest for oxygen reduction, the (202) surface site should have 2 OH adsorbed bridging Co atoms, as in Fig. 7-1-5. On this site a -1.38 eV dissociative adsorption energy was calculated for O₂, which is close to the -1.13 eV value calculated in [3] for the sulfide. Fig. 7-1-5 shows the surface structure before and after O₂ adsorption. The calculations yielded no activation energy barrier to the dissociation of O₂ during adsorption to form 2O(ads). Heat loss in this step indicates wasted free energy and necessitates that there will be one or more overpotentials in the electron transfer steps. An ideal catalyst will have O₂ adsorption and H₂O desorption free energies equal to zero because this would avoid wasting reaction free energy [45,46]. The ideal catalyst will also have reversible potentials for each electron transfer step equal to the reversible potential for the overall multielectron reaction.

Each electron transfer step will have a unique reversible potential and there will be activation energy for the reduction reaction at that potential. As the electrode potential is increased, the activation energy for reduction will increase [47], and the assumption is that the increase is rapid enough to cause the reaction forming the adsorbed reaction intermediate rate to slow

substantially as the potential is increased through the underpotential region. Based on this assumption, it is possible to propose that the rate limiting step is probably the step with the highest overpotential relative to the reversible potential of the overall multi-electron reaction. This is the basis of the discussion that follows.

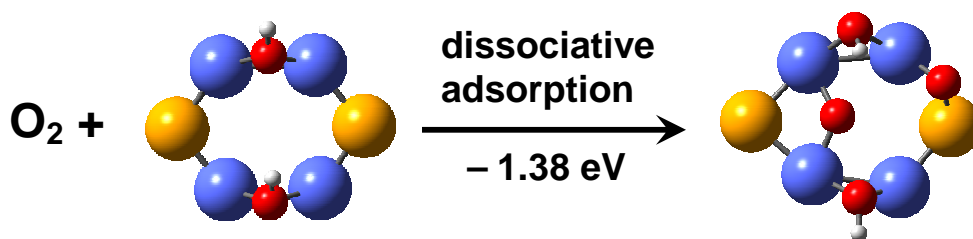


Fig. 7-1-5. O₂ dissociation on the (202) Co₉Se₈ hydroxylated surface model.

Possible reduction pathways for the adsorbed O atoms were explored next by the reaction



First, the O bridging two Co atoms in S1, Fig. 7-1-6 was reduced, and the newly-formed OH(ads) was put on the upper-left Co, in structure S2. The calculated reversible potential for reducing this O(ads) is -0.03 V, which is less than the 0.83 V value for the sulfide in the same structure. Since S2 might be a metastable local minimum on the energy surface, variations on this were optimized with OH(ads) bonded to the lower-left Co, S3, and the lower right Co, S4, and the reversible potentials increased slightly to 0.13 V and 0.23 V respectively. Finally, OH(ads) was bonded to Se, S5 was found to have the highest reversible potential of formation, 0.61 V, and so this reduction step is predicted to go at the highest potential. This contrasts with the sulfide case, for which the potential was 0.20 V for this structure and S2 had the highest reversible potential. 0.83 V.

The next step was to decide which way the O₂ reduction would go from the last structure, S5 in Fig. 7-1-6. Fig. 7-1-7 shows two possible pathways to reduce the O(ads) bonded to Co and the OH(ads) bonded to Se: the O is reduced first in path I to yield S6, and the OH(ads) is reduced first in path II to yield S7. The respective reversible potentials are 1.10 V and 1.47 V, meaning both reactions can go at the 0.61 V maximum potential of the first reduction step. The predicted reversible potential for reducing the OH(ads) formed in S6 to H₂O(ads) in S8 is 0.58 V and for reducing O(ads) in S7 to OH(ads) in S8 the value is 0.22 V. The last step, reducing the upper left-hand OH(ads) in S8 to H₂O(ads) in S9 has a predicted reversible potential 1.07 V.

When the two adsorbed water molecules are removed in the fourth electron transfer step the predicted reversible potential is reduced to 0.37 V.

7.1.5. Conclusions

The first electron transfer step with the highest predicted reversible potential following the dissociative adsorption of O₂ reduces O bonded to Se to OH bonded to Se at 0.61 V. The second electron transfer can either form OH(ads) from the O(ads) (path I) or reduce the OH to H₂O (path II). From the reversible potentials, 1.10 V and 1.47 V respectively, both are possible at the lower 0.61 V reversible potential of the first step. The third electron transfer step leads to OH(ads) + H₂O(ads) at predicted reversible potentials of 0.58 V for path I and 0.22 V for path II. The higher 0.58 V value is the limiting one and it is essentially the same as the 0.61 V value calculated for the first electron transfer step. However, to achieve the standard state of the surface as one with two OH(ads) bridging Co, one H₂O molecule must be desorbed with an energy of 0.08 eV and the second must be desorbed with an energy of 0.62 eV. These adsorbed water molecules can be viewed as surface poisons that slow the kinetics. Alternatively, the energy needed to cause them to become desorbed can be incorporated into the fourth electron transfer step. When this is done the calculated reversible potential for the last step becomes 0.37 V. This could be the limiting step for the cobalt selenide.

Looking back at the electron transfer steps on the selenide and sulfide, the lowest reversible potential for the selenide is for the last electron transfer when it leads to the initial state of the surface, 0.37 V. For the sulfide the value 0.74 V was reported for this step in ref 3, but in determining that number the product water molecules were assumed to not interact with the surface. However they are actually unstable the surface by 0.27 eV in the optimized structure and are in a metastable equilibrium. Taking this repulsion into account, the reversible potential for the last electron transfer on the sulfide would be 1.01 V. Using this new result, the first electron transfer has the lowest reversible potential on the sulfide, 0.83 V. Based on these results, the selenide is predicted to have overpotential 0.46 V greater than the sulfide.

The experimental onset of O₂ reduction on the treated cobalt selenide is about 0.5 V according to Fig. 7-1-1 and this is in reasonable agreement the 0.37 V reversible potential predicted for the last electron transfer step. It must be kept in mind that the bulk and surface structures of the selenide catalyst particles are unknown as are the surface structures of the sulfide catalysts, and our pentlandite (202) surface provides a model for active surface structures. For the pentlandite structure sulfide the onset potential is not known, but for the thiospinel, Co₃S₄, it is roughly 0.8 V [2]. This compares well with the predicted 0.83 V predicted reversible potential for the first reduction step. Other measures of the higher activity of the sulfide compared to the selenide are the current densities at 600 mV, 1300 mA/m² for 95 % CoS_{0.96}, 5 % Co₃S₄ compared to 76 mA/cm² for 83 % CoSe₂, 17% CoSe_{0.5} in Ref. 1 and, at 400 mV, 60 mA/cm² for Co₃S₄ compared to 0.1 mA/cm² for Co₃Se₄ in [2].

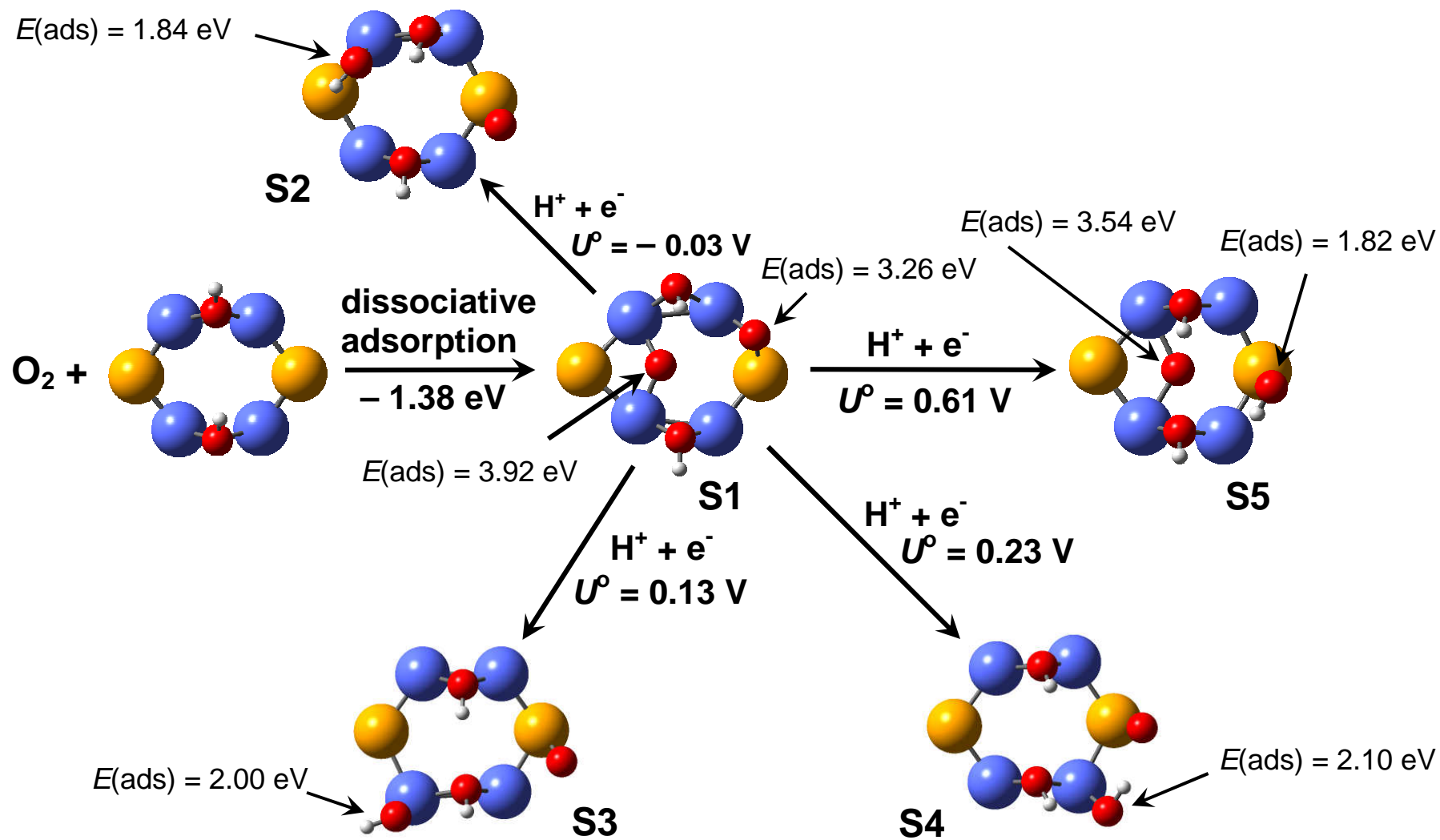


Fig. 7-1-6. First electron transfer step during O_2 reduction on (202) Co_9Se_8 : structure S4 has the highest.

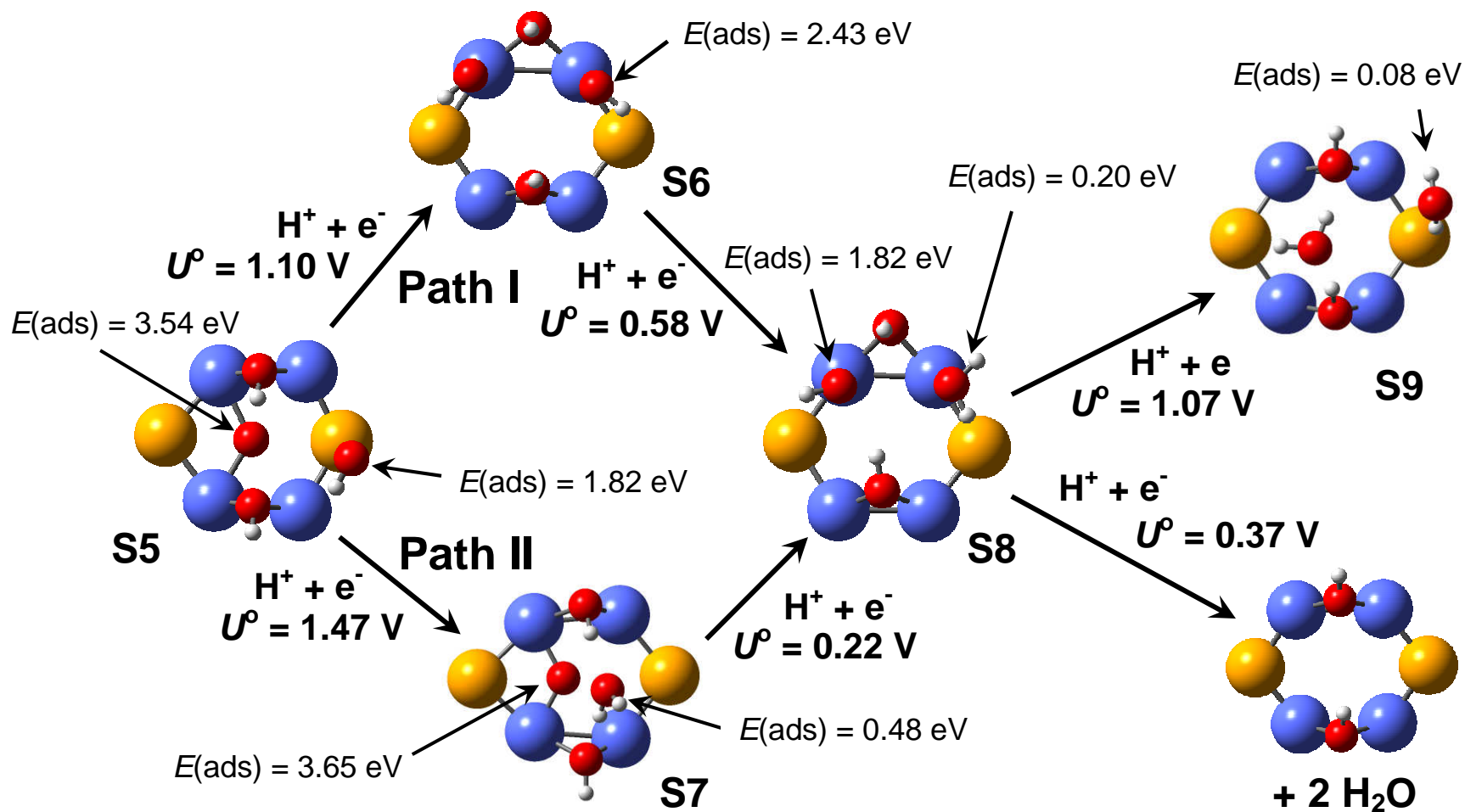


Fig. 7-1-7. Two predicted pathways for the second, third, and fourth electron transfer steps for O_2 reduction on (202) Co_9Se_8 . Path 1 has the favored higher potential. For the fourth electron transfer step 0.37 V is the reversible potential for producing the surface state chosen as the standard one for the beginning of the calculations.

It is difficult to establish the cause for the lower reversible potentials for the probable controlling electron transfer steps on the selenide. The lattice constant is smaller for the sulfide, 9.9482 Å compared to 10.431 Å for the selenide, and the different atom spacing may be affecting intra-adsorbate hydrogen bonding in a way that affects the adsorption energies of the intermediate species, a structure effect, and there may also be different degrees of coupling of the adsorbates electronically through the surface atoms.

7.1.6. References

- [1] V.D. Barsel, W. Sarholz, P. Schaarner, J. Schmitz, *Ber. Bunsen-Ges.* 78 (1974) 608.
- [2] H. Behret, H. Binder, G. Sandstede, *Electrochim. Acta* 20 (1975) 111.
- [3] R.A. Sidik, A.B. Anderson, *J. Phys. Chem. B* 110 (2006) 936.
- [4] N. Alonso-Vante, H. Tributsch, *Nature* 323 (1986) 431.
- [5] N. Alonso-Vante, W. Jaegermann, H. Tributsch, W. Hönlle, K. Yvon, *J. Am. Chem. Soc.* 109 (1987) 3251.
- [6] N. Alonso-Vante, B. Schubert, H. Tributsch, A. Perrin, *J. Catal.* 112 (1988) 384.
- [7] N. Alfonso-Vante, B.Schubert, H. Tributsch, *Materials Chemistry and Physics* 22 (1989) 281.
- [8] C. Fischer, N. Alonso-Vante, S. Fiechter, H. Tributsch, G. Reck, W. Schulz, *J. Alloys Compd.* 178 (1992) 305.
- [9] O. Solorza-Feria, K. Ellmer, M. Giersing, N. Alonso-Vante, *Electrochim. Acta*, 39 (1994) 1647.
- [10] N. Alonso-Vante, H. Tributsch, O. Solorza-Feria, *Electrochim. Acta* 40 (1995) 567.
- [11] J. Prakash, H. Joachin, *Electrochim. Acta* 45 (2000) 2289.
- [12] N. Alonso-Vante, P. Borthen, M. Fieber-Erdmann, H. -H. Strehblow, E. Holub-Krappe, *Electrochim. Acta* 45 (2000) 4227.
- [13] N. Alonso-Vante, P. Bogdanoff, H. Tributsch, *J. Catal.* 190 (2000) 240.
- [14] N. Alonso-Vante, I. V. Malakhov, S. G. Nikitenko, E. R. Savinova, D. I. Kochubey, *Electrochim. Acta* 47 (2002) 3807.
- [15] I. V. Malakhov, S. G. Nikitenko, E. R. Savinova, D. I. Kochubey, N. Alonso-Vante, *J. Phys. Chem. B* 106 (2002) 1670.

- [16] H. R. Chauke, D. Nguyen-Manh, P. E. Ngoepe, D. G. Pettifor, S. G. Fries, *Phys. Rev. B* 66 (2002) 155105/1.
- [17] J. Buriak, *Science* 304 (2004) 692.
- [18] Y. Yin, R. M. Rioux, C. K. Erdonmez, S. Hughes, G. A. Somorjai, A. P. Alivisatos, *Science* 304 (2004) 711.
- [19] J. Roques, A. B. Anderson, V. S. Murthi, S. J. Mukerjee, *J. Electrochem. Soc.* 152(6) (2005) E193.
- [20] J. Roques, A. B. Anderson, *Surf. Sci.* 581(2-3) (2005) 105.
- [21] J. Roques, A. B. Anderson, *J. of Fuel Cell Sci. and Tech.* 2(2) (2005) 86.
- [22] J. Roques, A. B. Anderson, *J. Electrochem. Soc.* 151(11) (2004) E340.
- [23] J. Roques, A. B. Anderson, *J. Electrochem. Soc.* 151(3) (2004) E85.
- [24] G. Kresse, Furthmuller, *Phys. Rev. B* 54 (1996) 11169.
- [25] G. Kresse, Hafner, *Phys. Rev. B* 47 (1993) 558.
- [26] G. Kresse, Hafner, *Phys. Rev. B* 49 (1994) 14251.
- [27] G. Kresse, Furthmuller, *J. Compt. Mater. Sci.* 6 (1996) 15.
- [28] G. Kresse, Hafner, *J. Phys.: Condens. Matter.* 6 (1994) 8245.
- [29] J. P. Perdew, Y. J. Wang, *Phys. Rev. B* 45 (1992) 13244.
- [30] D. M. Wood, A. Zunger, *J. Phys. A* 18 (1985) 1343.
- [31] H. J. Monkhorst, J. D. Pack, *Phys. Rev. B* 13 (1976) 5188.
- [32] M. Methfessel, A. T. Paxton, *Phys. Rev. B* 40 (1989) 3616.
- [33] R. W. G. Wyckoff, *Crystal Structures*; John Wiley & Sons: New York, 1964.
- [34] T. V. Albu, A. B. Anderson, *J. Electrochem. Soc.* 147 (2000) 4229.
- [35] C. E. Mooney, L. C. Anderson, J. Lunsford, *J. Phys. Chem.* 97 (1993) 2505.
- [36] B. A. Sexton, A. E. Hughes, *Surf. Sci.* 140 (1984) 227.
- [37] Taken from or derived from data given in A. J. Bard, R. Parsons, J. Jordan, *Standard Potentials in Aqueous Solution*; Marcel Dekker Inc.: New York and Basel, 1985.
- [38] N. M. Markovic, T. J. Schmidt, B. N. Grgur, H. A. Gasteiger, R. J. Behm, P. N. Ross, *J. Phys. Chem. B* 103 (1999) 8568.

- [39] S. Mukerjee, S. Srinivasan, M. P. Soriaga, J. McBreen, J. Electrochem. Soc., 142 (1995) 1409.
- [40] T. Iwasita, X. Xia, J. Electroanal. Chem. 411 (1996) 95.
- [41] N. M. Markovic, P. N. Ross, Surf. Sci. Rep. 45 (2002) 117.
- [42] V. Stamenkovic, Y. J. Schmidt, P. N. Ross, N. M. Markovic, J. Phys. Chem. B 106 (2002) 11970.
- [43] F. A. Uribe, T. A. Zawodzinski, Electrochim. Acta 47 (2002) 3799.
- [44] A. B. Anderson, J. Roques, S. Mukerjee, V. S. Murthi, N. M. Markovic, V. Stamenkovic, J. Phys. Chem. B 109 (2005) 1198.
- [45] H. Schweiger, E. Vayner, A. B. Anderson, J. Electrochem. Solid State Lett. 8 (2005) A585.
- [46] E. Vayner, H. Schweiger, A. B. Anderson, J. Electroanal. Chem. 000 (2007) 000.
- [47] See, for example, A. B. Anderson, Y. Cai, R. A. Sidik, D-B Kang, J. Electroanal. Chem. 580 (2005) 17.
- [48] Binary Alloy Phase Diagrams, 2nd ed.; T. B. Massalski, H. Okamoto, P. R. Subramanian, L. Kacprzak, Eds.; ASM International: Materials Park, OH, 1990; Vol. 2, pp. 1235-1237.

7.2. EFFECT OF HYDROPHOBICITY AND PORE GEOMETRY IN CATHODE GDL ON PEM FUEL CELL PERFORMANCE

7.2.1. Introduction

In proton exchange membrane fuel cells (PEMFCs), the humidified fuel and oxidant are introduced to the anode and the cathode compartments to keep the membrane from dehydration. At high current densities, excessive water is produced by the cathodic reaction, which significantly blocks the pores available for oxygen transport in the gas diffusion layer (GDL) and covers the active sites in the catalyst layer [1-2].

Extensive theoretical works have been performed to study flooding phenomena in PEM fuel cells [3-8]. Springer et al. [3] developed a one-dimensional PEM fuel cell model. They showed that the limiting current is directly connected to the effective porosity controlled by water content in the GDL. Baschuck and Li [4] assumed a layer of liquid water between the GDL and the catalyst layer to describe partially flooded cathode, and demonstrated flooding levels at various pressures and temperatures.

Based on Darcy's law, two-phase transport models for PEM fuel cells have been proposed [5-8]. He et al. [5] presented the effects of liquid water flow across the cathode GDL, driven by capillary pressure, on the fuel cell performance. Wang et al. [6] introduced Leverett J -function to correlate capillary pressure with saturation to depict the effect of flooding as a function of saturation. Recently, Pasaogullari and Wang [7] derived a one-dimensional analytical solution for liquid water transport across the hydrophobic GDL, assuming that no saturation occurs at the interface between the gas flow channel (GFC) and the GDL. Weber et al. [8] examined the effect of hydrophobicity of a single-layer GDL which, consists of two separate pore networks (i.e., hydrophilic pores and hydrophobic pores), on water management. Their simulation showed that when the hydrophobicity of a GDL increases, a maximum power is determined by the trade-offs between mass-transfer benefits and ohmic losses. However, the dependency of water management on both hydrophobic and structural properties of the cathode GDL has not been addressed in literature extensively. The objective of this work is to investigate the effect of hydrophobicity and pore geometry on the transport of liquid water and oxygen across the hydrophobic cathode GDL in PEM fuel cells.

7.2.2. Mathematical Model Development

The capillary pressure p_c in a hydrophobic diffusion layer is generally expressed as [9,10]:

$$p_c = \frac{\sigma \cos \theta_c}{(K_{\text{abs}}/\varepsilon)^{1/2}} (1.417s - 2.120s^2 + 1.263s^3) \quad (7-2-1)$$

where σ and θ_c represent the surface tension of liquid water and the contact angle of liquid water on the solid surface, respectively. K_{abs} , ε , and s denote the absolute permeability, the bulk porosity and the liquid water saturation in a diffusion layer, respectively. The liquid phase permeability K_l is defined as [11]:

$$K_l = K_{\text{abs}} K_{rl} = K_{\text{abs}} s^3 \quad (7-2-2)$$

where K_{rl} is the relative permeability of the liquid phase, which is equivalent to the cube of liquid saturation. A dual-layer GDL is made up of the macroporous substrate (MPS) and the microporous layer (MPL). The former consists of carbon fiber and hydrophobic agent, and the latter comprises carbon powder and hydrophobic agent. Hence, the contact angle for a composite diffusion layer which contains hydrophilic material (e.g., carbon) and hydrophobic agent (e.g., PTFE) can be expressed as [8,11]:

$$\theta_c = \cos^{-1} [f_{\text{HI}} \cos \theta_{\text{HI}} + (1 - f_{\text{HI}}) \cos \theta_{\text{HO}}] \quad (7-2-3)$$

where f_{HI} denotes the fraction of hydrophilic surface in a diffusion layer, and θ_{HI} and θ_{HO} are the hydrophilic contact angle and the hydrophobic contact angle. According to literature, the contact angle for the graphite ranges from 49° to 82° and the PTFE contact angle is between 98.6° and 124° [12,13]. Based on the assumptions that (i) a diffusion layer is isothermal, (ii) the gas phase pressure p_g is constant (i.e., fully saturated), and (iii) the catalyst layer is infinitely thin, one-dimensional solution of liquid water transport through a diffusion layer has been derived analytically as [7]:

$$s^4 (0.35425 - 0.8480s + 0.6135s^2) = \frac{i}{2F} M_{\text{H}_2\text{O}} (1 + 2\alpha) \frac{\nu}{\sigma \cos \theta_c (\varepsilon K_{\text{abs}})^{1/2}} x + C_1 \quad (7-2-4)$$

where i is the current density, F is the Faraday constant, $M_{\text{H}_2\text{O}}$ molecular weight of water, α is the net water transport coefficient, ν is the kinematic viscosity of liquid water, and x is the distance in through-plane direction for a diffusion layer. The integration constant C_1 depends on the boundary condition. The average saturation in a diffusion layer s_{avg} at a given current density is defined as:

$$s_{\text{avg}} = \frac{\int_0^\delta s(x) dx}{\delta} \quad (7-2-5)$$

where δ denotes the thickness of the diffusion layer. At zero capillary pressure (i.e., $p_g = p_l$), all the hydrophilic surface is covered with the liquid water and all the hydrophobic surface remains

undamped in the absence of residual saturation of the gas phase [11,14]. Under the assumption that the capillary pressure at the interface between the GFC and the MPS is zero, the liquid water saturation at the GFC/MPS interface corresponds to f_{HI} and hence the integration constant C_1 is calculated from the liquid water saturation at this interface. In a single-layer GDL, the capillary pressure with respect to liquid saturation shows a continuous profile. However, for a dual-layer GDL which consists of the MPS and the MPL, there exists a discontinuity in liquid saturation at the interface between the MPS and the MPL because of different hydrophobic and structural properties [10,11].

The gas-phase diffusion within pores of a diffusion layer can be split into bulk diffusion and Knudsen diffusion. The diffusion coefficient is corrected for the average saturation and tortuosity using Bruggeman correlation. Hence, the effective diffusion coefficient is as follows [15]:

$$D^{\text{eff}} = \left(\frac{1}{D^{\text{eff}}} + \frac{1}{D_K^{\text{eff}}} \right)^{-1} = [\varepsilon(1 - s_{\text{avg}})]^{1.5} \left(\frac{1}{D} + \frac{1}{D_K} \right)^{-1} \quad (7-2-6)$$

The Knudsen diffusion coefficient for species i is given by

$$D_{K,i} = \frac{d_{\text{avg}}}{3} \left(\frac{8RT}{\pi M_i} \right)^{1/2} \quad (7-2-7)$$

where d_{avg} is the average pore diameter in a diffusion layer, R and T are the gas constant and the absolute temperature, and M_i is the molecular weight of species i . In this study, the Knudsen diffusion was taken into account for the MPL.

At steady state, the molar flux of oxygen through each domain is the same. i.e.,

$$j_{\text{O}_2}^{\text{GFC}} = j_{\text{O}_2}^{\text{MPS}} = j_{\text{O}_2}^{\text{MPL}} = j_{\text{O}_2} \quad (7-2-8)$$

When the oxygen are assumed as an ideal gas, the molar flux of oxygen from the GFC to the interface between the MPL and the membrane (i.e., the reaction site) is given as

$$j_{\text{O}_2} = \frac{p}{RT} \left(\frac{x_{\text{lm,O}_2}^{\text{GFC}} - x_{\text{O}_2}^{\text{MPL/mem}}}{\frac{\delta^{\text{MPS}}}{D_{\text{O}_2\text{-air}}^{\text{eff,MPS}}} + \frac{\delta^{\text{MPL}}}{D_{\text{O}_2\text{-air}}^{\text{eff,MPL}}} + \frac{1}{k_c}} \right) \quad (7-2-9)$$

where $x_{\text{lm,O}_2}^{\text{GFC}}$ is the logarithmic mean mole fraction of oxygen in the GFC⁸, and $x_{\text{O}_2}^{\text{MPL/mem}}$ is the mole fraction of oxygen at the interface between the MPL and the membrane, respectively. δ^{MPS} and δ^{MPL} are the thicknesses of the MPS and the MPL. k_c is the convective mass-transfer coefficient at the interface between the GFC and the MPS. It was determined using the analogy

between heat and mass-transfer [6,7,16]. $D_{O_2\text{-air}}^{\text{eff}}$ is the effective diffusion coefficient of oxygen in air. Since the mole flux of oxygen is equal to its consumption rate at the interface between the MPL and the membrane, the mole flux of oxygen is expressed using the Tafel equation, based on the assumption that the anodic contribution is negligibly small [17-19].

$$j_{O_2} = \frac{i}{4F} = \frac{1}{4F} \left[(1 - s^{\text{MPL/mem}}) a i_0^{\text{ref}} \delta_{\text{CL}} \frac{x_{O_2}^{\text{MPL/mem}}}{x_{O_2}^{\text{ref}}} \exp\left(-\frac{\alpha_c F}{RT} \eta\right) \right] \quad (7-2-10)$$

where $s^{\text{MPL/mem}}$ is the saturation at the interface between the MPL and the membrane, a is the specific electrochemically active area, i_0^{ref} is the cathodic reference exchange current density, δ_{CL} is the catalyst layer thickness, and α_c is the cathodic transfer coefficient. Combining Eq. (7-2-9) with Eq. (7-2-10), the overpotential for a PEM fuel cell is derived as follows.

$$\eta = \frac{RT}{\alpha_c F} \ln \left[\frac{p}{RT} \frac{i x_{O_2}^{\text{ref}}}{(1 - s^{\text{MPL/mem}}) a i_0^{\text{ref}} \delta_{\text{CL}}} \times \frac{1}{\frac{p}{RT} x_{\text{lm},O_2}^{\text{GFC}} - \frac{i}{4F} \left[\frac{\delta^{\text{MPS}}}{D_{O_2\text{-air}} [\varepsilon^{\text{MPS}} (1 - s_{\text{avg}}^{\text{MPS}})]^{1.5}} + \left(\frac{1}{D_{O_2\text{-air}}} + \frac{1}{D_{K_{O_2}}} \right) \frac{\delta^{\text{MPL}}}{[\varepsilon^{\text{MPL}} (1 - s_{\text{avg}}^{\text{MPL}})]^{1.5}} + \frac{1}{k_c} \right]} \right] \right] \quad (7-2-11)$$

Eq. (7-2-11) includes the contribution of the MPL to the liquid water flow as well as the oxygen transport which in above equation was divided into the bulk and Knudsen diffusion. The interactions of the MPL with the liquid water flow and oxygen transport were not taken into account in the analytical form derived by Pasagullari and Wang [7]. Also, the average saturations at each layer as a function of current density, in lieu of a constant saturation at the cathode over the current density, were employed to determine the effective porosity. Once the ohmic losses originate mostly from ionic transport through the membrane and the electrodes, the cell potential can be determined by

$$E_{\text{cell}} = E_{\text{oc}} - \eta - iR \quad (7-2-12)$$

$$iR = i \left(\frac{\delta_{\text{mem}}}{\kappa_{\text{mem}}} + 2R_e \right) \quad (7-2-13)$$

where E_{oc} is the open circuit potential, δ_{mem} is the membrane thicknesses ($= 50 \mu\text{m}$), κ_{mem} is the ionic conductivity of membrane, and R_e is the electrode ohmic resistance.

7.2.3. Results and Discussion

Fig. 7-2-1 demonstrates the bulk porosity with respect to average pore diameter for the MPS with different PTFE contents (Carbon Cloth Type A, E-TEK). The bulk porosity and the average pore diameter were measured using the mercury porosimeter (Micromeritics Autopore 9500).

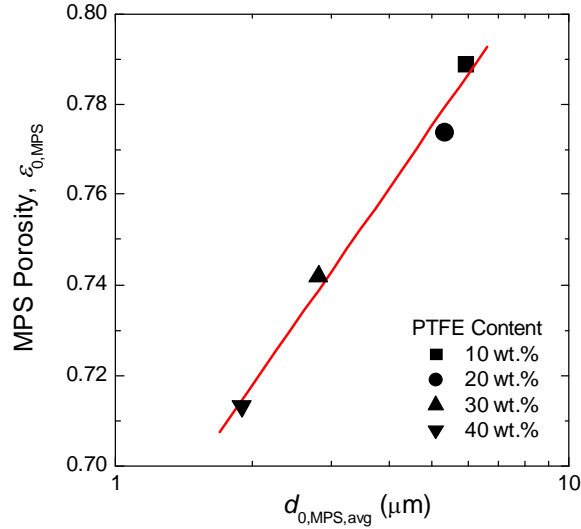


Fig. 7-2-1. Bulk porosity with respect to average pore diameter for MPS with different PTFE contents.

As seen in Fig. 7-2-1, the bulk porosity in the MPS $\epsilon_{0,MPS}$ can be correlated with the average pore diameter in the MPS $d_{0,MPS,avg}$. That is,

$$\epsilon_{0,MPS} = 0.14437 \log d_{0,MPS,avg} + 1.54058 \quad (7-2-14)$$

The empirical equation is used to estimate the absolute permeability K_{abs} [11]:

$$K_{abs} = K_{abs}^{ref} \left(\frac{\epsilon}{\epsilon_{ref}} \right) \left(\frac{d_{avg}}{d_{avg}^{ref}} \right)^2 \quad (7-2-15)$$

The MEA is typically compressed in order to keep good electrical contacts between each component. Hence, the bulk porosity in a diffusion layer reduces on compression, depending on clamping force. The bulk porosity in a compressed diffusion layer ϵ is estimated as [20]:

$$\epsilon = 1 - \frac{\delta_0}{\delta} (1 - \epsilon_0) \quad (7-2-16)$$

where ϵ_0 and δ_0 denote the uncompressed diffusion layer porosity and thickness. The values of δ_0/δ were given 1.125 for the MPS and 1.050 for the MPL in this study. The various parameters and conditions used in the model are summarized in Table 7-2-1.

Table 7-2-1. Values for various simulation parameters and physical properties.

Parameter	Unit	Value
Cell temperature T	°C	75
Total gas pressure p	atm	1
Uncompressed MPS thickness $\delta_{0,MPS}$	μm	450
Hydrophilic surface contact angle θ_{HI} [8,12]	°	80
Hydrophobic surface contact angle θ_{HO} [8,13]	°	110
Surface tension in liquid-water-air σ [21]	N m^{-1}	0.0635
Liquid water kinematic viscosity ν [21]	$\text{m}^2 \text{s}^{-1}$	3.85×10^{-5}
Net water transport coefficient α [10]		0.5
Oxygen diffusion coefficient in air $D_{O_2\text{-air}}$ [21]	$\text{m}^2 \text{s}^{-1}$	2.65×10^{-5}
Convective mass transfer coefficient k_c	m s^{-1}	0.087
Oxygen mole fraction in the gas flow channel x_{Im,O_2}^{GFC}		0.098
Specific electrochemically active area - cathodic reference exchange current density ai_0^{ref}	A m^{-3}	15,000
Compressed catalyst layer thickness δ_{CL}	μm	10
Cathodic transfer coefficient α_c [8]		1
Open circuit potential	V	1.08
Membrane conductivity κ_{mem} [22]	S cm^{-1}	0.12
Electrode ohmic resistance R_e [23]	$\Omega \text{ cm}^2$	0.05

A model fit to experimental data reported in [3] is shown in Fig. 7-2-2. Parameters used for the fitting are given in Table 7-2-2. In the figure, the simulation demonstrates good agreement to the polarization curve obtained using the hydrophobized cathode with the air feed.

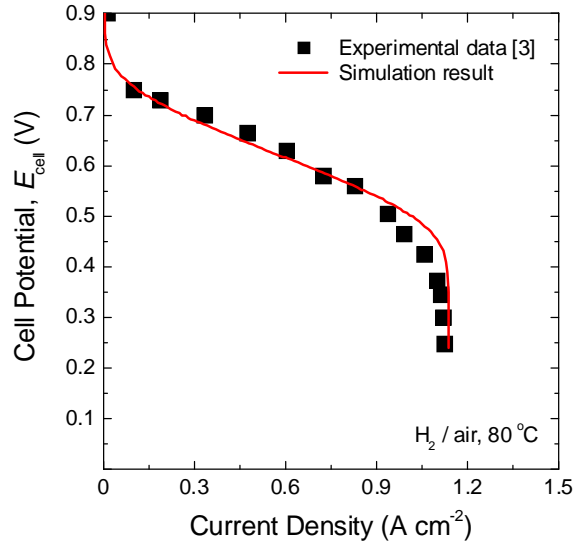


Fig. 7-2-2. Comparison of model and experimental polarization curves. Parameters are given in Table 7-2-2 and the data are from [3].

Table 7-2-2. Values for the simulation parameters for the fitting.^a

Parameter	Unit	Value
Cell temperature T	°C	80
Compressed MPS thickness δ_{MPS}	μm	300
Fraction of hydrophilic surface		0.564
Average pore diameter in MPS	μm	5.9
Surface tension in liquid-water-air σ [21]	N m^{-1}	0.0626
Liquid water kinematic viscosity ν [21]	$\text{m}^2 \text{s}^{-1}$	3.65×10^{-5}
Oxygen diffusion coefficient in air $D_{\text{O}_2\text{-air}}$ [21]	$\text{m}^2 \text{s}^{-1}$	2.71×10^{-5}
Convective mass-transfer coefficient	m s^{-1}	0.089
Oxygen mole fraction in the gas flow channel, $x_{\text{lm},\text{O}_2}^{\text{GFC}}$		0.071
Membrane conductivity κ_{mem} [22]	S cm^{-1}	0.15
Compressed catalyst layer thickness δ_{CL} [3]	μm	4

^a Parameters which are not given in Table 7-2-2 for the fitting are taken from Table 7-2-1.

Fig. 7-2-3(a) shows saturation profile across the MPS with different average pore diameters. The simulations were performed at 1.0 A cm^{-2} and $f_{\text{HL},\text{MPS}} = 0.6$. As illustrated in Fig. 7-2-3(a), by increasing the average pore diameter in the MPS, the saturation in the MPS becomes smaller. This is due primarily to the dependency of the absolute permeability K_{abs} on the average pore

diameter $d_{0,\text{MPS,avg}}$. i.e., a MPS with larger $d_{0,\text{MPS,avg}}$ leads to a better liquid water transport. Fig. 7-2-3(b) depicts polarization curves as a function of average pore diameter in the MPS. The performance is nearly identical at low current densities. However, it increases with higher $d_{0,\text{MPS,avg}}$ at high current densities. At this region, the oxygen transport is restricted by liquid water within the pores, causing the limiting current. The results indicate that larger $d_{0,\text{MPS,avg}}$ facilitates both liquid water flow and oxygen counter flow through the MPS at constant level of hydrophobicity.

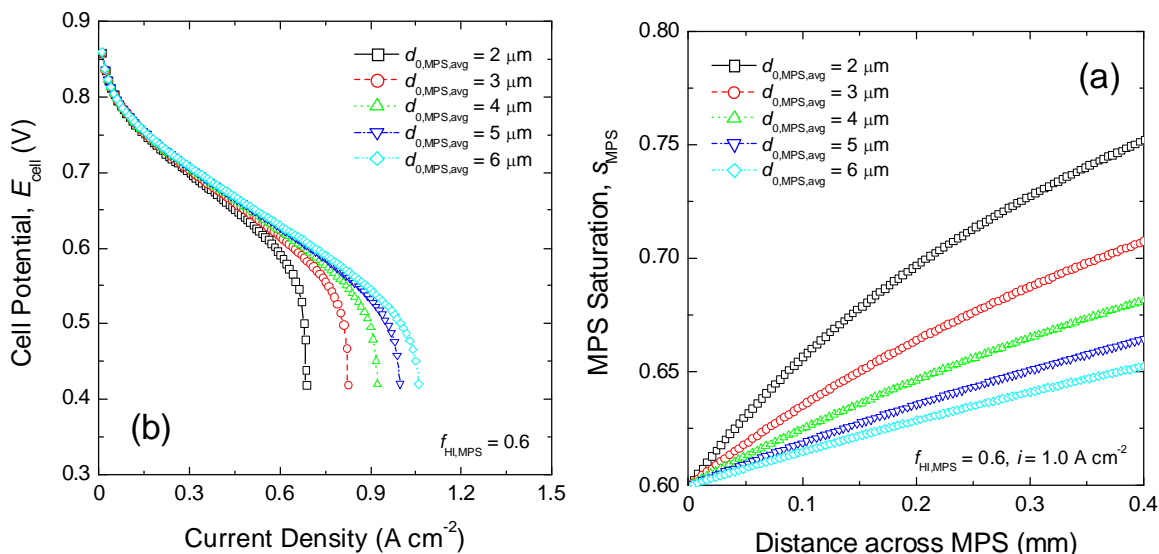


Fig. 7-2-3. (a) Saturation profile across the MPS with average pore diameter. (b) Polarization curves with average pore diameter in the MPS.

Fig. 7-2-4(a) presents the saturation profile across the MPS with different fractions of hydrophilic surface. The saturation profile was obtained at 1.0 A cm^{-2} and $d_{0,\text{MPS,avg}} = 6 \mu\text{m}$. It is seen that the saturation level across the MPS increases with higher $f_{\text{HL,MPS}}$. Furthermore, by decreasing fraction of hydrophilic surface in the MPS, the saturation gradient across the MPS becomes large. This indicates that at constant $d_{0,\text{MPS,avg}}$, more hydrophobic MPS removes liquid water effectively. Fig. 7-2-4(b) gives the polarization curves as a function of $f_{\text{HL,MPS}}$. It is observed that the performance increases with smaller $f_{\text{HL,MPS}}$. The reason is that a smaller $f_{\text{HL,MPS}}$ leads to a lower liquid saturation in the MPS, resulting in a smaller oxygen concentration gradient at the cathode.

Practically, when the amount of the hydrophobic agent impregnated into the pores increases, both the fraction of hydrophilic surface f_{HI} and the average pore diameter $d_{0,\text{avg}}$ in a diffusion layer reduce. In addition, the distribution of the hydrophobic agent throughout a diffusion layer depends on drying rate during sintering, and thickness of a diffusion layer.^{24,25} It may result in

the gradient of f_{HI} with respect to $d_{0,avg}$. Hence, f_{HI} as a function of $d_{0,avg}$ can be used to describe the interaction between wettability and pore structure as follows:

$$f_{HI} = 0.6 - b \log\left(\frac{6 - d_{0,avg}}{0.1} + 1\right) \quad (7-2-17)$$

where b is a constant which governs the gradient of f_{HI} with respect to $d_{0,avg}$. Fig. 7-2-5(a) exhibits f_{HI} as a function of $d_{0,avg}$ using Eq. (7-2-17). As seen in Fig. 7-2-5(a), when b increases from 0 to 0.16, f_{HI} can be as low as ca. 0.32. Fig. 7-2-5(b) displays the average saturation in the MPS $s_{MPS,avg}$ at various gradients of $f_{HI,MPS}$ with respect to $d_{0,MPS,avg}$ using Eq. (7-2-17). The simulations were performed at 1.0 A cm^{-2} . As expected, $s_{MPS,avg}$ decreases with higher $d_{0,MPS,avg}$ in the absence of the gradient of $f_{HI,MPS}$ (case 1 in this figure). As seen in Fig. 7-2-5(b), however, a minimum value of $s_{MPS,avg}$ appears when there exists a gradient of $f_{HI,MPS}$ with respect to $d_{0,MPS,avg}$. It shifts negatively with higher b . This minimum arises from the interplay between $d_{0,MPS,avg}$ and $f_{HI,MPS}$. The former is intimately coupled with the liquid water permeability through the MPS and the latter is represented by the contact angle of liquid water on the MPS.

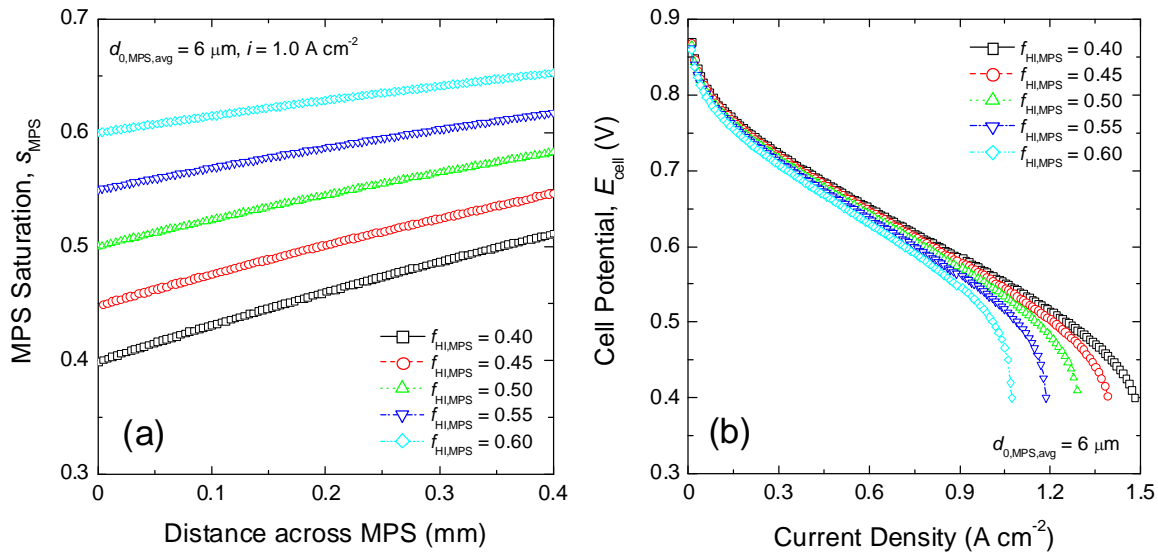


Fig. 7-2-4. (a) Saturation profile across the MPS with fraction of hydrophilic surface. (b) Polarization curves with fraction of hydrophilic surface in the MPS.

Fig. 7-2-6(a) delineates the saturation profiles across the MPS with different pairs of $d_{0,MPS,avg}$ and $f_{HI,MPS}$. The values of $f_{HI,MPS}$ were calculated using Eq. (7-2-17) (case 4 in Fig. 7-2-5(a)). The saturation profile was obtained at 1.0 A cm^{-2} . It appears that s_{MPS} increases with higher $d_{0,MPS,avg}$ and $f_{HI,MPS}$ near the interface between the GFC and the MPS. However, s_{MPS} decreases at the interface between the MPS and the membrane in the order: $2 > 6 > 3 > 4 > 5 \text{ μm}$. The

observed liquid water saturation can be explained as follows: $f_{\text{HL,MPS}}$ dominantly control the saturation near the GFC/MPS interface due to low capillary pressure. On the other hand, at the MPS/membrane interface, $d_{0,\text{MPS,avg}}$ is of great importance because of high flux of liquid water from the catalyst layer. Fig. 7-2-6(b) demonstrates the polarization curves using the MPS with different pairs of $d_{0,\text{MPS,avg}}$ and $f_{\text{HL,MPS}}$. The performance reaches a maximum when $d_{0,\text{MPS,avg}}$ is 5 μm and $f_{\text{HL,MPS}}$ is 0.475. It originates primarily from lower liquid water saturation, as shown in Fig. 7-2-6(a).

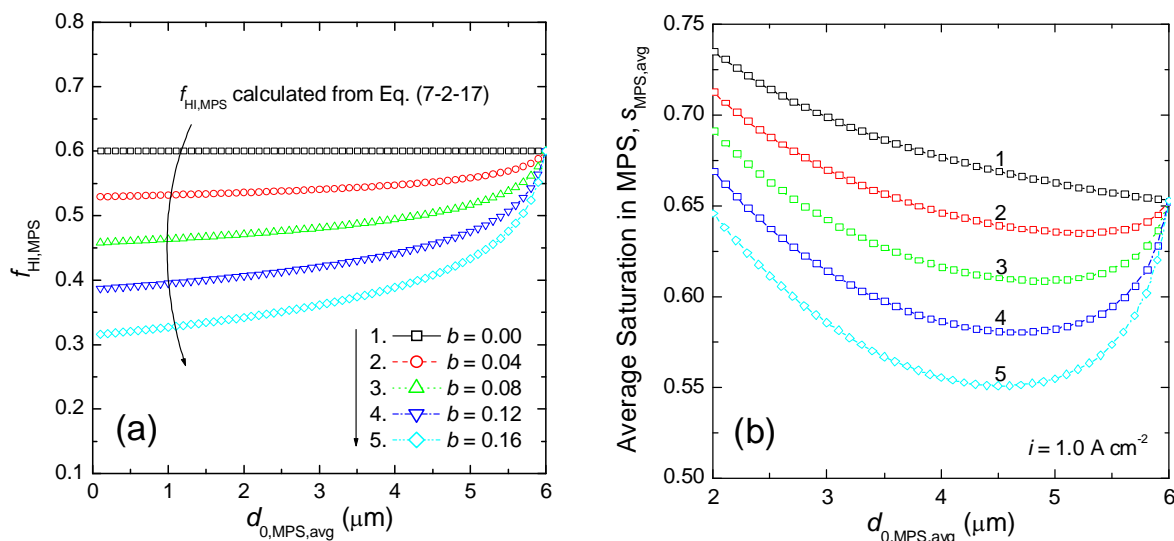


Fig. 7-2-5. (a) Gradients of fraction of hydrophilic surface with respect to average pore diameter in a diffusion layer. (b) Average saturation in the MPS with gradient of fraction of hydrophilic surface with respect to average pore diameter.

The MPL reduces the contact resistance between the catalyst layer and the MPS, and improves water management at the cathode [10,26-28]. The MPL is deposited onto the MPS using various coating methods: spraying, tape-casting, screen-printing, brushing, etc [2,29]. Hence, part of the MPL is entrenched into the MPS, resulting in change in the pore volume available for mass transport through the MPS [27,28]. Therefore, it is necessary to take into account the change of the MPS properties in the presence of the MPL. Table 7-2-3 lists simulated properties of the MPS with and without the MPL. Fig. 7-2-7(a) represents the saturation profile across a dual-layer GDL, which consists of the MPS and the MPL. The saturation profile was obtained at 1.0 A cm^{-2} . As seen in Fig. 7-2-7(a), sudden drops of the saturation at the interface between the MPS and the MPL are distinctively observed, which is due to the difference in the pore size and the hydrophobic characteristic between the MPL and the MPS. The saturation profile across the MPS without the MPL is also presented in Fig. 7-2-7(a). It is seen that the MPS with the MPL shows a lower saturation across the MPS than that without the MPL. This means that the deposition of the MPL facilitates liquid water removal due to the

decreased $f_{HI,MPS}$, although it decreases somewhat $d_{0,MPS,avg}$. It is also observed that saturation level in the MPL decreases with increasing $d_{0,MPL,avg}$ and then it increases with further increasing $d_{0,MPL,avg}$. This is because $d_{0,MPL,avg}$ controls saturation levels at the interface between the MPS and the MPL, as well as the gradient of saturation across the MPL.

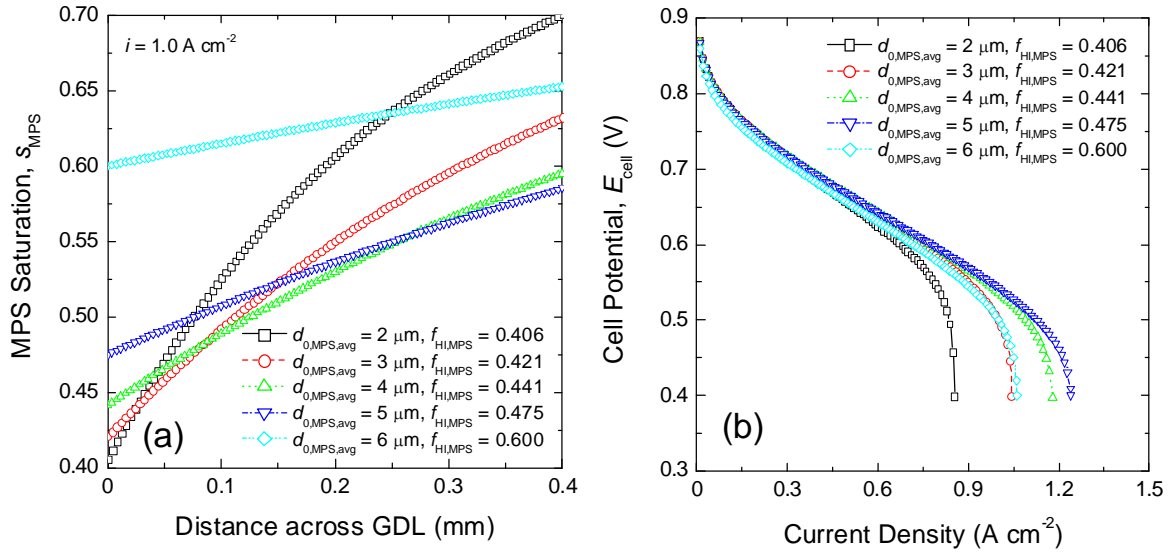


Fig. 7-2-6. (a) Saturation profile across the MPS at various pairs of the average pore diameter and fraction of hydrophilic surface. (b) Polarization curves using the MPS at various pairs of the average pore diameter and fraction of hydrophilic surface.

Table 7-2-3. Values for physical properties of the MPS with and without the MPL.

Parameter	Unit	Value
without MPL		
Uncompressed average pore diameter in MPS $d_{0,MPS,avg}$	μm	6
Fraction of hydrophilic surface in MPS $f_{HI,MPS}$		0.6
with MPL		
Uncompressed average pore diameter in MPS $d_{0,MPS,avg}$	μm	5.5
Fraction of hydrophilic surface in MPS $f_{HI,MPS}$		0.45
Fraction of hydrophilic surface in MPL $f_{HI,MPL}$		0.3
Uncompressed thickness of MPL $\delta_{0,MPL}$	μm	25

On the other hand, $s_{MPL,avg}$ as a function of $f_{HI,MPL}$ remains almost constant, as seen in Fig. 7-2-7(a) (see the inset). Thus, these results indicate that $d_{0,MPL,avg}$ mainly influences the saturation in the MPL. Fig. 7-2-7(b) gives the polarization curves using the MPL with different $d_{0,MPL,avg}$. The polarization curve obtained using no MPL was also presented in Fig. 7-2-7(b) for comparison. Fig. 7-2-7(b) displays that the MPL results in an improved fuel cell performance which is vastly dependent on average pore diameter in the MPL.

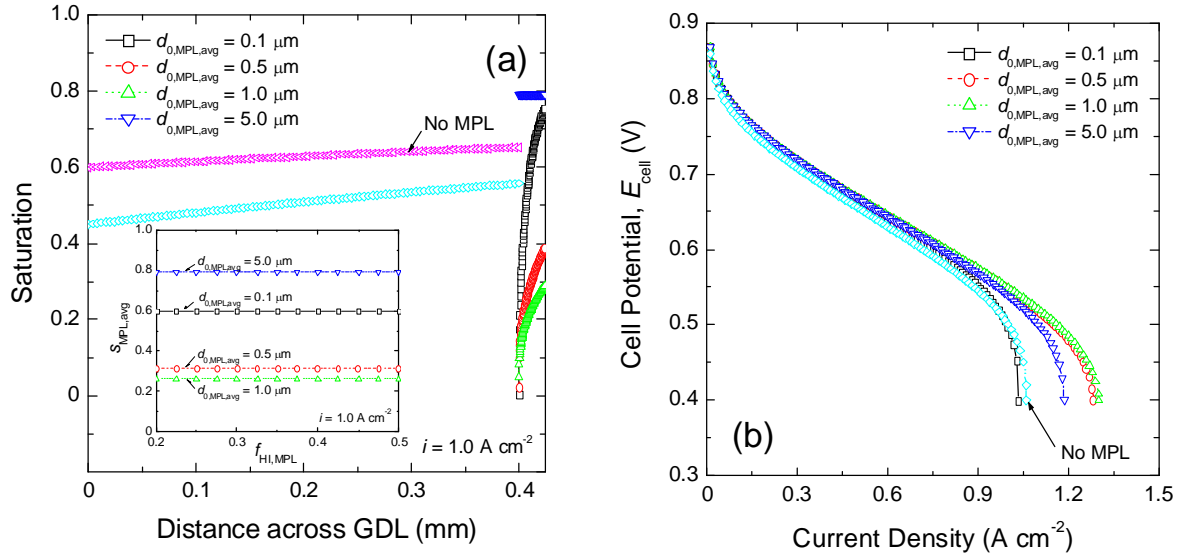


Fig. 7-2-7. (a) Saturation profile across the GDL with average pore diameter in the MPL. (b) Polarization curves with average pore diameter in the MPL.

As mentioned earlier, the gradient of $f_{HI,MPS}$ with respect to $d_{0,MPS,avg}$ affects saturation profile and hence controls the performance. Similarly, to examine the effect of the gradient of $f_{HI,MPL}$ with respect to $d_{0,MPL,avg}$, saturation profile and polarization curve were generated. Fig. 7-2-8(a) exhibits saturation profile for a dual-layer GDL with different gradients of $f_{HI,MPL}$ with respect to $d_{0,MPL,avg}$. The saturation profile was obtained at 1.0 A cm^{-2} . On the other hand, a reduced $f_{HI,MPS}$ due to the deposition of a hydrophobic MPL was given as a logarithmic mean between $f_{HI,MPS}$ without the MPL ($= 0.6$) and $f_{HI,MPL}$ determined by Eq. (7-2-17) (case 4 in Fig. 7-2-5(a)). As illustrated in Fig. 7-2-8(a), a minimum saturation in the MPL is observed for $d_{0,MPL,avg} = 1.0 \text{ μm}$ and $f_{HI,MPL} = 0.395$. However, the saturation level in the MPS decreases and then it reduces slightly with lower $f_{HI,MPL}$. This is due to the fact that the deposition of MPL with higher content of hydrophobic agent makes the MPS more hydrophobic. Fig. 7-2-8(b) exhibits the polarization curves using the MPL with different pairs of $d_{0,MPL,avg}$ and $f_{HI,MPL}$.

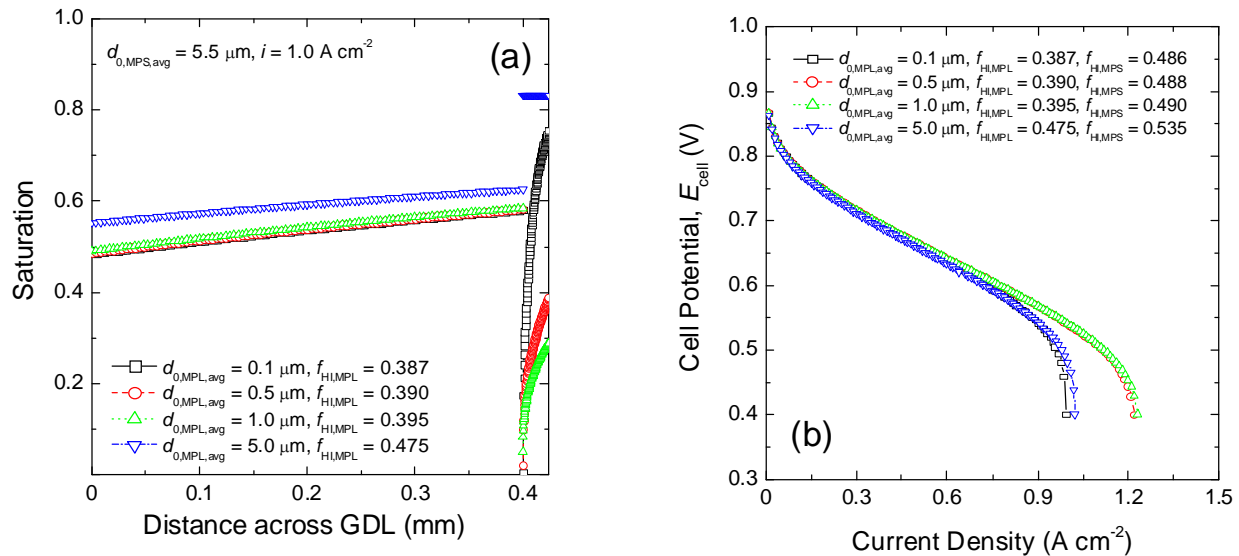


Fig. 7-2-8. (a) Saturation profile across the GDL at various pairs of the average pore diameter and fraction of hydrophilic pore in the MPL. (b) Polarization curves using the MPL at various pairs of the average pore diameter and fraction of hydrophilic pore.

A maximum performance is obtained with the MPL which has $d_{0,MPL,avg} = 1.0 \mu\text{m}$ and $f_{HI,MPL} = 0.395$, in the presence of the gradient of $f_{HI,MPL}$ with respect to $d_{0,MPL,avg}$ (case 4 in Fig. 7-2-5(a))

7.2.4. Conclusions

The results in this study indicated that water saturation at the cathode is affected by the fraction of hydrophilic surface and the average pore diameter in the macroporous substrate, and the average pore diameter in the microporous layer. Deposition of a hydrophobic microporous layer reduces the fraction of hydrophilic surface in the MPS, allowing faster water removal from the cathode.

7.2.5. References

- [1] F.N. Büchi, S. Srinivasan, J. Electrochem. Soc. 144 (1997) 2767.
- [2] F. Barbir, PEM Fuel Cells, Elsevier Academic Press, Burlington, 2005.
- [3] T.E. Springer, M.S. Wilson, S. Gottesfeld, J. Electrochem. Soc. 140 (1993) 3513.
- [4] J.J. Baschuk, X. Li, J. Power Sources 86 (2000) 181.

- [5] W. He, J.S. Yi, T.V. Nguyen, *AIChE J.* 46 (2000) 2053.
- [6] Z.H. Wang, C.Y. Wang, K.S. Chen, *J. Power Sources* 84 (2001) 40.
- [7] U. Pasaogullari, C.Y. Wang, *J. Electrochem. Soc.* 151 (2004) A399.
- [8] A.Z. Weber, R.M. Darling, J. Newman, *J. Electrochem. Soc.* 151 (2004) A1715.
- [9] M. Kaviany, *Principles of heat transfer in porous media*, Springer-Verlag, New York, 1991.
- [10] J.H. Nam, M. Kaviany, *Int. J. Heat Mass Transfer*, 46 (2003) 4595.
- [11] J. Bear, *Dynamics of Fluids in Porous Media*, Dover Publications, New York, 1988.
- [12] M.E. Schrader, *J. Phys. Chem.* 79 (1975) 2508.
- [13] C.W. Extrand, Y. Kumagai, *J. Colloid Interface Sci.* 170 (1995) 515.
- [14] A.Z. Weber, J. Newman, *Chem. Rev.* 104 (2004) 4679.
- [15] R.H. Perry, D.W. Green, *Perry's Chemical Engineers' Handbook*, seventh ed., McGraw-Hill, New York, 1997.
- [16] Y. Bayazitoğlu, M.N. Özişik, *Elements of Heat Transfer*, McGraw-Hill, New York, 1988.
- [17] A.J. Bard, L.R. Faulkner, *Electrochemical Method*, second ed., John Wiley & Sons, New York, 2001.
- [18] H. Meng, C.-Y. Wang, *J. Electrochem. Soc.* 152 (2005) A1733.
- [19] H. Ju, G. Luo, C.-Y. Wang, *J. Electrochem. Soc.* 154 (2007) B218.
- [20] J.P. Feser, A.K. Prasad, S.G. Advani, *J. Power Sources* 162 (2006) 1226.
- [21] F.P. Incropera, D.P. DeWitt, *Fundamentals of Heat and Mass Transfer*, fourth ed., John Wiley & Sons, New York, 1996.
- [22] K.D. Kreuer, M. Schuster, B. Obliers, O. Diat, U. Traub, A. Fuchs, U. Klock, S.J. Paddison, J. Maier, *J. Power Sources* 178 (2008) 499.
- [23] G. Li, P.G. Pickup, *J. Electrochem. Soc.* 150 (2003) C745.
- [24] D. Bevers, R. Rogers, M. Bradke, *J. Power Sources* 63 (1996) 193.
- [25] M. Mathias, J. Roth, J. Fleming, W. Lehnert, in: W. Vielstich, A. Lamm, and H.A. Gasteiger (Eds.), *Handbook of Fuel Cells: Fundamentals, Technology, and Applications*, John Wiley & Sons, New York, 2003.
- [26] A.Z. Weber, J. Newman, *J. Electrochem. Soc.* 152 (2005) A644.

- [27] S. Park, J.-W. Lee, B.N. Popov, J. Power Sources 163 (2006) 357.
- [28] S. Park, J.-W. Lee, B.N. Popov, J. Power Sources, 177 (2008) 457.
- [29] S. Lister, G. Mclean, J. Power Sources 130 (2004) 61.